

The Design of a Control Architecture for a Heavy-Lift Precision Manipulator for Use  
in Contact with the Environment

by

William T. Becker III

Bachelor of Science, Magna cum Laude, Mechanical Engineering  
University of Maryland, College Park 2004

Submitted to the Department of Mechanical Engineering  
in Partial Fulfillment of the Requirements for the Degree of  
Master of Science

at the

Massachusetts Institute of Technology

June 2006

© Massachusetts Institute of Technology  
All Rights Reserved

Signature of Author . . . . .

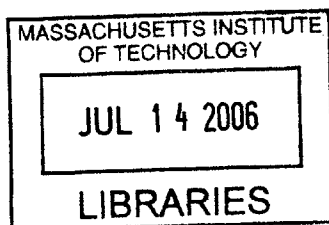
Department of Mechanical Engineering  
May 9th, 2006

Certified by . . . . .

Steven Dubowsky  
Professor of Mechanical Engineering  
Thesis Advisor

Accepted by . . . . .

Professor Lallit Anand  
Chairman, Committee on Graduate Studies



BARKER

The Design of a Control Architecture for a Heavy-Lift Precision Manipulator for Use in  
Contact with the Environment

William T. Becker

Submitted to the Department of Mechanical Engineering  
on May 9, 2006, in partial fulfillment of the  
requirements for the degree of  
Master of Science in Mechanical Engineering

**Abstract:**

Robotic manipulators can be used to enhance the strength and dexterity of a human user. This thesis considers the design of a controller for a heavy-lift manipulator for lifting and inserting payloads onto aircraft on the deck of a ship. The purpose of this robot is to reduce manpower requirements aboard the ship, and reduce the physical requirements for the individuals loading the payloads onto an aircraft. This particular application presents several control challenges, including structural resonances, complex interaction with the environment, high joint friction that varies over time, tight tolerances for the insertion tasks, and ship motions.

This thesis builds upon previous works by Garretson [17] and DiCicco [9] by further developing an insertion control mode for intuitive human interaction with the payload of the manipulator when in contact with the environment. These control algorithms, as well as those developed in the previous work, are also validated on a laboratory manipulator.

This thesis contains a detailed description of the control architecture for the heavy lift manipulator, including the insertion control mode and a position control mode for use when the manipulator is not in contact with the environment. Both architectures are validated with dynamic simulation models. The position control response of this manipulator is shown to be improved with the implementation of friction compensation. In some joints, outputs from an adaptive friction estimator are used to make feed-forward models of friction for use during environmental contact. The position and insertion controllers are then evaluated under open-loop and human control on a laboratory manipulator.

Thesis Supervisor: Steven Dubowsky, Professor of Mechanical Engineering

## **ACKNOWLEDGEMENTS**

I would like to thank Foster-Miller and the U.S. Navy for their support of this research. I would also like to thank the entire Field and Space Robotics Lab, who are an amazing group of people to work with. Special thanks go to those who worked with me on this project- Justin Garretson, Matt DiCicco, Matt Lichter, Jamie Nichol, and Takeshi Takuara. I would also like to thank Dr. Dubowsky for his guidance and giving me the opportunity to work on this research, as well as for giving me a kick in the right direction when I needed it.

I would not have made it this far without the help and support of a lot of people- far too many to thank individually. You all are a constant reminder of what is really important in life. Special thanks to Dalia, Steve, Grant, Amy, and Bill for your friendship, and for keeping me sane for these past two years. Thanks to Sheena for always being there (even though there was a long way away) for me, and for putting up with all of my flaws and indiscretions. Finally, thanks to Mom, Dad, Alex, and Andy. Without your support and encouragement throughout my life, I would never be in a situation where I had the opportunity to write these words. I hope I have made you proud. This thesis is dedicated to you.

# TABLE OF CONTENTS

---

Abstract .....	1
Acknowledgements .....	2
Table of Contents .....	3
Chapter 1: Introduction .....	6
1.1 Introduction .....	6
1.2 Challenges .....	7
1.2.1 Environmental Factors .....	7
1.2.2 Structural Resonances .....	8
1.2.3 Joint Friction .....	8
1.2.4 High Precision .....	8
1.2.5 Contact Forces .....	9
1.2.6 Intuitive Human Interaction .....	9
1.3 Background Literature .....	10
1.3.1 Control of Robotic Manipulators .....	10
1.3.2 Friction Compensation .....	11
1.3.3 Force Control Interaction .....	13
1.3.4 Force Interaction with a Human User without Bilateral Force Feedback .....	14
1.3.5 Prior Work on Similar Projects .....	15
1.4 Contributions of this Thesis .....	16
1.5 Thesis Outline .....	16
Chapter 2: Control Architecture .....	18
2.1 System Description .....	19
2.1.1 Joint Configuration and Coordinate Systems .....	19
2.1.2 Sensors and User Interface .....	21
2.1.3 Friction Models .....	22



2.1.4 Operation Assumptions.....	23
2.2 Position Control .....	25
2.2.1 PID Controllers .....	27
2.2.2 Gravity and Base Motion Compensation.....	28
2.2.3 Friction Compensation.....	29
2.3 Insertion Control .....	32
2.3.1 Admittance Control.....	35
2.3.2 Friction Compensation.....	38
2.4 Summary .....	39
Chapter 3: Simulation Tests and Results .....	40
3.1 Description of the Simulated System.....	41
3.2 Position Control Simulations .....	43
3.2.1: The Representative Task.....	43
3.2.2: Friction Model Extraction.....	48
3.3 Insertion Control Simulations .....	54
3.3.1 Force Impact Simulations .....	56
3.3.2 Endpoint Spirals.....	60
3.3.3: Aligned Insertion Simulation.....	64
3.3.4: Misaligned Insertion Simulation.....	70
3.4 Summary .....	74
Chapter 4: Laboratory Tests.....	75
4.1 Experimental Setup.....	76
4.2 Controller Details and Modifications.....	78
4.2.1 Endpoint Selection.....	78
4.2.2 Scaling and Joint Controller Modifications .....	78
4.2.3 Modifications to the Friedland-Park Algorithm .....	79
4.2.4 Payloads and Insertion Setup .....	81

## CHAPTER 1: INTRODUCTION

---

### 1.1 Introduction

This thesis presents the design of a control system for a shipboard heavy-lift serial manipulator being developed commercially for the United States Navy. The purpose of this manipulator, seen in Figure 1, is to allow a single user to load payloads onto an aircraft while onboard a ship. This task is currently performed by a team of three to seven personnel, and requires a high level of strength from those personnel. A stated goal of the Navy is to reduce greatly the number of personnel required onboard an aircraft carrier due to budgetary and safety concerns. A robot with the stated capabilities would serve to both reduce the number of personnel required onboard a ship as well as the physical demands on those personnel.

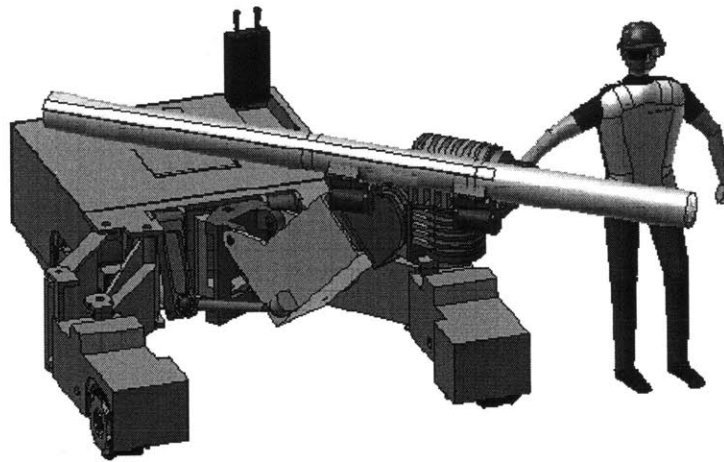


Figure 1: Artist's concept of the heavy-lift manipulator system (Courtesy Foster-Miller Inc.)

The goal of the controller is to enable the user of the robot to acquire, maneuver, insert, and remove the payload from an aircraft. The manipulator is mounted on an omni-directional vehicle (ODV) base which allows the payload to be transported from storage to an aircraft while in a "load carrying position". This ODV is operated independent

4.3 Position Control Tests.....	82
4.3.1 Joint-Level Tests.....	82
4.3.2 Cartesian Trajectories .....	88
4.4 Friction Model Extraction.....	90
4.4.1 Adaptive Law Tuning .....	90
4.4.2: Friction Model Identification.....	92
4.4 Insertion Control Tests.....	96
4.4.1 Control Notes .....	96
4.4.2. Horizontal Open Loop Force Impact Experiment .....	97
4.4.3. Vertical Open Loop Force Impact Experiment.....	100
4.4.5: Open Loop Compliance Experiments.....	102
4.4.5: Human in the Loop Tests.....	106
4.5 Summary.....	111
Chapter 5: Conclusions .....	113
5.1 Suggestions for Future Work on this Project.....	114
References.....	117
Appendix A: Joint and Admittance Tuning .....	122
Appendix B: Adept Parameter Identification .....	129
Appendix C: Adept Joint 1 Friction Modeling .....	135
Appendix D: Gravity Compensation Equations .....	138
Appendix E: Manipulator Parameters.....	143
Kinematic Parameters .....	143
Inertial Parameters .....	144
Friction Parameters .....	145
Appendix F: Payload Dimensions and Tolerances .....	146
Appendix G: Insertion Control User Survey .....	149

from the manipulator, and is held motionless any time the payload is being maneuvered by the manipulator. The control of this ODV is not discussed in this thesis.

This thesis builds upon the work of Garretson [17] and DiCicco [9], who developed the primary architecture of the control system. This control system consists of a position control system, and an insertion control system which enables a user to maneuver a payload in contact with the environment without the benefit of bilateral force feedback. This thesis further develops these control systems and applies them to test dynamic simulation models of the heavy lift manipulator, and a laboratory hardware system.

Beyond this specific application, the research in this thesis can be extended towards many applications for heavy lift manipulators, particularly where a large payload must be maneuvered in contact with the environment. In addition, the capabilities of the control system may be extended to force-amplification, force-reduction, or teleoperated systems in which bilateral force feedback is not available.

## **1.2 Challenges**

A number of unique challenges arise in the development of the control system for the shipboard heavy-lift manipulator. This section gives a brief description of these challenges, and outlines the requirements for the implementation of a control system that can successfully overcome them.

### **1.2.1 Environmental Factors**

The deck of a ship is a challenging environment for control system design. An environment with variable disturbances such as wind and ship motion creates a difficult situation for a precision manipulator. Major external environmental disturbances must be adequately compensated or rejected by the control system to allow a user to successfully operate the manipulator.

In addition to dynamic disturbances, the harsh environment of the deck of a ship will cause changes and deterioration of the physical manipulator. Temperature variations, lubrication breakdown, as well as salt, water, and corrosion can cause changes in the friction in the manipulator or degradation of sensor signals. The control system must be

able to compensate for the time-varying effects of the environment, and be minimally sensitive to errors which could develop over time.

### **1.2.2 Structural Resonances**

The large, heavy payloads and heavy construction of the manipulator result in low structural resonant frequencies of the system. Raising control system gains allows superior precision and response of the manipulator, as well as superior rejection of disturbance forces. However, the bandwidth of the control system gains must be limited to avoid exciting the structural resonant frequencies of the physical system. The limited control system gains reduce the ability of the control system to compensate for disturbances such as friction and gravitational modeling errors. Therefore, dedicated compensation architecture must be implemented to reject significant sources of disturbance to the system.

### **1.2.3 Joint Friction**

This manipulator has been designed to lift payloads of up to 3000 lbs (1360 kg). This capacity requires powerful motors and high gear-ratio transmissions to actuate the joints of these manipulators. These motors and transmissions typically have high friction, which results in tracking errors, stick-slip, and other undesired behaviors. In some cases, these problems may be overcome by raising system control gains. However, in this manipulator, low structural natural frequencies introduce stability concerns that limit the control gains that may be used. In order to account for these problems, a method to explicitly compensate for the effects of friction is necessary. As mentioned in the previous section, environmental factors will cause the joint friction to change over time. As a result, the friction compensation method must be robust to these time-varying changes, and compensate for the effects of friction so that the manipulator is capable of tracking its desired trajectory and successfully inserting the payload.

### **1.2.4 High Precision**

Depending on the payload, the manipulator must execute insertion tasks with accuracies on the order of millimeters. Precisions of that scale are common in smaller manipulators, but are seldom found in manipulators with the load capacity of this

manipulator. In addition, the added challenges of high joint friction and slow controller bandwidth make precise position control difficult. In addition to a well-tuned position control system for maneuvering in free space, it is necessary to design a system that can use the effects of the environment to aid the user in performing the insertion task, as discussed next.

### **1.2.5 Contact Forces**

The nature of an insertion task requires the manipulator or the payload to come into contact with the environment. The features of the contact surface and the payload are well known to the user, allowing him or her to formulate a mental model of the payload-environment interaction. The contact forces which arise from this interaction act as a disturbance that can affect the tracking of the manipulator. However, these contact forces can also be used to provide clues that allow a user to recognize the surface features of the contact surface. These clues are similar to those tactile clues a human uses when interacting with the environment through a tool. If properly utilized, the clues can greatly improve the ability of a user to move the payload along a surface and insert the payload.

### **1.2.6 Intuitive Human Interaction**

The heavy manipulator system in this thesis is controlled by a human user. Even if the control system allows the manipulator to position the payload with zero tracking error to its desired position, it is unlikely that the insertion task would be successful if the user's wishes are not properly translated into movement of the manipulator. Both the method of translating a user's force or position inputs and the coordinate frame of those inputs have a profound effect on the behavior and usability of the manipulator.

The manipulator interface is designed so that a user will either use a joystick at the base of the manipulator or a force handle mounted on the manipulator near the payload. The physical system design prevents true bilateral force feedback of the environmental contact forces to the user. Instead, the control system must be designed to combine the inputs of the user and any available information about the environment in order to give the user some interface that will allow successful insertion of the payload.

Successful insertion of the payload is facilitated by a user interface that behaves in an intuitive manner. For example, if the user is operating a force handle, the manipulator must 'push' and 'twist' the payload in the direction the user is pushing or twisting, allowing the user to feel like he or she has complete control of the manipulator and its payload. The manipulator should also react naturally to contact with the environment. A slight contact should not result in the manipulator moving sharply out of the way, or pushing into the contact with more force.

Because user interfaces are difficult to evaluate in simulation, it is necessary to test the functionality of any control law with hardware.

## ***1.3 Background Literature***

### **1.3.1 Control of Robotic Manipulators**

The trajectory and position control of serial manipulators is a well-studied problem [4,53,58]. The most common forms of endpoint position control in industrial applications are Jacobian inverse and Jacobian transpose control using decentralized PID joint controllers about either position or velocity. Numerous performance enhancements to these simple control algorithms have been implemented, including integral saturation, filters, and partial feed-forward terms [54]. The reason for the widespread use of these control algorithms is that the linear control required for the individual joints is well understood, and simple to implement [27].

Many forms of manipulator control offer superior trajectory following performance if properly implemented, including the computed torque method, sliding mode control, and adaptive control. The computed torque method requires an accurate model of the plant, and consists of solving the equations of motion for time-varying joint torques to move the manipulator along the desired path. This form of control is useful if a highly accurate model exists and there are few disturbances [4]. Sliding mode control describes the desired trajectory as a reduced-order "sliding surface", with a stable first-order control law to pull the manipulator to this desired trajectory. Sliding control can be made very robust to disturbances, and it generally requires a less accurate model of the system than computed-torque control [4,50]. Many forms of adaptive control have been

proposed to identify parameters of the manipulator in computed-torque and sliding-mode control [7,51], including some which use fuzzy logic [59] and neural networks [33] to identify these parameters.

There is a tradeoff between control simplicity, robustness to disturbances, and trajectory following ability. Complex trajectory control algorithms require much more complexity in models and control laws than decentralized linear control. This is particularly true of high degree-of-freedom systems, in which model complexity scales exponentially. Because of the modeling simplicity, well understood behavior, and robustness to disturbances, Jacobian inverse control has been selected as the control method for the manipulator in this thesis. The simpler architecture and robustness to disturbances also suit it well to working with force control algorithms, which are necessary when the manipulator comes into contact with the environment.

### **1.3.2 Friction Compensation**

Many control methods have been suggested to help systems estimate and compensate for the effects of joint friction [3]. These methods generally fall into three categories: model-based compensation, adaptive compensation, and sensor-based compensation.

Model-based friction compensation uses mathematical models to predict joint friction, which is then compensated with motor torque [19,42]. The effectiveness of this type of compensation depends on the accuracy of the models. Accurate characterization of joint friction is difficult in harsh environments such as this one, as friction will change over time with variations in temperature or wear [44].

To compensate for friction variations, methods have been proposed for online estimation of friction parameters using adaptive and observer-based approaches [3,5,15, 20]. These methods take advantage of known or measured information about the system dynamics to identify friction parameters online. Online friction identification and compensation using these single-joint observer methods has resulted in good position control performance in systems with high joint friction [32,34]. Single-joint adaptive identification is not practical for some systems, however, because adaptive identification may view contact forces as frictional disturbances and may become unusable when the



manipulator is in contact with the environment. The use of adaptive methods of friction compensation for systems in contact with the environment requires an adaptive model-based feed-forward structure, as well as a contact force sensor in order for the controller to differentiate between joint friction and contact forces [57]. The formulation of these adaptive methods is very complex, especially for high-degree-of-freedom systems [43].

Sensor-based compensation overcomes many of the problems of model-based and adaptive methods, but can only be used when the design of the robot allows the placement of sensors to provide direct feedback of the system friction. Torque control loops can then be used to reduce the effects of friction [37,45]. No model of the friction is required and the compensation is robust to friction changes with wear or temperature. This method has been shown to provide accurate compensation for joint friction; however, providing sensors at each joint can be costly and add to system complexity. More recently, an alternative sensor-based method has been proposed that allows the friction in all joints to be identified using a single six-degree-of-freedom force/torque sensor in the manipulator's base, greatly simplifying the hardware implementation of sensor-based approaches [23,41].

In summary, sensor-based methods of friction compensation are preferred when the sensor hardware is available. Adaptive methods can perform very well, but cannot handle contact forces without complex formulation. Model-based methods are more stable, but are not robust to unmodeled or time-varying effects. Because the system in this thesis has low structural natural frequencies, a high-gain linear controller is not feasible to implement. Force sensors are not present at some joints, and the manipulator is required to come in contact with the environment. However, a simple model-based compensator is insufficient for the friction variations caused by the harsh environment of the deck of a ship. For these reasons, an adaptive algorithm is used when the manipulator is moving in free space, and data from this algorithm is used update the parameters in a model-based feed-forward compensation algorithm to be used when the manipulator is in contact with the environment in the joints which do not have force sensor hardware available. To the author's knowledge, this is a novel approach to compensating for time-varying friction that remains stable in the presence of contact forces.

### 1.3.3 Force Control Interaction

Force control of manipulators is a much more difficult problem than position control, and has been a major area of research for over twenty years. A number of approaches to this problem have been investigated, including explicit force control, hybrid control, and stiffness/impedance control [6,56]. The major obstacle in all of these approaches is assuring stability of the controller when in contact with the environment.

Explicit force control is a general term for a controller that uses a measured contact force signal directly as an input signal to the plant. Explicit force controllers can be either force-based or position-based [55]. Modeling the interaction between the robot and environment is necessary in order to ensure stability of both forms of explicit force controllers [12,13,14,56]. In a force-based explicit force controller, a force sensor measures a contact force, compares it to a reference desired endpoint force, and formulates desired joint torques using PD, PID, or similar control laws. Examples of force-based explicit force controllers can be found in [1,31,60]. In a position-based force controller, also known as an admittance controller, the force from the contact force sensor is transformed into a desired position response through the use of an admittance law. This desired position is then input to an inner-loop position controller, which formulates a command based on the error between the desired and actual joint positions. Examples of admittance control can be found in [24,25,28]. Hybrid control is a term for a controller that utilizes position control in some directions, and explicit force control in other directions [38].

The admittance control concept has been extended in several directions in recent years, including natural admittance control and adaptive admittance control. Natural admittance control requires a precise model of the robot, and the force inputs to the contact sensor are transformed into admittances so that the robot modifies its endpoint trajectory as if a the contact force had acted upon the robot under no control, and is therefore passive to all contact forces [10,18]. Adaptive admittance control ensures stability by adapting an admittance law to the stiffness of the environment [48,49].

An alternative approach to explicit force control is impedance control. Impedance is the dynamic generalization of stiffness, and impedance control allows the modification

of the apparent inertia of a robot to disturbances. Impedance control achieves stability with the environment by reacting passively to all contact forces. It has the advantage that it does not require an extensive model of the interaction between the robot and the environment to maintain this stability [21,22].

The robot that is the subject of this thesis operates under position control for most of its motion, using decentralized PID position controllers tuned for good transient behavior and no structural resonance excitation. This well-tuned position controller can function as an inner loop to use with endpoint and user force inputs to an admittance controller. For this reason, admittance control has been selected as the control method of the manipulator when interacting with the environment.

#### **1.3.4 Force Interaction with a Human User without Bilateral Force Feedback**

Bilateral force-feedback is a term which describes a system that allows the user to feel the forces measured by a sensor at the end-effector of the robot, and to control the robot by applying forces to a controller. Such a system requires that the controller and the actual robot be decoupled from each other in a master-slave configuration, and requires that both the master user interface system be actively powered. Bilateral force feedback has been shown to provide an intuitive user interface in both virtual and teleoperated systems [2,39]. However, an actively powered master user interface adds additional complexity to both the physical and control system, as well as additional cost.

In the system described in this thesis, the human moves with the machine in the system, and it is therefore impossible to independently feed back the tactile forces the machine encounters in the environment to the user. This creates a challenge in designing a user interface for the robot that gives the user an intuitive "feel" for the manipulator. This type of robot is referred to as an "extender" or "exoskeleton": a robot which interacts with a user in such a way that power and information flow back and forth between the human and the machine [28]. These robots interact with the environment under force control from the user and share the same stability concerns as force controllers. Descriptions of the man-machine interaction and control strategies for this form of manipulator can be found in [26,29,30].

### 1.3.5 Prior Work on Similar Projects

As mentioned in Section 1.1, prior work on the development of the control system for this manipulator was performed by Garretson [17] and DiCicco [9]. A summary of the algorithms developed in these previous works are described in some detail in Section 2 of this thesis, and their contents are only briefly described here. In [17], the position control algorithm for the manipulator was developed. This included a description of the resolved-rate controller with decentralized joint PID controllers, and development of the friction compensation and base motion compensation algorithms. This work also developed separate friction control algorithms for when the manipulator is in free space, and when it is in contact with the environment. This work developed several tasks representative of actual payload acquisition, maneuvering, and insertion. Finally, the position control system was validated in dynamic simulation. These simulations demonstrated the capability of the position control system to follow desired trajectories for simple motions and representative tasks when maneuvering several payloads. The tests compared the ability of the manipulator to follow the trajectories in the presence of disturbances such as friction and ship motion, and demonstrated successful implementation of the friction and base motion compensation algorithms.

In [17], the necessity of a second form of control for the insertion phase of the task became clear, as the tracking errors which occurred using the position controller were on the same order of magnitude as the insertion geometry tolerances. This second form of control, called Insertion Control, was developed in [9], and includes the effects of contact force in an admittance control law to aid the user in the insertion task. An in-depth comparison of admittance control against impedance control and other forms of force control was included in this work. Simulations of the behavior of the insertion controller while moving the payload along a fixed surface were performed, as well as simulation studies of an insertion task while modeling visual feedback of a user as an outer PD loop. An external jam-prevention watchdog algorithm was also developed, which could be useful during insertion.

A system similar to the one presented in this thesis has been developed by Oak Ridge National Laboratories [8]. It has 8 or 9 degrees of freedom, and utilizes hydraulic actuators instead of electric motors. A test prototype of this system received favorable

reviews by expert munitions handlers in the U.S. Air Force using both velocity and acceleration-based control laws, though the opinions varied strongly with gains on the control laws [11]. A promising control algorithm for this system is a form of admittance control they refer to as 'accommodation control'. This system is similar to the insertion controller found in [9], but uses a velocity controller, and treats human input as a 100 to 1 force amplifier against contact forces [36]. This group has also considered naval applications for manipulators, particularly examining the effect of ship motions and methods to compensate for these effects [35].

## ***1.4 Contributions of this Thesis***

This thesis furthers the prior work of Garretson [17] and DiCicco [9], and details the control architecture and algorithms to be used on a heavy lift precision manipulator that must be able to interact with the environment under hostile conditions. Implementation issues of the insertion controller, particularly the kinematic and velocity transforms necessary to provide stable and intuitive control, are examined in greater depth than the previous work. The fundamental behavior of the insertion controller is examined in simulation, and the ability of the controller to exploit compliance with the environment to achieve an insertion task is demonstrated. Finally, this thesis reports on the successful implementation of the control algorithms on a laboratory robot.

## ***1.5 Thesis Outline***

The architecture of the control system for the manipulator is detailed in Chapter 2. This chapter includes a description of the physical system, followed by a description of the position control architecture and insertion control architecture, including all disturbance compensation algorithms.

Chapter 3 contains the results of simulation studies evaluating the performance of both control modes of the manipulator. These tests include a study of the sensitivity of the position control algorithm to sensor and modeling errors, with an emphasis on the ability of the algorithm to accurately extract friction parameters, as well as open loop evaluations of the insertion control algorithm beyond those described in [9].

Chapter 4 describes the implementation and performance of the control architecture on a four degree of freedom laboratory manipulator. The manipulator is tuned for dynamic similarity with the full scale manipulator. Both the position and control modes are evaluated, including the friction compensation and extraction algorithm. Tests with a human in the loop demonstrate that the insertion control algorithm enables a user to successfully insert payloads with geometric similarity to the full-scale payloads.

Chapter 5 concludes this thesis with a summary of the results from chapters 3 and 4, and suggests further areas of exploration which expand upon the task of environmental interaction without bilateral force feedback.

## **CHAPTER 2: CONTROL ARCHITECTURE**

---

The purpose of the control architecture for the heavy-lift manipulator described in this thesis is to give the user of the manipulator a control tool that will allow him to single handedly load and unload payloads to an aircraft with ease. The control system must give the user an intuitive interface for moving the payload and manipulator with a desired velocity. To improve the usability of the manipulator, the control architecture must compensate for all major disturbances, including joint friction, base motion, and gravity.

As discussed in Section 1.3.1, the controller has two distinct modes: a position control mode, and an insertion control mode. Position control mode, as its name suggests, attempts to achieve a desired position input by the user. This mode is used any time when the manipulator is not in contact with the environment, and allows the user to input desired a payload motion in Cartesian space, or to input a desired movement of manipulator joints.

Insertion Control Mode is used when the manipulator or its payload is in contact with the environment, either when the manipulator is acquiring the payload, or when it is attaching the payload to the aircraft. The insertion control mode is fundamentally different from the position control mode in two different ways. First, in the insertion control mode, the desired position of the manipulator comes from a combination of the user input and the contact force on the manipulator instead of purely from the user input. Second, in the insertion control mode, the contact of the manipulator with the environment requires a different form of friction compensation from the position control mode in certain joints. This chapter includes a description of the physical heavy-lift manipulator system, and then a detailed description of the control architecture implemented on this system for both position control mode and insertion control mode, including details on all disturbance compensation algorithms.

## 2.1 System Description

The robot is a six degree-of-freedom robotic manipulator carried by an omni-directional vehicle that allows the robot to move from point to point while carrying the payload, as seen in Figure 2. This vehicle is controlled entirely separately from the manipulator. When the manipulator is being controlled by the user, stab jacks lift the omni-directional wheels off of the ground, effectively providing a fixed base for the manipulator. The control system described in this section is designed to control only the manipulator, not the omni-directional vehicle. The user interfaces are a joystick on the omni-directional base, and a force-sensing handle located at the end of the manipulator, near the payload.

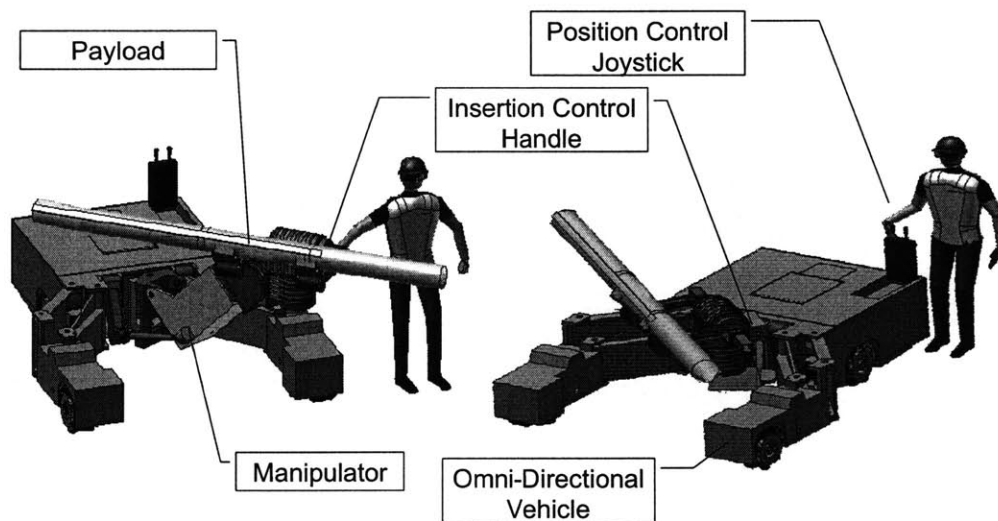


Figure 2: System overview and user interface locations (courtesy Foster-Miller Inc.)

### 2.1.1 Joint Configuration and Coordinate Systems

Figure 3 is a diagram of the joint configuration and coordinate systems of the manipulator. Joints one and two of the manipulator are base yaw and pitch joints, respectively. The two joints are dependently linked to each other, and actuated by parallel linear actuators mounted on the base of the robot, as seen in Figure 4. Joint three is a prismatic joint also powered by a linear actuator that extends the end three joints from the base. Joint four is an end pitch joint and joint five is an end yaw joint. Joint six pitches or rolls the payload, depending on joint configuration. The end-effector is a pair



of fork tines that can either be inserted into a pallet (like a fork-lift) for larger payloads, or fitted with grippers to grasp smaller payloads. The actuators for the first three joints are linear actuators powered by gear-motors with roller-screw transmissions. The actuators on the end three joints are proprietary high-torque direct-drive motors.

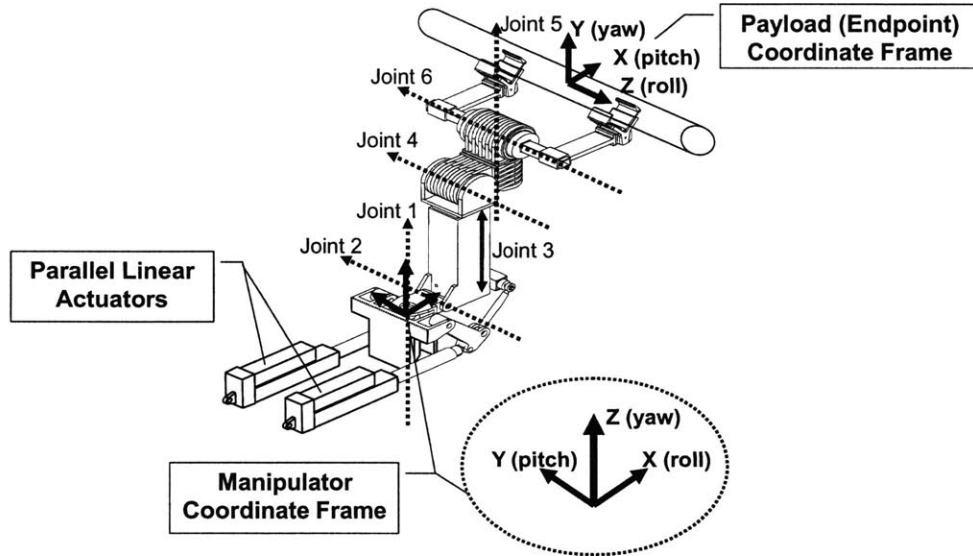


**Figure 3: Manipulator joint configuration and coordinate frames (Courtesy Foster-Miller Inc.)**

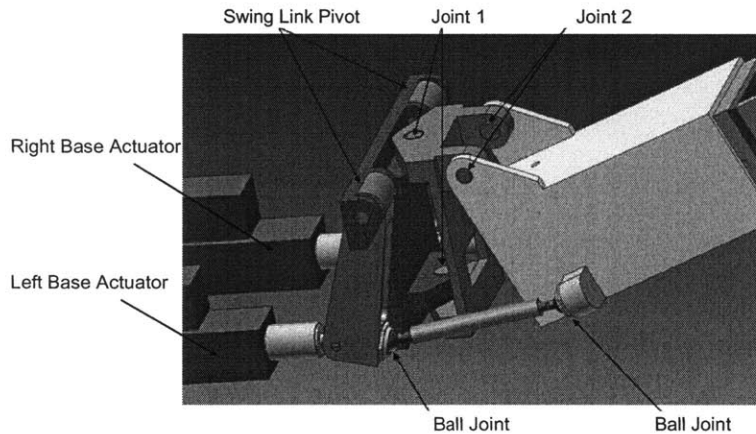


**Figure 4: Base actuator configuration for joints 1 and 2 (Courtesy Foster-Miller Inc.)**

This configuration of joints results in a kinematic singularity when joint 5 (end yaw joint) is at either  $0$  or  $180^\circ$ . When the manipulator is near this singular configuration, the Jacobian inverse controller is ill-behaved. For this reason, when the manipulator is near the singularity, the control system should allow only direct joint commands. For a more complete description of kinematic singularities of this robot, see [17].

The manipulator coordinate system origin is located at the base of the manipulator along the axis of joint 1. The Z axis corresponds to the vertical direction, X is the forward direction, and Y is the sideways direction. Rotations about the X, Y, and Z axes are referred to as roll, pitch, and yaw, respectively. The origin of the payload coordinate frame is at the height of the center of mass of the payload above the endpoint of link six, midway between the grippers or fork tines. In this coordinate frame, Z is along the long axis of the payload, Y is vertical when joint 6 is level to the ground, and X is horizontal and perpendicular to the long axis of the payload. Payload rotations about the X, Y, and Z axes are referred to as pitch, yaw, and roll motions, respectively.

### **2.1.2 Sensors and User Interface**

The robot is equipped with high-accuracy encoders on all joints to measure joint position. As seen in Figure 5, load cells are located after the transmission on the motors for joints 1-3, enabling measurement of the force applied by each linear actuator. Force sensors are not present in the other three joints due to mechanical design constraints. A six-axis force-torque sensor is in place in link 6 to measure forces on the payload. The force measurement from this sensor is a combination of contact forces of the payload, the weight of the payload, and inertial effects from acceleration of the payload. If the weight of the payload is subtracted from this measurement, and the manipulator is moving slowly so inertial effects are minimal, this sensor can be used to measure the contact forces and torques on the payload. A three-axis accelerometer is located in the base of the manipulator and used in control loops that compensate for ship motions and inclined floor surfaces. The user interfaces are a joystick on the omni-directional base, and a force-sensing handle located near the payload, as previously shown in Figure 2.

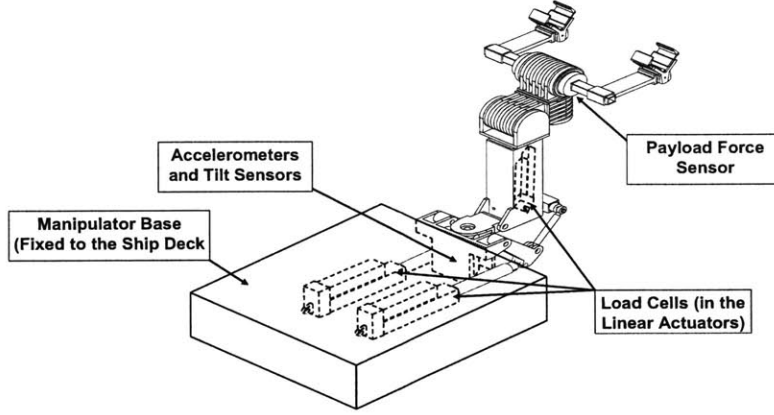


Figure 5: Sensor locations on the manipulator

### 2.1.3 Friction Models

Laboratory tests of the motors used in the base joints and the end joints reveal that very different friction profiles exist in each group of joints.

The friction behavior in the base joints has coulomb and viscous components and some stick-slip behavior, as well as a linear dependence on the static load on the motor. The friction model given in equation (2.1) was extracted from the experimental data, and the model is shown in Figure 6 for constant static load.  $\alpha_1$  and  $\alpha_2$  define coulomb friction and the effect of static load.  $\alpha_3$  defines the contribution of viscous friction. The  $\beta$  terms define a nonlinear velocity-dependent shaping function to approximate the stick-slip model. Further information on this approximation can be found in [1,4]. The parameters defining these friction profiles are given in Appendix E.

$$\tau_{friction} = -[(\alpha_2 + \alpha_1 F_{load})(\beta_1 + \beta_1(1 - e^{-\beta_1|\dot{q}|}) + \alpha_3|\dot{q}|)\text{sgn}(\dot{q})] \quad (2.1)$$

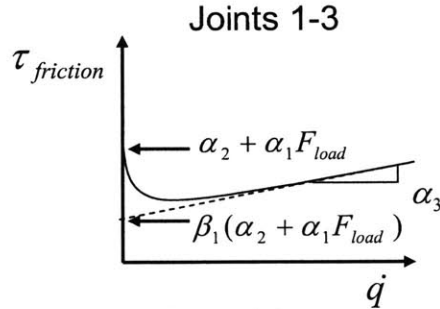


Figure 6: Friction model as a function of velocity for joints 1-3

Because joints 4-6 use direct-drive motors, the only significant source of friction in those joints is from the motors themselves. Their friction profile, given by equation (2.2), is a function of joint velocity and motor load. Stick-slip effects were not significant.  $\alpha_1$  defines the velocity-dependent term,  $\alpha_2$  defines the zero-velocity, zero-load level of friction, and  $\alpha_3$  and  $\alpha_4$  define the contribution of motor load to the friction.  $C$  is a constant 8.8504. The friction model with respect to motor load is shown for a constant velocity in Figure 7.

$$\tau_{friction} = -\frac{(1 + \alpha_1|\dot{q}|)(\alpha_2 + \alpha_3|C\tau_{motor}| + \alpha_4(C\tau_{motor})^2)}{C} \text{sgn}(\dot{q}) \quad (2.2)$$

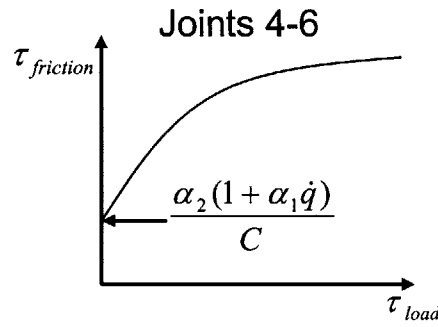


Figure 7: Friction as a function of load on the motor for joints 4-6

#### 2.1.4 Operation Assumptions

The design of this control architecture assumes several things about the operation of the manipulator.

1. When in position control mode, the user controls the manipulator through the joystick at the base of the manipulator
2. At any point when the manipulator is near a singularity, the manipulator will be under joint control in position control mode. This is a safety feature that must be written into the controller code.
3. When in position control mode, neither the manipulator nor the payload comes into contact with the environment. Also, the user does not push on the manipulator or payload during position control mode.

4. When in insertion control mode, the user controls the manipulator through the force handle near the end effector
5. When in insertion control mode, the manipulator is well away from any singularities. This is a safety and controllability feature that must be written into the controller code.
6. The base of the robot is motionless with respect to the ground during all manipulator motions (i.e. the omni-directional base is not moving and is raised on its stab jacks)
7. The manipulator is designed to be used for payloads from under 100 kg to 1350 kg. In this work, only two payloads are considered:
  - a. The heavy payload has a mass of 1350 kg. The insertion geometry is representative of payloads above 200 kg, and has large insertion tolerances on the order of 1 cm.
  - b. The light payload has a mass of 165 kg. The insertion geometry is representative of payloads under 200 kg, and has much tighter insertion tolerances (on the order of 2 mm). In addition, after insertion, the payload must be slid along a slot until it engages with a latching mechanism. This payload, its insertion geometry, and the insertion tolerances are shown in Figure 8. A simplified form of this payload is used in all simulations in Chapter 3, and the two-lug experimental payload constructed in Chapter 4 is scaled to this payload. For more detailed drawings of this payload, see Appendix F.

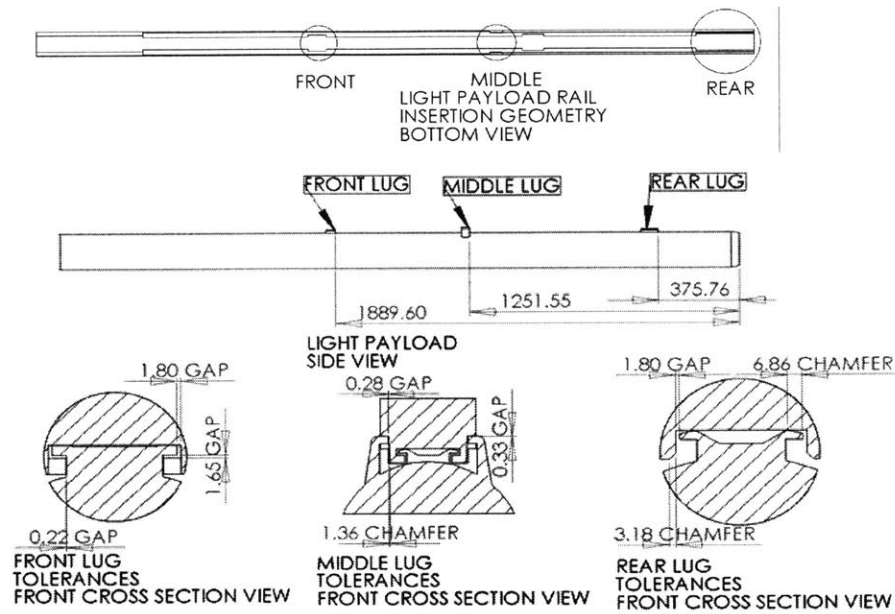


Figure 8: Dimensions of the light payload insertion geometry

## 2.2 Position Control

The presence of the load cells in joints 1-3 allows the use of torque control loops to compensate for the majority of friction in those joints. The absence of load cells in joints 4-6 means that a different form of friction compensation must be used. During position control mode, an adaptive friction compensation algorithm will be used in these joints. These different forms of friction compensation require fundamentally different joint-level controllers.

The control architecture for the first three joints is shown in Figure 9, and the control architecture for the end three joints is shown in Figure 10.

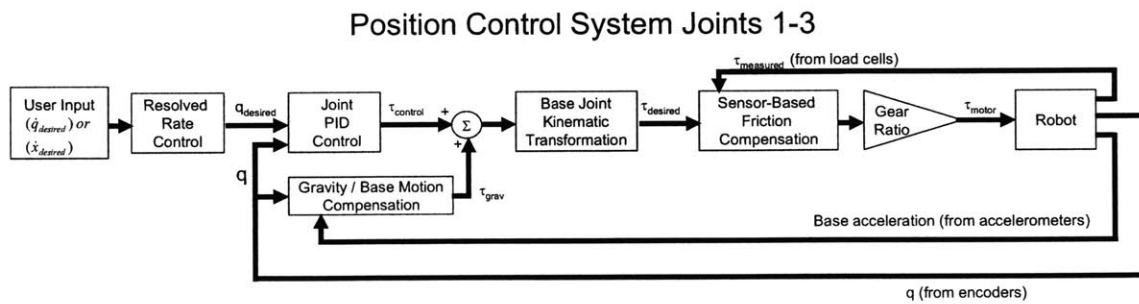


Figure 9: Position Control System block diagram for joints 1-3

The user inputs a desired Cartesian velocity for the payload or joint velocity from a joystick. If a desired Cartesian velocity is input, it is transformed into desired joint velocities through the use of the manipulator Jacobian transform (2.3).

$$\dot{\underline{q}}_{des} = J_{man}^{-1} \dot{\underline{x}}_{des} \quad (2.3)$$

where  $\dot{\underline{q}}_{des}$  is the vector of desired joint velocities,  $\dot{\underline{x}}_{des}$  is the vector of desired Cartesian velocities, and  $J_{man}$  is the manipulator Jacobian transform of joint velocities to end effector velocities. The desired joint velocity is then integrated into a desired position by the resolved rate controller (2.4) and then input to joint level PID controllers.

$$\underline{q}_{des} = \int \dot{\underline{q}}_{des} \quad (2.4)$$

where  $\underline{q}_{des}$  is the vector of desired joint positions. At this point, the control architecture fundamentally changes between the joints using sensor-based friction compensation, and those using adaptive friction compensation. Details about the PID controllers are further discussed in Section 2.2.1 and Appendix A.

In the base three joints, the PID controllers act upon the error between the actual and the desired joint positions to output a control torque. This torque is then added to a pose and base-dependent gravity and base motion compensating torque, which is also calculated at a joint level, and further discussed in Section 2.2.2. In the coupled yaw and pitch joints (joints 1 and 2), this desired joint torque is then kinematically transformed into desired linear actuator forces. This is accomplished through the use of equation (2.5).

$$\begin{bmatrix} F_{desR} \\ F_{desL} \end{bmatrix} = J_{base}^T \begin{bmatrix} \tau_{des1} \\ \tau_{des2} \end{bmatrix} \quad (2.5)$$

where  $F_{desR}$  and  $F_{desL}$  are the desired forces from the right and left base linear actuators,  $\tau_{des1}$  and  $\tau_{des2}$  are the desired torques on joint 1 and 2 from the PID controllers and gravity compensation algorithm, and  $J_{base}$  is the Jacobian transform of linear actuator velocities to joint 1 and 2 velocities. Because joint 3 is prismatic, the force desired in joint space from joint 3 is equal to the force from the linear actuator. The desired linear actuator forces are then input to the sensor-based friction compensation algorithm, which will be described in Section 2.2.3.1. This algorithm uses a feedback signal from the load cells to

compensate for friction by driving the error between the desired force and the measured torque to zero. Finally, the actuator torque is converted to a motor torque by multiplying by the gear ratio of the linear actuator, and this torque is sent to the robot.

The end three joints, as seen in Figure 10, also use joint level PID controllers to calculate a control torque for each joint. This torque is then added to a friction compensation torque from an adaptive algorithm. This friction compensation algorithm uses an observer to compensate for all uncompensated disturbances to the joint, and will be further discussed in section 2.2.3.2. It requires the joint velocity, joint inertia, and the sum of all non-disturbance torques applied to the joint as inputs. Gravity and gravity compensation are assumed to offset, and any difference in the two is considered a disturbance. The combined command and friction compensation torque is then added to a gravity and base motion torque, which is calculated the same way as for the first three joints. The total torque is then sent to the robot.

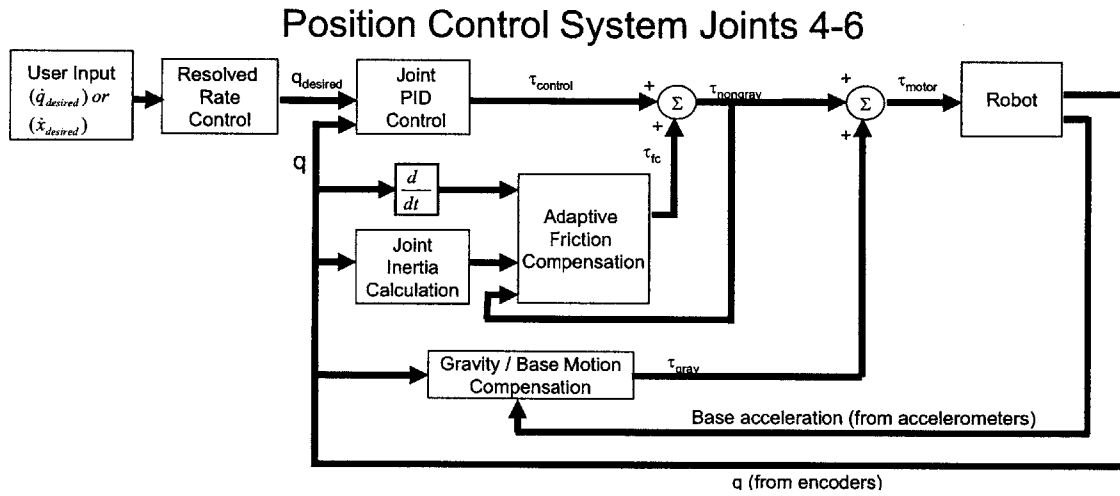


Figure 10: Position Control System block diagram for joints 4-6

### 2.2.1 PID Controllers

Two forms of joint-level controller were considered for this robot: PI controllers that close the loop about joint velocity, and PID controllers that close the loop about joint position. For practical reasons, the form of joint controller should remain as unchanged as possible between the two modes. In [9], DiCicco noted that velocity controllers provide a more intuitive "feel" when used with direct human interaction, due to possible



undesired movement at the end of a trajectory when a position-loop joint controller attempts to settle at a reference position. However, in a well-tuned position controller, this undesired movement is minimal. Also, controllers which close the loop about joint position are more resistant to disturbances to the manipulator. Therefore, joint position PID controllers have been selected for use in this manipulator, with an additional natural damping term acting upon the negative joint velocity for stability. Results from tests with the insertion controller indicate that integral joint control cause limit cycling behavior of manipulator contact forces when in contact with the environment, so the integral gain of the controllers is set to zero during insertion control mode. Details on the tuning of the joint controllers can be found in Appendix A.

One of the challenges in designing a control system for this robot is ensuring that the controller does not excite structural resonances in the manipulator. The lowest resonant frequency of the manipulator structure is anywhere from 5 Hz to 9 Hz, depending on the payload. To ensure these resonances are not excited, the individual joint controllers are tuned to a bandwidth one decade below the structural resonant frequency. The joint controllers are tuned to a damping ratio of 0.707, which allows for a fast, controlled response. Tuned joint gains for the two payloads discussed in this thesis have been calculated (see Appendix A).

### **2.2.2 Gravity and Base Motion Compensation**

The gravity and base-motion compensation algorithm used in this controller uses accelerometers and tilt sensors in the base of the manipulator to find the direction and magnitude of an "apparent gravity vector". In [17], an analytic model of the heavy lift manipulator on a simulated ship deck demonstrated that this algorithm would compensate for over 90% of the disturbance from the ship moving under the maximum sea state and that the uncompensated rotational effects were relatively small.

The apparent gravity vector is the sum of the gravitational and translational acceleration vector at the base of the manipulator. Based upon the apparent gravity vector and the joint angles of the robot, a closed form solution can be found to solve for the joint torques that will counteract the gravitational and translational acceleration

effects on the links of the robot and its payload in each direction in manipulator space (see Appendix D). These torques are then added (2.6).

$$\underline{\tau}_{gc} = \underline{\tau}_{gcX}(\underline{q}, g_x) + \underline{\tau}_{gcY}(\underline{q}, g_y) + \underline{\tau}_{gcZ}(\underline{q}, g_z) \quad (2.6)$$

where  $\underline{q}$  is the vector of joint angles of the robot, and  $g_x$ ,  $g_y$ , and  $g_z$  are the components of the apparent gravity vector in manipulator space. This compensation algorithm has the effect of compensating for the combined effects of gravity and acceleration of the base of the robot. If the kinematic model of the robot is perfect, and sensor readings are accurate, the only uncompensated effects from ship motion will come from the higher order rotational terms. Simulation studies in [17] showed that the effects of compensated ship motions during the position control task did not greatly diminish the tracking ability of the manipulator.

### 2.2.3 Friction Compensation

As discussed in section 1.3.3, sensor-based methods of friction compensation are preferred when the sensor hardware is available for all joints. Adaptive methods can perform very well, but cannot handle contact forces. Model-based methods are more stable, but are not robust to unmodeled or time-varying effects. The system in this paper has low structural natural frequencies, so gains cannot be raised to overcome friction. Force sensors are not present at some joints, and the manipulator is required to come in contact with the environment. However, a simple model-based compensator is insufficient for the friction variations caused by the harsh environment of the deck of a ship. This section describes a practical friction compensation architecture that uses a combination of sensor-based, model-based, and adaptive approaches for this system.

#### 2.2.3.1 Joints 1-3: Torque Control Loops

The force sensors in the first three joints of the manipulator are located between the end of the roller screw of the linear actuators that power the joints, and the linkage of the joint itself, as seen in Figure 11. This allows a reliable measurement of the force transmitted through this point in the manipulator. The force at the end of the linear actuator is related to the motor torque by equation (2.7):

$$F_{Loadcell} = \tau_{measure} \frac{2\pi R_g}{L} \quad (2.7)$$

where  $L$  is the lead of the roller screw, and  $R_g$  is the transmission gear ratio. This measured torque is fed back into a torque control loop. The error between this measured torque and the desired torque is input into a PI controller, so that actual torque applied to the joint tracks that desired by the PID position controller and gravity compensation [11]. The gains (see Appendix A) in the torque control loops have been selected so that their bandwidth is approximately ten times the bandwidth of the PID controllers, which makes the dynamics of the torque loops effectively invisible to the overall system.

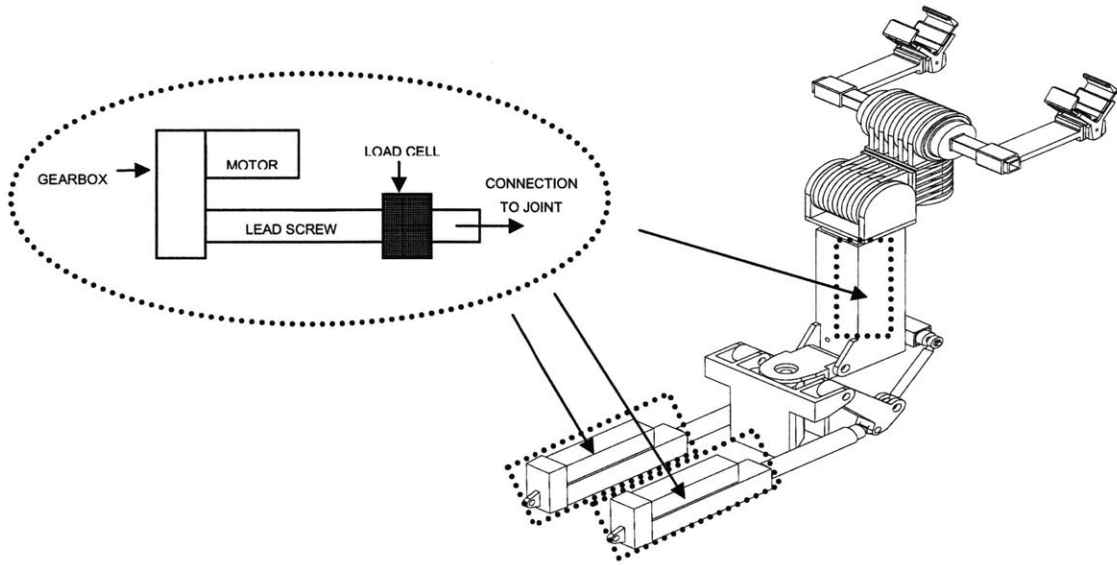


**Figure 11: Configuration of the load cells in series with the motors in joints 1-3 (from[17], courtesy Foster-Miller Inc.)**

#### **2.2.3.2 Joints 4-6: Adaptive Friction Compensation**

The adaptive estimator used in this manipulator was originally proposed by Friedland and Park [16]. This method has been shown to provide accurate online estimates of friction in position control systems, without regard to the model of the friction [9, 15, 17]. Like most adaptive algorithms, the Friedland-Park algorithm is based on a dynamic model of the joint (2.8):

$$\tau_{app} + \tau_{fric} = I\alpha \quad (2.8)$$

where  $I$  is the effective joint inertia,  $\alpha$  is the joint angular acceleration,  $\tau_{app}$  is the applied torque by the controller, and  $\tau_{fric}$  is the disturbance torque, which is assumed to be friction. The effective joint inertia is a function of the manipulator configuration, and is defined as the moment of inertia of the links of a manipulator beyond a joint, about that joint. The applied torque ( $\tau_{app}$ ) is the sum of the uncompensated torques commanded to the joint by the controller. In this manipulator, the applied torque (2.9) is the sum of contributions of the PID controllers ( $\tau_{PID}$ ) and the friction compensation torque ( $\tau_{fc}$ ). Disturbance torques come from many sources, such as friction, wind, contact forces, gravity compensation errors, or a user pushing on the manipulator. Because the friction compensation works on a joint level, torque resulting from movement of the other joints is considered a disturbance, as well.

$$\tau_{app} = \tau_{PID} + \tau_{fc} \quad (2.9)$$

The Friedland-Park algorithm identifies the magnitude of the disturbance force ( $\hat{a}$ ) through the use of an observer. It is assumed that all disturbances are the result of friction in the joint, and the algorithm attempts to identify and cancel out this disturbance. The algorithm will converge to the actual value of the disturbance so long as there is sufficient joint excitation for the observer. For practical purposes, this means that the algorithm will work well whenever the joint is moving, except during an initial learning period. A friction compensation torque is then applied as the estimated magnitude  $\hat{a}$  times the sign of the velocity (2.10) through the control law (2.11). The intermediate variable  $z$  is found using the adaptation law (2.12):

$$\tau_{fc} = \hat{a} \operatorname{sgn}(\dot{q}) \quad (2.10)$$

$$\hat{a} = z - Jk|\dot{q}|^\mu \quad (2.11)$$

$$\dot{z} = k\mu|\dot{q}|^{\mu-1}[\tau_{app} - \tau_{fc}] \operatorname{sgn}(\dot{q}) \quad (2.12)$$

where  $q$  is the joint angle and  $k$  and  $\mu$  are gains tuned for individual joints. In the case of this manipulator, the applied torque less the friction compensation torque is the torque from the PID controllers. In other cases, however, applying a shaping function such as a saturation function, low pass filter, or a gain to the friction compensation torque may be

useful to reduce effects such as chatter. Figure 12 is a block diagram of the adaptive friction compensation algorithm, and shows the inputs and outputs as well as the adaptation and control laws.

The adaptive estimates from this algorithm, as well as the joint velocity and command torque will be recorded for use in a feed-forward algorithm, which will be discussed later in Section 2.3.3. Because the adaptive algorithm treats each joint independently, motions and forces on each joint resulting from the movement of other joints are also treated as disturbances. During position control mode, these disturbances are compensated similar to friction on-line. However, when extracting data for a feed-forward algorithm, these sympathetic motions can lead to inaccuracies in identifying the magnitude of friction at a given time. For this reason, the algorithm works best when only one joint is moving at a time, or the dynamic interactions between joints are minimal. The motions of this manipulator generally fall within these boundaries, but best identification of joint friction may require a short training trajectory of individual joint motions.

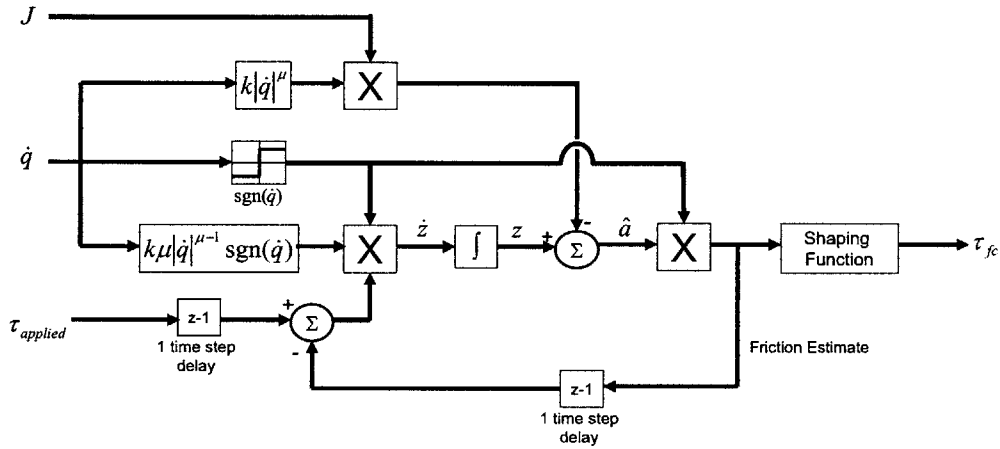


Figure 12: Block Diagram of the Adaptive Friction Algorithm

## 2.3 Insertion Control

The insertion controller is needed because a purely position-based robot would not be capable of performing the insertion task, particularly those having a complex insertion geometry. Without force-feedback from the end effector, the manipulator could possibly damage the payload or the insertion point, or even push the payload through the

wing of the aircraft it is interacting with. Even if care were taken by a user in a purely position-controlled algorithm, the uncontrolled contact forces would render the robot useless for precision maneuvering.

To give the user of the manipulator an interface for maneuvering and inserting the payload by pushing on the robot, a six axis force-sensing handle is located on the robot, mounted on link six, near the payload (see Figure 2). The goal of the insertion controller is to make the robot move the payload in response to these forces as if a human were pushing on the payload with a greatly amplified force. In an ideal case, the control system of the robot would simply make the payload move as if it were greatly lightened, so the user would feel as if he were lifting and inserting something orders of magnitude lighter than the actual payload.

This ideal controller, unfortunately, requires an extremely complex model of the manipulator and payload in order to provide the desired performance. In addition, bandwidth and power limitations limit controller performance. Therefore, an "insertion control" algorithm which simplifies the manipulator response to contact forces but maintains the intuitive nature of the ideal controller is used during the insertion task.

A block diagram of the insertion control mode for joints 1-3 is shown in Figure 13, and a block diagram of the insertion control mode for joints 4-6 appears in Figure 14. As with the position control mode, the user input for both sets of joints is identical, and the differences in the individual joint controllers are a result of differing forms of friction identification and compensation.

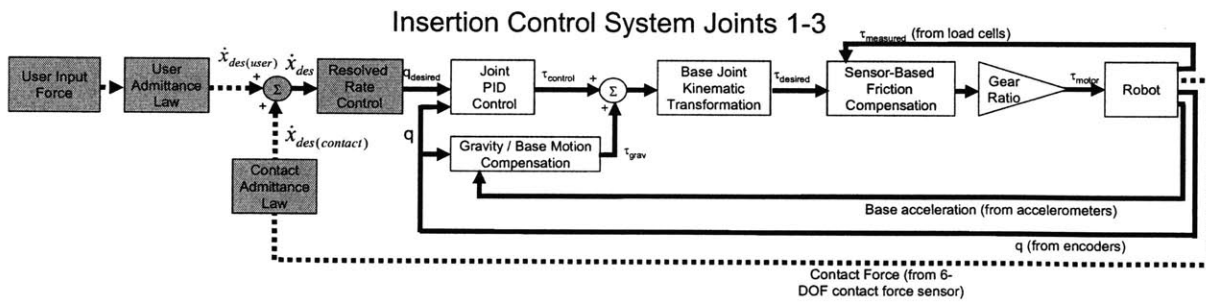


**Figure 13: Block diagram of the insertion control algorithm for joints 1-3. Components not included in the position control algorithm are shown with dotted lines and darkened boxes.**

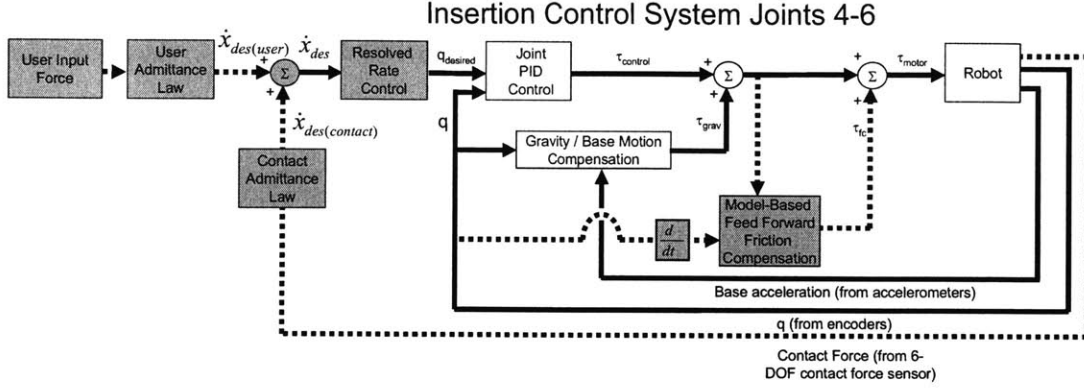


**Figure 14: Block diagram of the insertion control algorithm for joints 4-6. Components not included in the position control algorithm are shown with dotted lines and darkened boxes.**

The user input to the controller in insertion control mode is the user force from a six axis force sensor. This desired force is converted to a desired Cartesian velocity of the payload by an admittance law. When in the manipulator is moving in free space, this is the only input to the controller. When the manipulator comes into contact with the environment, a force sensor located underneath the payload is used to measure the contact force. As described in section 2.1.2, the force measured by this sensor is a combination of the contact force, the weight of the payload, and inertial forces from the payload acceleration. The contact force can be approximated by subtracting the weight of the payload from the force measurements, and neglecting the inertial forces. The approximated contact force is treated as a second input to the controller. This force is also converted into a desired Cartesian velocity by an admittance law, which is added to the velocity from the user input. The combined desired Cartesian velocity is transformed into desired joint velocities through the endpoint Jacobian transform as shown in equation (2.13). It is important to note that this matrix is the Jacobian transform of joint velocities to Cartesian velocities in the end-effector coordinate frame, not in the manipulator coordinate frame as in the position control mode shown by equation (2.3).

$$\dot{\underline{q}}_{des} = J_{endpt}^{-1} \dot{\underline{x}}_{des} \quad (2.13)$$

The desired joint velocities are then integrated into desired joint positions as in the position control mode.

In addition to the input method, the other major difference between the position control mode and the insertion control mode is the different method of friction compensation in joints 4-6. As seen in Figure 13, the friction compensation algorithm in the joints 1-3 is identical to the compensation algorithm in position control mode. Sensor-based torque control friction compensation is stable in the presence of contact forces, and will continue to provide a measure of friction in the base joints. As discussed in section 1.3.3, it is difficult to make adaptive friction compensation stable in the presence of contact forces. Because of this difficulty, a least-squares curve fit of the data recorded from the position control mode adaptive algorithm is used to calculate the parameters of a known friction model. This model is then used to calculate a feed-forward friction compensation torque during insertion control mode. By using only recent friction estimates, the model-based feed forward compensation is able to maintain an accurate model of friction even as parameter values drift.

### 2.3.1 Admittance Control

Admittance control is a name used for a broad range of control algorithms that transform user and environment forces into a desired trajectory response by a robot. Admittance is the dynamic equivalent of compliance, similar to how impedance is the dynamic equivalent of stiffness. Typically, admittance laws transform user or contact forces into desired velocities using a second-order control law, much like a PID controller (2.14)

$$\dot{\underline{x}}_{des} = \underline{F}(A_D s + A_P + A_I \frac{1}{s}) \quad (2.14)$$

Where  $\dot{\underline{x}}_{des}$  is the vector of desired payload velocities in the payload coordinate frame,  $\underline{F}$  is a vector of applied force in the payload coordinate frame, and  $A_D$ ,  $A_P$ , and  $A_I$  are derivative, proportional, and integral admittance laws, respectively. In a robot with perfect tracking, a proportional admittance law would result in a velocity directly proportional to the input force, which to a user would feel like a pure viscous damper. An integral law would result in a velocity proportional to the integral of the force, which to a user would feel like an inertia. A derivative admittance law would result in a velocity proportional to the derivative of the force, which would feel like a spring to a



user. Because no robot has perfect tracking, the viscous/inertia/spring analogy is approximate, but useful for examination of the admittance law. The robot will always have inertia as it accelerates and decelerates, and will have a spring-like force towards its desired position, when position controllers are used.

The best admittance law is not necessarily the one that most closely follows a reference force or position, but the one that responds the most intuitively to the user. Spring-like forces require constant effort from a user, and would likely prove to be a counterintuitive hindrance. Therefore, only admittance laws containing viscous and inertial terms will be considered.

Similar to tuning the joint controllers, the admittance law must be tuned to avoid exciting structural resonant frequencies of the manipulator, as well as resonant modes arising from interaction of the payload and the environment [56,12]. A method of modeling the robot-environment interaction and tuning the admittance controller is detailed in Appendix A. The closed-loop bandwidth of input force to output (contact) force must be limited to a decade below the lowest structural resonant frequency, as well as safely below other resonances which occur in the robot-payload-environment system. This analysis provides a range of stable admittance gains for the environmental interaction. A small amplification gain may be added to the user force without danger of instability.

DiCicco [9] used this model of the robot-payload-environment system to tune stable admittance laws for this manipulator using both purely viscous, and viscous/inertial characteristics. It was demonstrated that, for a similar bandwidth, a viscous/inertial admittance law demonstrated slightly better force following characteristics of the contact force to input force, but also had overshoots in the contact force which might be counterintuitive to a user. The purely viscous admittance law does not have these overshoots, and for a similar bandwidth law, tracked force nearly as well. From a safety standpoint, a purely viscous law also has the advantage that the desired position of the payload will stop moving if a user lets go of the force handle. In a study of another heavy-life manipulator, purely viscous admittance laws met with generally favorable user responses when compared with inertial admittances, especially for lower-speed admittance controllers [36].

Therefore, a purely viscous admittance law is used in this controller (2.15)

$$\dot{\underline{x}}_{des} = A_P(k_{user}\underline{F}_{input} + \underline{F}_{contact}) \quad (2.15)$$

where  $A_P$  is a gain representing a proportional admittance law,  $k_{user}$  is a human amplification gain, and  $\underline{F}_{input}$  and  $\underline{F}_{contact}$  are vectors of forces and torques from the human user and contact sensor, respectively. This law assumes that both user and contact forces are sensed and applied in the endpoint coordinate frame.

Ensuring that the force inputs to the system move the payload in the desired direction is as important as properly tuning the admittance law for stability with the environment. If a contact force causes the manipulator to move in an undesired direction, such as twisting about a point when a pure force is applied, instabilities can occur even with a well-tuned admittance law. The purpose of both the user and contact force sensors are to zero the force applied to the sensors. In essence, this means that the manipulator moves out of the way of both the environment and the user. The most effective way to achieve this control is to transform the desired velocity from the contact force to a desired endpoint velocity. The equations of relative velocity of rigid body motion (2.16) and (2.17) are used for this transformation.

$$\underline{V}_{dE} = \underline{V}_{dS} + \underline{\Omega}_{dS} \times \underline{R}_{E/S} \quad (2.16)$$

$$\underline{\Omega}_{dE} = \underline{\Omega}_{dS} \quad (2.17)$$

where  $\underline{V}_{dE}$  and  $\underline{\Omega}_{dE}$  are the desired endpoint velocities,  $\underline{V}_{dS}$  and  $\underline{\Omega}_{dS}$  are the desired velocities from the admittance law on each sensor, and  $\underline{R}_{E/S}$  is the position vector of the endpoint from the sensor. It is assumed that the orientation of the axes of the sensors is the same orientation as the endpoint frame. Combining equations (2.15), (2.16), and (2.17), the entire admittance law may be summarized as:

$$\begin{bmatrix} \underline{V}_{dE} \\ \underline{\Omega}_{dE} \end{bmatrix} = \begin{bmatrix} k_U \underline{K}_{At} \underline{F}_I + k_U \underline{K}_{Ar} \underline{\tau}_I \times \underline{R}_{E/I} + \underline{K}_{At} \underline{F}_C + \underline{K}_{Ar} \underline{\tau}_C \times \underline{R}_{E/C} \\ k_U \underline{K}_{Ar} \underline{\tau}_I + \underline{K}_{Ar} \underline{\tau}_C \end{bmatrix} \quad (2.18)$$

where  $\underline{V}_{dE}$  and  $\underline{\Omega}_{dE}$  are the desired endpoint translational and rotational velocities,  $\underline{K}_{At}$  and  $\underline{K}_{Ar}$  are the translational and rotational admittance vectors,  $k_U$  is the gain on the user

input, and  $F_I$ ,  $\tau_I$ ,  $F_C$ , and  $\tau_C$  are the forces and torques from the input and payload force sensors. In order to simplify these conversions, the endpoint of the robot used for calculation of the endpoint Jacobian should be the position of the contact force sensor, if possible. These desired velocities in Cartesian space at the endpoint of the manipulator are transformed into desired joint velocities by the use of the Jacobian inverse, and integrated into desired joint positions.

The steady-state behavior of this controller is essentially a damper when operating in free space, and a force amplifier by a factor of the user amplification gain when in contact with the environment. Selection of this amplification gain is a tradeoff between superior rejection of environmental disturbances and movement speed (higher gains), and a better feel for the forces the manipulator is applying to the environment (lower gains). For best results, this gain should be tuned on the robotic hardware to give a user the most desirable "feel" for the manipulator.

### **2.3.2 Friction Compensation**

As mentioned previously, joints 1-3 utilize the same sensor-based torque loop friction compensation during insertion control as they use in the position control mode. However, the adaptive algorithm used in the position control mode for joints 4-6 treats all unmodeled disturbances as friction, and attempts to compensate for those disturbances. This is desirable when the manipulator is operating in free space, as it results in a rejection of all external disturbances. However, if the payload comes into contact with the environment, the adaptive estimate of the friction would continue to climb until the actuator saturated, or the manipulator or environment broke due to the excessive force. This unstable behavior is undesirable, for obvious reasons.

Therefore, model-based friction compensation is selected for these joints when the manipulator is in contact with the environment. The friction in the joints of the manipulator changes over time. The form of the friction was calculated from experimental data in section 2.1.3. The form of this model is repeated here in equation (2.19). Recent data from the adaptive estimators are used to update the parameters of the model, so the feed-forward model tracks the time-varying friction.

$$\tau_{friction} = -\frac{(1 + \alpha_1|\dot{q}|)(\alpha_2 + \alpha_3|C\tau_{motor}| + \alpha_4(C\tau_{motor})^2)}{C} \text{sgn}(\dot{q}) \quad (2.19)$$

The adaptive friction estimate, motor torque, and joint velocity are recorded during the position control mode. Accurate parameter identification of the model requires that the data be cropped to eliminate data points where the estimate of friction is likely to be inaccurate. The sampling rate of the recorded data is reduced for computational speed, data points are removed when joint velocity is near zero, and data is removed during initial learning transients. This cropped recent data is used in a nonlinear least-squares curve-fit to identify the friction model parameters  $\alpha_1$ ,  $\alpha_2$ ,  $\alpha_3$ , and  $\alpha_4$ . The friction compensation torque is then calculated by substituting the current values of motor torque and joint velocity into equation (2.19). As long as the form of the friction model does not change over time, this process will result in frequently updated feed-forward parameters for the model-based feed forward algorithm.

Overcompensation of friction may lead to control instability, but undercompensation of friction only results in increased tracking errors. Therefore, it may be advisable to apply a gain of less than one to the output from the model-based friction compensator to ensure that friction is not overcompensated.

## 2.4 Summary

This chapter detailed the control architecture for use on the heavy lift manipulator. This architecture was broken down into two primary modes: position control and insertion control, which are differentiated by separate forms of control input and friction compensation. This control architecture will be tested in simulations of the full scale heavy lift manipulator in Chapter 3, and on a smaller, reduced complexity laboratory manipulator in Chapter 4.

## **CHAPTER 3: SIMULATION TESTS AND RESULTS**

This chapter contains simulation results of the full-scale heavy lift manipulator. The contributions of this chapter beyond those of [17] and [9] lie in the simulation results of the insertion controller. However, for completeness, some of the position control tests from [17] are repeated. Reference [9] contains some preliminary results of the insertion control system in simulation, primarily with a user modeled as a loose PD controller. This chapter contains several tests that demonstrate some of the fundamental behaviors of the insertion controller, as well as tests that demonstrate the ability of the insertion controller to utilize contact forces to perform a successful insertion using open-loop force commands.

Modeling human responses is difficult, and therefore is avoided in the simulations in this chapter. The simulations in this chapter use open-loop position and force commands to provide an objective evaluation of the control algorithms. Examination of the ability of a human user to utilize these control algorithms in a laboratory manipulator is performed to some extent in Chapter 4. The simulation and laboratory experimental work is valuable, however, when the full-scale hardware is operational, the control algorithms will need to be extensively tested and tuned on that system.

Due to the significantly smaller tolerances and more complex insertion geometry inherent to the light payload, this payload is used as a benchmark for testing the insertion control algorithm rather than the heavy payload. Therefore, all simulations in this chapter are for the light payload.

### 3.1 Description of the Simulated System

The heavy lift manipulator system is simulated by an accurate model constructed in the software package MSC ADAMS. This model, shown in Figure 15, contains accurate kinematic and inertial parameters of the heavy lift manipulator (see Appendix E), as well as a gravitational field. During the insertion control tests, the model also contains simulated insertion geometry and a modeled contact force between this geometry and the payload of the manipulator. The insertion geometry is modeled as a section of a “wing” of an aircraft with a slot running the length of the wing, and the payload is a simplified 2-lug approximation of the actual payloads to be handled by the manipulator. Inputs to this plant model are the six joint torques. The outputs from the system are the joint positions, accelerations of the base of the manipulator, and the 6-axis force measurement from a contact force sensor. Due to the complex nature of the joint friction, joint friction is implemented in the software package Simulink. The controller for this plant, as well as the open loop user inputs, are also constructed in Simulink. The Simulink controller uses a discrete step size solver running at a rate of 1 kHz. See Appendix A for gains and parameters of the controller.

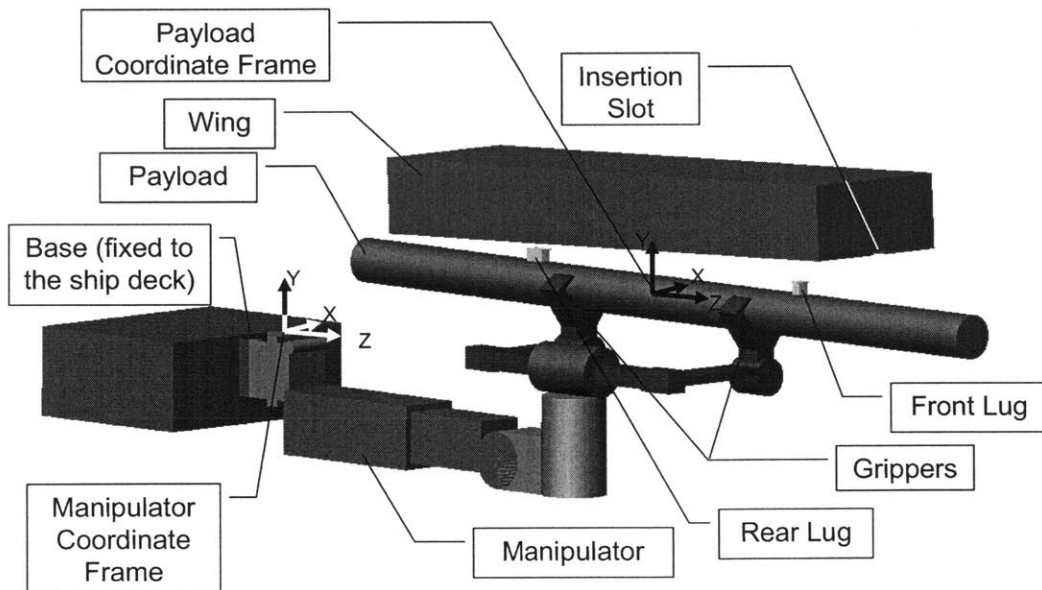


Figure 15: Simulation model of the heavy-lift manipulator

Unless otherwise stated, the following assumptions are valid during the simulations:

1. The geometric and inertial parameters of the manipulator and its payload are exactly known by the position controller (see Appendix E).
2. All sensor measurements are 100% accurate and noise-free.
3. All simulated command inputs are smooth
4. There is no simulated ship motion.
5. Joint motors deliver commanded torques perfectly and instantaneously (“torque ripple” effects are neglected).
6. The payload of the robot is the 156 kg 'light payload' which is secured to the manipulator with a compliant gripper (See Appendix E).
7. The insertion geometry of the lugs and slot is slightly simplified from the actual case. Instead of the three lugs of the actual payload, the payload uses two lugs representative of the front and rear lugs of the actual payload (see Figure 16). The simplified insertion geometry is a single slot running the length of a 2 meter long simulated wing. Table 1 shows the tolerances for the actual and the simulated payload. The tolerances of this simplified system are identical to the tolerances of the actual system in the payload X direction, with the exception that the simulation insertion point for the rear lug does not have a chamfer to aid insertion. The insertion tolerance in this direction is tighter than the tolerance in the Z direction by an order of magnitude. Therefore, the simulated geometry is representative of the most challenging dimension of the insertion task. It is assumed that a user would be able to align the lugs of the manipulator in the payload Z direction, so a slot with no constraints in the payload Z direction is a reasonable simplification.

**Table 1: Tolerances for the insertion geometry for the actual and simulated payloads.**

Payload	Front Lug X direction	Front Lug Z direction	Rear Lug X direction	Rear Lug Chamfer (X)	Rear Lug Z direction
Actual	3.61 mm	20.83 mm	4.74 mm	3.18 mm	123.19 mm
Simulation	3.61 mm	N/A	4.74 mm	0 mm	N/A

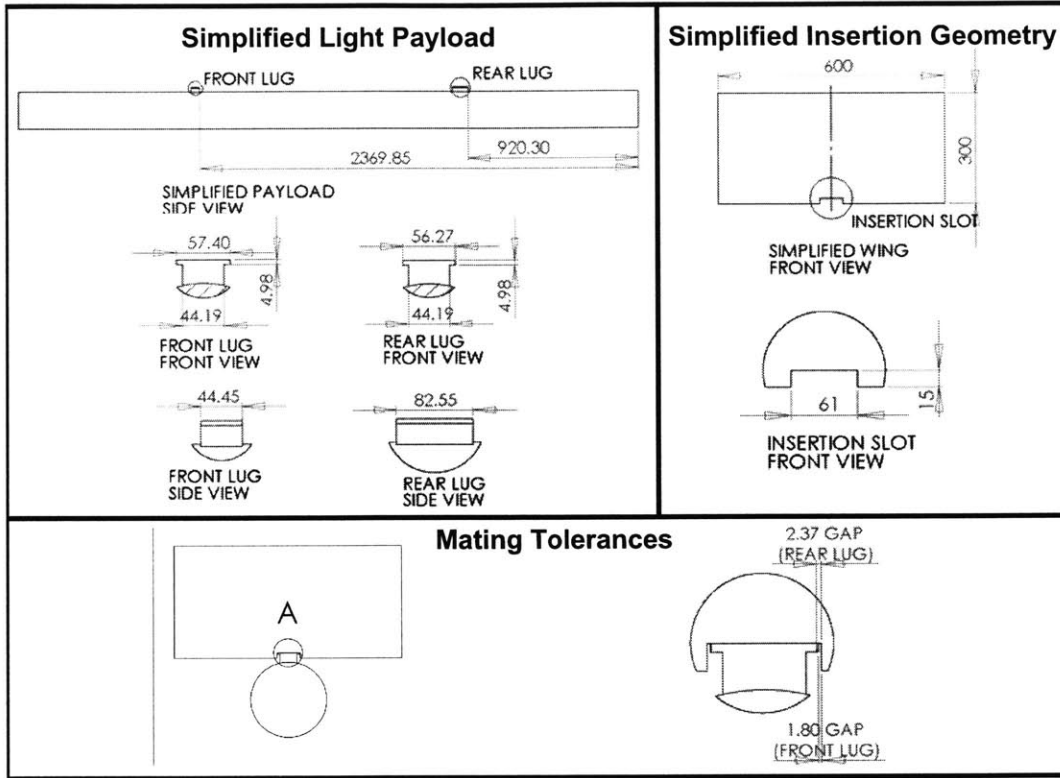


**Figure 16: Simplified payload and insertion geometry used in the simulations. All measurements are in millimeters.**

### 3.2 Position Control Simulations

In reference [17], a detailed simulation investigation of the position control mode was performed for both the heavy and light payloads. The trajectory tracking performance of the manipulator during these tests was shown to be within desired specifications, and the incorporation of independent friction compensation greatly improved the performance of the manipulator. In this section, these results will be revisited, with particular focus on the use of the adaptive friction estimators in the extraction of a feed-forward model of friction to be used in contact with the environment.

#### 3.2.1: The Representative Task

In order to determine that the position control algorithm maintains an acceptable tracking error, and the adaptive algorithms can be used to extract a model of friction from ordinary movements of the manipulator, a task representing a standard payload maneuver was determined. The trajectory of the endpoint of the manipulator during the



representative task is shown in Figure 17, and images of the simulated manipulator during this task are shown in Figure 18.

In this task, the manipulator begins parallel to the deck of the ship (Point A) with joint 5 set to  $30^\circ$  to avoid a singular configuration. From 0-5 seconds, the endpoint of the manipulator is then raised straight upwards under Cartesian control to point B, where the payload would be acquired. After holding for two seconds, the manipulator then performs a "crossover" maneuver under joint control in which joint 6 is actuated  $180^\circ$  to point C (7 sec - 32 sec). After another short pause, the manipulator then rotates the payload about the yaw (Z) axis and translates it in the positive Y direction to point D (33 - 42 sec). The payload is then lowered and rotated about the X axis into point E, a low center of gravity "transportation" position (43 - 48 sec). The manipulator joints would then be locked, and the omni-directional vehicle the manipulator is mounted on would be driven to the side of aircraft. The payload is then translated in the positive Y and Z directions, bringing the payload to point F, within 5 centimeters of the insertion point (49-54 sec). This is the end of the position control representative task. The user would then select the insertion control mode, and move to the force handle near the end-effector of the manipulator, and insert the payload into its slot.

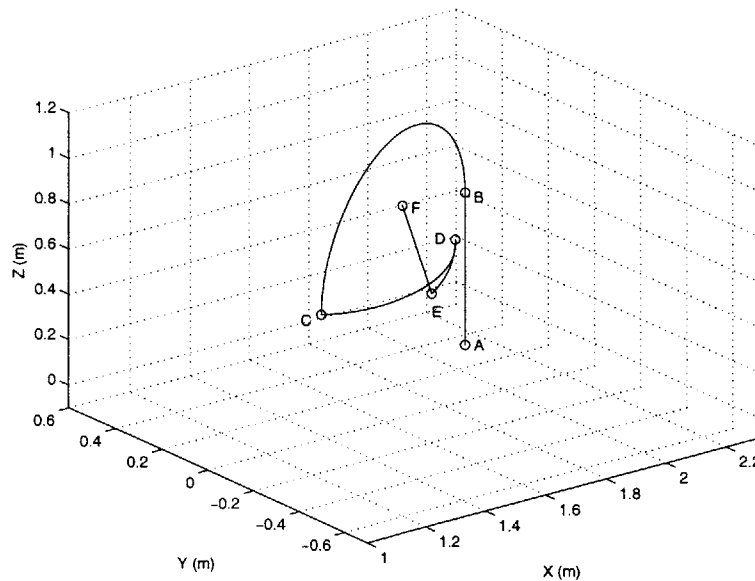
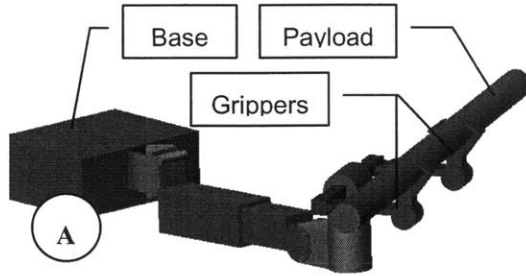
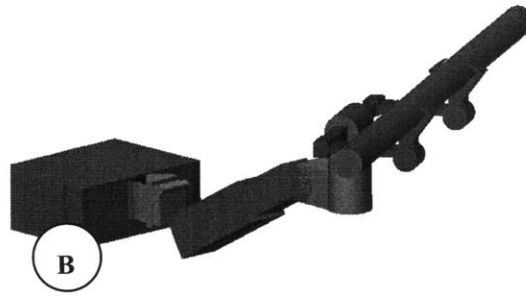


**Figure 17: Endpoint trajectory during the representative task for the light payload (from [17]). The trajectory is shown in the manipulator coordinate frame.**

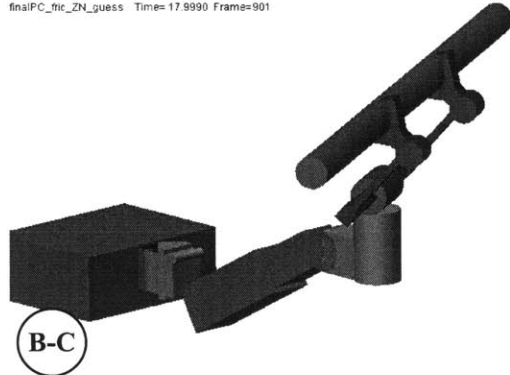
finalPC\_fric\_ZN\_guess Time= 1.9990 Frame=101



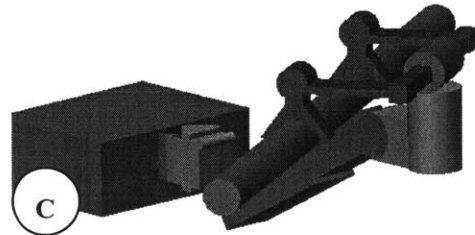
finalPC\_fric\_ZN\_guess Time= 5.9990 Frame=301



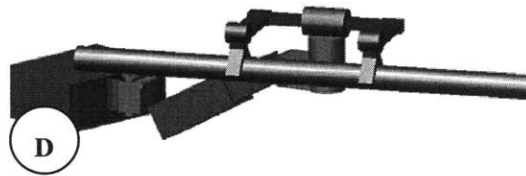
finalPC\_fric\_ZN\_guess Time= 17.9990 Frame=901



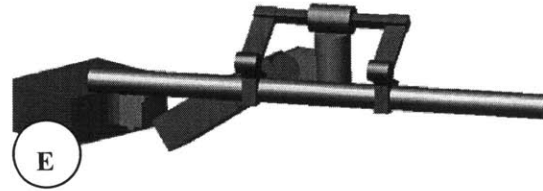
finalPC\_fric\_ZN\_guess Time= 31.9990 Frame=1601



finalPC\_fric\_ZN\_guess Time= 41.9990 Frame=2101



finalPC\_fric\_ZN\_guess Time= 51.9990 Frame=2601



finalPC\_fric\_ZN\_guess Time= 55.9990 Frame=2801

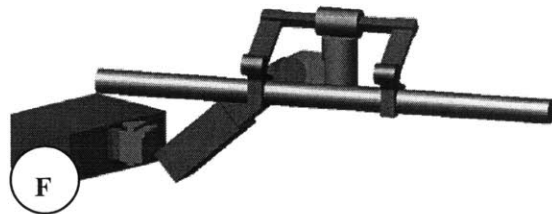


**Figure 18: Manipulator poses during the representative task**

A goal of the position control mode is to keep the endpoint of the manipulator within 2.5 cm of the desired trajectory. Meeting this goal is a good indication that the user will be able to maintain control of the manipulator and move the payload in

sufficiently precise manner during position control mode. Dynamic simulations of the representative task performed by a frictionless manipulator, manipulator with uncompensated joint friction, and a manipulator with friction compensation are used to evaluate the performance of the control algorithm. These simulations show the ability of the manipulator to follow the representative trajectory, demonstrate the necessity of friction compensation, and provide a metric for evaluation of the position controller. In addition, the adaptive friction estimator outputs from the representative task simulation are used to calculate the parameters for a feed-forward model of friction as described in section 2.3.2.

The tracking error during the representative task is used as a performance metric of the manipulator. The tracking error is defined as the endpoint position perpendicular to the desired trajectory, so lag in the manipulator tracking does not factor into the metric. Figure 19 shows the tracking error of a frictionless manipulator, and the tracking error of the manipulator with uncompensated joint friction in all joints for the representative task. The frictionless manipulator easily meets the requirement of a maximum tracking error of 2.5 cm. However, with friction in the joints, the manipulator cannot meet this tracking requirement.

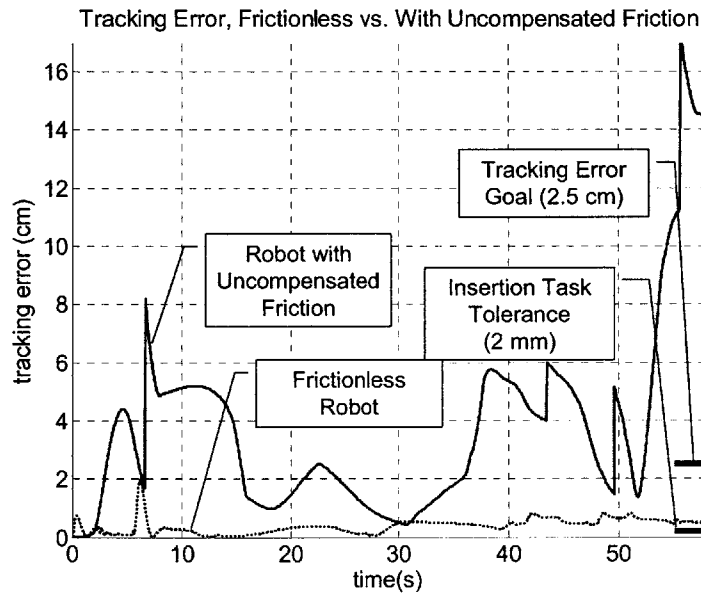


**Figure 19: Tracking error comparison for the representative task, no friction in the manipulator vs. manipulator with uncompensated friction**

All motions of the manipulator with uncompensated friction result in tracking errors well above the 2.5 cm specification. In particular, high tracking errors occur near the beginning of the joint 6 "crossover" maneuver around 7-16 seconds, and the slow motion as the payload is moved near the plane after 50 seconds. These high tracking errors demonstrate the necessity of friction compensation in the joints of the manipulator in order for the manipulator to be controllable, even during position control mode.

Section 2.2.3 describes the two forms of friction compensation used in the joints of the heavy-lift manipulator during position control. In order to evaluate the ability of these friction compensation algorithms to reduce the effects of friction in the joints of the robot, the performance of a robot with friction compensation is compared to the performance of a frictionless robot. Figure 20 is a plot of the tracking error of these two robots during the representative task.

Implementing friction compensation dramatically improves the performance of the robot. The tracking errors of the robot with friction compensation are only slightly higher on average than the frictionless robot, and far smaller than the errors which occur in the robot with uncompensated friction. The largest tracking errors which occur with friction compensation occur when the payload is lowered to the "transportation" position from 38-42 seconds, and during the motion as the payload is moved near the aircraft from 48-54 seconds. However, even these largest tracking errors are only about 1.6 cm, well within the position control mode goal of 2.5 cm. Examining Figure 20 also shows that the accuracy of the controller appears to be insufficient to insert the payload using a purely position based controller, even with perfect knowledge of the insertion geometry. This clearly demonstrates the need for a controller that can use contact interaction with the environment to aid in the insertion of the payload.

One unusual result seen in Figure 20 is that the frictionless robot has a spike in the tracking error at approximately 5 seconds, at the end of the first motion of the representative task. A similar spike is not seen in the manipulator with friction compensation. This error is a result of overshoot from the underdamped joint controllers as the manipulator comes to a stop. In the robot with friction compensation, the peak error at this point is lower because the presence of some uncompensated friction in the

joints reduces overshooting behavior. The magnitude of this error is still below the 2.5 cm tracking error goal, and the error dissipates quickly.

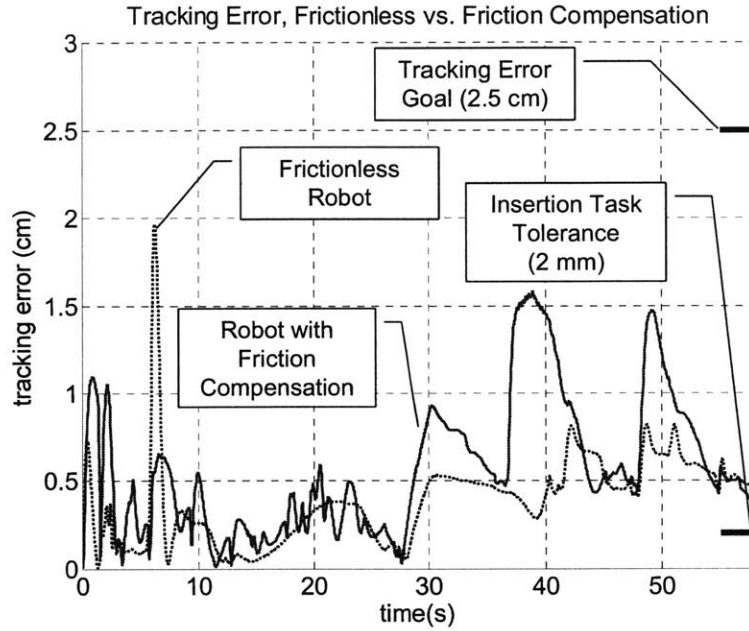


Figure 20: Tracking error comparison for the representative task, no friction in the manipulator vs. manipulator with compensated friction

### 3.2.2: Friction Model Extraction

During position control mode, estimators are used to identify and compensate for the friction in joints 4, 5, and 6 of the manipulator. This friction estimate, if sufficiently accurate, can be used to calculate parameters of a feed-forward model of friction for use during insertion control mode. The model of friction for these joints is a function of joint velocity and the load on the motor. The estimate of the friction from the adaptive compensator, the joint velocity and the applied torque of the motor are recorded during the position control task. When the insertion algorithm is used, recently recorded data is then fit to the known friction model, and the parameters of the model are identified. The accuracy of this curve-fit is dependent upon two factors: the accuracy of the friction estimate, and the richness of the trajectory used to gather the data used in the curve fit. Figure 21 compares the estimate of the friction in joint 6 during the representative task, as well as the actual friction in the joint. The friction tracking performance of joint 6 is

representative of the performance seen in the other two joints utilizing the adaptive friction estimation.

The adaptive estimators require motion of the joint in order to accurately track friction in both an actual manipulator and in simulation. The simulation model of friction multiplies the magnitude of the friction by the negative sign of the velocity. The model results in a high frequency alternation of the sign of the velocity when the joint velocity is near zero. As a result, the joint friction represented by the dotted line in Figure 21 appears to be noisy about zero velocity. When the joint is moving, the estimate, represented by the solid line, can be seen to accurately track the friction in the joint. The largest inaccuracies in this estimate of friction occur during learning transients at the beginning of motion. These transients occur in the joint 6 compensator around 12 seconds, 39 seconds, and 49 seconds.

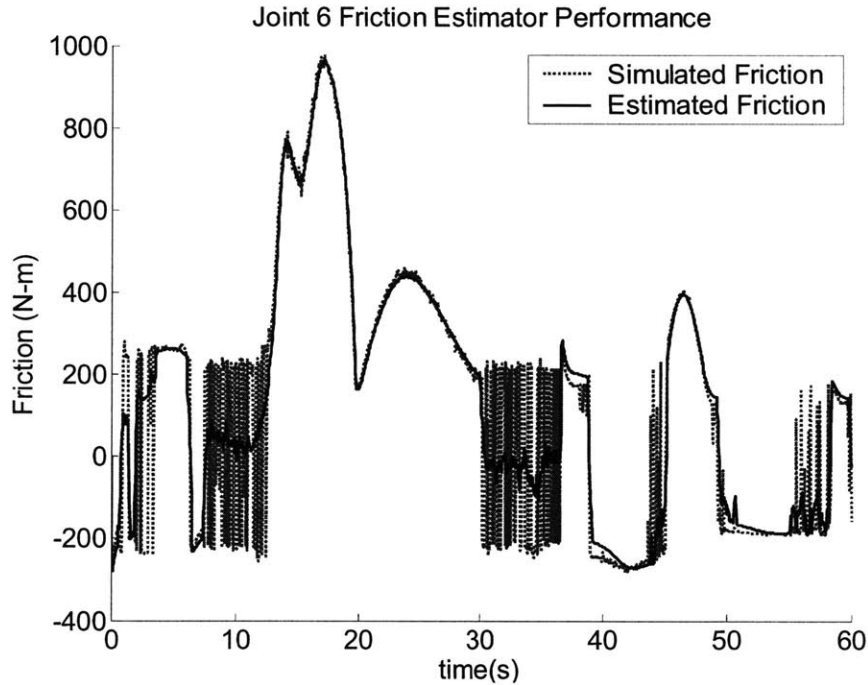


Figure 21: Friction estimator performance in joint 6 during the representative task

To ensure the accuracy of the feed-forward model of friction, the data used in the curve fit must be cropped so that inaccurate estimates of friction are not used in the curve-fit process. Therefore, data from when the joint velocity is below a certain

threshold is cropped to eliminate the noise in the estimate which occurs at low speeds. Additionally, the data from the learning transients must be eliminated. Finally, the data is sampled less frequently than the controller frequency for computational speed. In actual practice, the data used in the curve fit would encompass several cycles of the manipulator. This ensures a richer selection of data to fit to the model of friction, and reduces the effect of temporary disturbances on the adaptive compensator estimates.

To evaluate the ability of the adaptive estimators to compute a feed-forward model of friction, the data from the representative task is cropped and fit to the known form of friction (3.1).

$$\tau_{friction} = -\frac{(1 + \alpha_1|\dot{q}|)(\alpha_2 + \alpha_3|C\tau_{motor}| + \alpha_4(C\tau_{motor})^2)}{C} \text{sgn}(\dot{q}) \quad (3.1)$$

where C equals 8.8504. In this case, the data from the adaptive estimators is sampled at 20 Hz. Data points are then removed if the joint velocity at the point is below a cutoff threshold to eliminate the estimator noise about zero velocity. In joint 4, this threshold is 0.03 rad/s, and in joints 5 and 6 the threshold is 0.005 rad/s. Data is also removed if the point is less than 1 second after a joint has started from rest or changed direction, to eliminate transient estimates. The cropped data from the adaptive estimators during the simulated representative task is sufficient to provide good parameter estimation of the friction model. The parameters used to simulate friction during the representative task, as well as the identified parameters from the curve-fit are shown below in Table 2.

**Table 2: Actual and extracted curve-fit parameters of friction from the representative task simulation. The data used in the curve-fit identification is cropped to eliminate inaccurate points.**

Joint	Simulated/Extracted	$\alpha_1$ (s/rad)	$\alpha_2$ (Nm)	$\alpha_3$ (no dim)	$\alpha_4$ (N <sup>-1</sup> m <sup>-1</sup> )
4	Simulated	10	500	0.187	-1*10 <sup>-6</sup>
4	Extracted	9.78	484.4	0.184	-7.2*10 <sup>-7</sup>
5	Simulated	10	150	0.187	-1*10 <sup>-6</sup>
5	Extracted	12.03	122.6	0.160	-2.6*10 <sup>-6</sup>
6	Simulated	10	350	0.187	-1*10 <sup>-6</sup>
6	Extracted	10.7	335	0.177	-1.3*10 <sup>-6</sup>

The parameters identified in Table 2 are close to the actual parameters of friction used in the models. The accuracy of the extracted models is evaluated in two ways: comparison of the accuracy of the extracted model of friction to the actual model of friction at the points used in the curve-fitting process, and over the entire expected range of the friction model. Table 3 lists the percent and total errors between the extracted friction model and the simulated friction model using the velocity and torque values of the data points used in the curve-fit. Typically, these points will be the points at which the extracted friction model will be most accurate.

The results in Table 3 show that at these points, the model of friction is accurate to within less than 1.5% of the actual friction in joint 4, and within 5% in joint 6. Joint 5 has, at first glance, significantly higher error of up to 17%. However, the magnitude of friction in joint 5 is significantly lower than the magnitude of friction in the other joints, and the maximum total error of friction is only an error of 5.8 Nm. This value of friction is small enough to be easily compensated by the PID joint controllers in the absence of perfect friction compensation. The maximum friction magnitude errors in the other two joints are also quite small.

**Table 3: Error of the extracted friction model from the simulated friction model at the points used in the curve-fit**

Joint	Percent Error		Total Error	
	Mean	Max	Mean	Max
4	1.03%	1.4%	6.4 Nm	12.3 Nm
5	8.9%	16.8%	4.3 Nm	5.8 Nm
6	2.8%	4.8%	7.5 Nm	12.3 Nm

This initial analysis demonstrates that the curve-fit value of friction is a good estimate of the actual value of friction at the points used to make the curve-fit. This result could be expected from examining the excellent friction tracking ability of the adaptive estimators illustrated in Figure 21. A better analysis of the accuracy of the curve-fit model is to compare values of the curve-fit model to the values of friction from the actual model over the expected range of operation of the joint. Figure 22, Figure 23, and Figure 24 show the percent error of the curve-fit model from the actual friction for joints 4, 5, and 6, respectively. This modeling error is the error between the value of



friction from the curve-fit model and the model of friction used in the simulation divided by the simulated friction. These plots show the modeling error for the entire velocity range of each joint, and a maximum torque load equal to 150% of the maximum recorded joint torque during the position control motion. These values represent realistic bounds for the friction model likely to be used in an insertion task with this payload. Negative values of friction percentage error represent values of load torque and velocity where the model undercompensates for joint friction, and positive values of this error represent cases where the model overcompensates for friction.

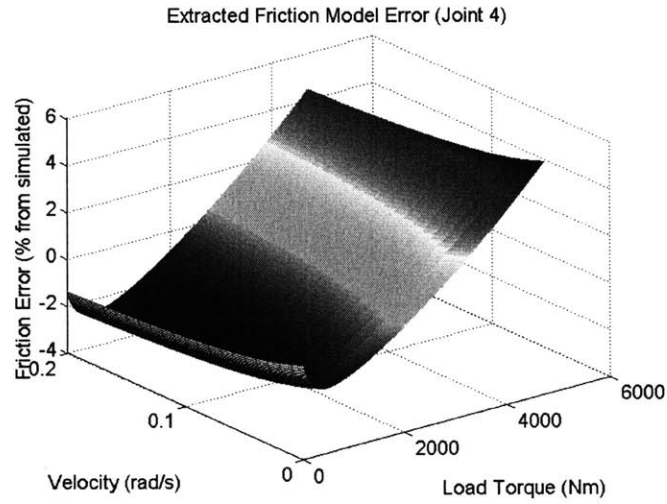


**Figure 22: Curve-fit accuracy of the extracted friction model from joint 4**

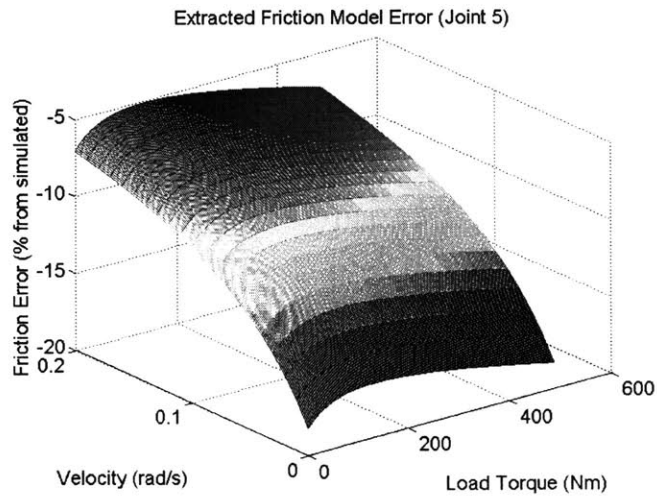


**Figure 23: Curve-fit accuracy of the extracted friction model from joint 5**

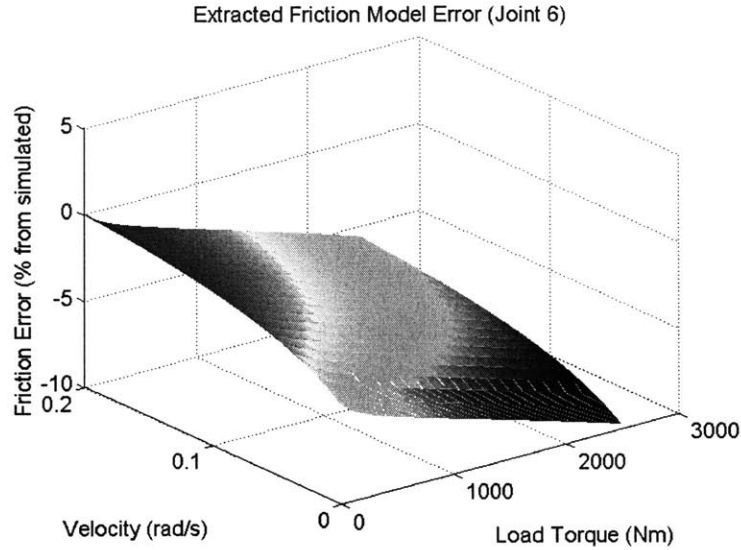


**Figure 24: Curve-fit accuracy of the extracted friction model from joint 6**

**Table 4: Percentage error of the curve-fit model from the actual value of friction over the expected range of operation**

Joint	Max Negative Error	Mean Error	Max Positive Error
4	-2.6%	0.54%	5.9%
5	-18.3%	-8.2%	N/A
6	-9.6%	-4.4 %	3.2%

The maximum and mean values of friction modeling error for the three joints are shown in Table 4. Combined with the plots of the error, these values provide a good metric of the ability of the outputs from the joint-level adaptive estimators to be used to calculate the parameters of the friction model. The models from both joint 4 and 6 are within 10% of the actual value of friction over their entire expected range. The data from each of these joints was within 1.5% and 5%, respectively, at the points used in the curve-fit, so it is likely that multiple trajectories and a richer data set would lead to further improvements of these already accurate models. The model of friction of joint 5 has significantly larger errors, as expected. However, the modeling error is at most 18.3% less than the actual friction in the joint, and the model will not overcompensate for friction at any point. As stated previously, the magnitude of friction in joint 5 is

significantly smaller than the magnitude of friction in the other joints, and these errors will likely be compensated by the PID joint controllers. The data in Table 4 demonstrates that the data from the adaptive estimators can be used to construct a model of friction which can be used in a feed-forward algorithm to compensate for at least 80% of the friction in each joint.

The plots of the friction modeling error for all three joints show that the models generally undercompensate for friction. As previously stated, this is desirable behavior, because overcompensated friction leads to manipulator instabilities, and undercompensated friction leads only to an increase in tracking errors. When the model-based feed-forward friction model is used during insertion control, a gain slightly less than one should be applied to the estimated magnitude of friction, in order to ensure that the friction compensation torque is always equal to or lower than the actual magnitude of friction. Examining the data from the representative task, a gain of 0.94 would be sufficient to ensure stability.

In this section, the need for dedicated friction compensation architecture was demonstrated for the manipulator under position control. The position controller demonstrated acceptably small tracking errors when friction compensation was implemented on the manipulator. The output from these adaptive estimators was then used to formulate feed-forward models of friction for use in joints 4, 5, and 6 when the manipulator is in contact with the environment. The maximum error in these models was less than 20% of the total magnitude of friction, and in almost all cases the error was significantly lower. Utilizing this process to continually update the model of friction should allow the feed-forward model to vary over time as the joints of the manipulator degrade. In the next section, the ability of the insertion control algorithm will be evaluated by testing its ability to utilize contact forces to allow an insertion of the payload using open-loop user inputs with imperfect joint friction compensation.

### ***3.3 Insertion Control Simulations***

The insertion control mode of the manipulator allows a user to utilize contact forces with the environment to perform the insertion task. All of the insertion control simulations use the simplified 2-lug payload and slot insertion geometry described in

section 3.1. For detailed drawings of this payload and geometry, see Appendix F. Contact friction is modeled with a static coefficient of 0.31, and a dynamic coefficient of 0.26, which are representative of a steel-on-steel contact (see Appendix A for simulation parameters).

As described in section 2.3.1, an admittance law is used to calculate the desired velocity of the manipulator from the measured user input and contact forces. In appendix A, a model of the robot and environment interaction is used in order to calculate a stable contact admittance law. It is determined that translational admittances of  $7.2 \cdot 10^{-5}$  m/s/N or less have bandwidth safely low enough to avoid excitation of structural resonances of the manipulator and robot-environmental interaction. A rotational admittance of  $30.0 \cdot 10^{-5}$  rad/s/Nm or less is similarly safe.

In the actual manipulator, the individual admittances for each direction should be tuned within these safe values based upon the user's "feel" of the manipulator. Tuning the admittances by the user input ensures that the user does not feel that the manipulator does not feel too responsive in some directions, and sluggish in others. As explained in section 2.3.1 and appendix B, a small gain on the user input can be used to speed up the manipulator response to a user while maintaining a stable admittance to the environment. In the simulations in this section, a translational contact admittance law of  $7.0 \cdot 10^{-5}$  m/s/N, rotational contact admittance law of  $7.0 \cdot 10^{-5}$  rad/s/Nm, and a user gain of 5 are used to calculate the desired manipulator endpoint velocity. A simulated force sensor is placed at the endpoint of the robot (the end of link 6) to feed back the forces acting on the payload to the controller. The weight of the payload is removed from this signal, and inertial forces are assumed to be negligible. The user input to the system is a 6-axis force and torque in the coordinate frame of the endpoint of the manipulator. As mentioned in section 2.3.1, excessive integral control can lead to unstable limit cycling when in contact with the environment. Therefore, the integral gains on the joint controllers are turned off during insertion control mode.

The friction in the joints of the manipulator is implemented in the same way as in the position control simulations. Friction compensation is identical in joints 1-3. Unless otherwise specified, the friction in joints 4-6 is reduced by 80%, which is a reasonable estimate of the performance of the ability of the feed-forward model from the adaptive

estimators to reduce friction. The surface contact is modeled as a spring-damper system with a stiffness of  $2.7 \cdot 10^6$  N/m and a damping of  $5 \cdot 10^3$  Ns/m. The coefficient of static friction of the surface contact is 0.31, and the coefficient of dynamic friction is 0.26.

Four tests are used in order to evaluate the performance of the insertion control. The force impact test demonstrates the stable nature of the insertion control algorithm as the manipulator end-effector is pushed upwards into a simulated flat "wing", and comes to rest. The endpoint spiral test demonstrates the ability of the controller to respond to fine user input forces when in contact with the environment. The zero rotation insertion test demonstrates the ability of the insertion controller to use the environment in order to aid a user in an insertion task, as well as the ability of the controller to push the payload down a slot when the user is pushing in an offset direction. The compliant insertion test shows the ability of the controller to use environmental forces to aid a user in an insertion task, even when the payload is misaligned with its insertion geometry.

### **3.3.1 Force Impact Simulations**

This test demonstrates the stable interaction of the payload and environment as a user pushes a payload up into a simulated wing. The payload is simply lifted from a horizontal position into contact with the environment with a constant user force. The manipulator begins parallel to the ground (Figure 25A). After a few seconds of movement in free space, the payload contacts the environment. The payload then comes to rest and the contact force stabilizes as the user input force and contact force offset each other. The user is pushing upwards with a force of 100N with a user gain of 5. Therefore, the necessary contact force to offset this force is 500N. The user begins pushing upward at 3 seconds. Because of the uncompensated joint friction in the manipulator, one lug of the manipulator hits slightly before the other (Figure 25B), at about 4 seconds into the simulation. At 4.5 seconds, the second lug impacts the wing, and the controller levels the payload using the contact force (Figure 25B and Figure 26A). After 4.5 seconds, the user continues to push up on the manipulator, and the desired endpoint position moves into the wing, as seen in Figure 27. The error between the actual and desired position increases the contact force approaches a steady-state value of the user input force multiplied by the

user gain. As the contact force increases, the joint errors increase. This is particularly noticeable in joint 6 (Figure 26B).

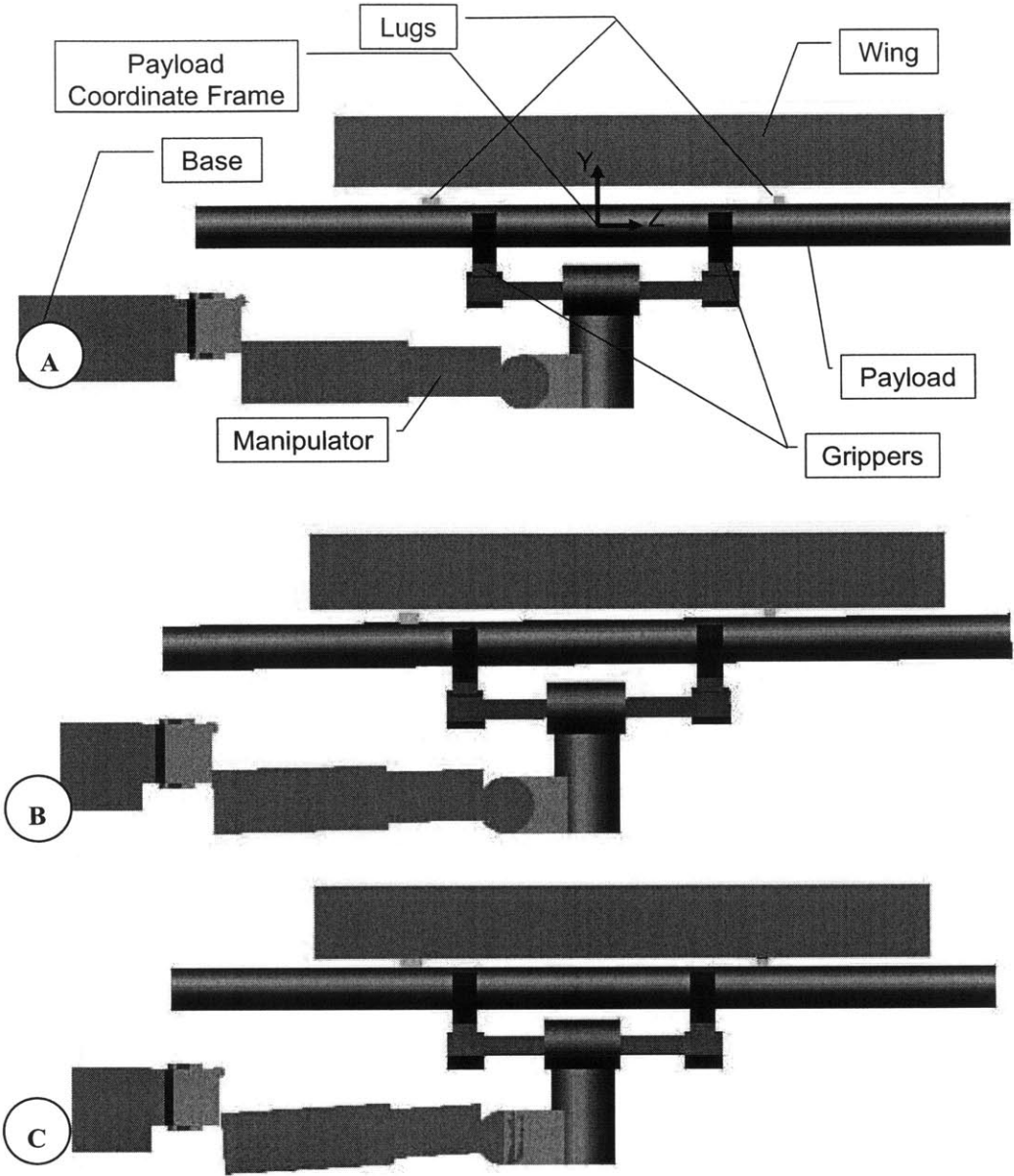
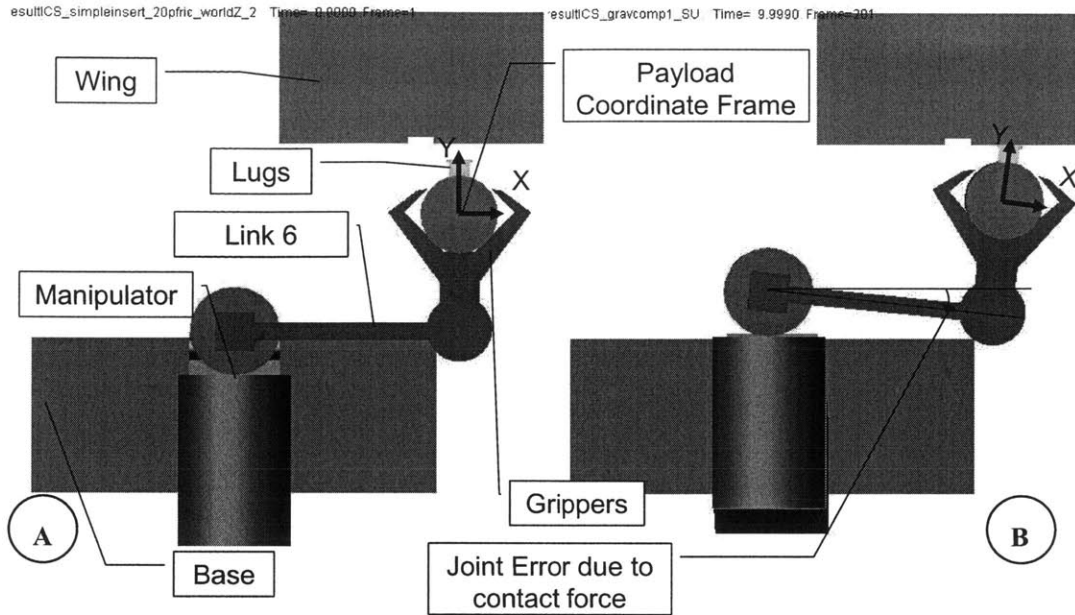
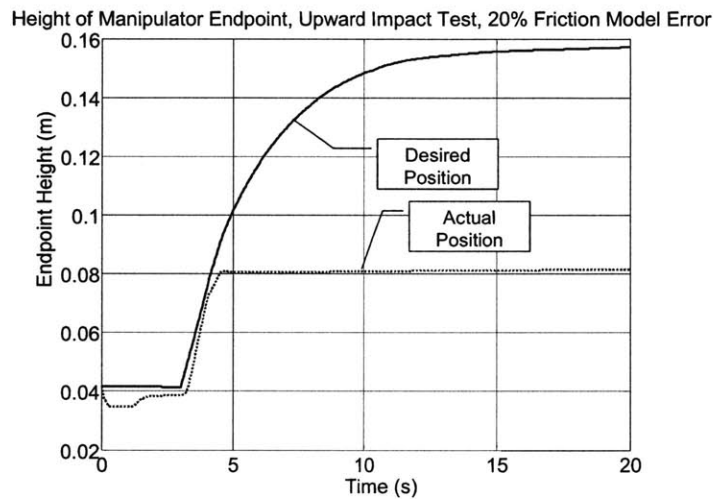


Figure 25: Side view of the upward force impact simulation



**Figure 26: Front view of the upward force impact simulation**



**Figure 27: Desired and actual endpoint positions of the manipulator in the manipulator Z (vertical) direction for the force impact test with 20% uncompensated joint friction in joints 4-6**

Figure 28 shows the contact and input forces in the vertical direction during this test. The contact force can be seen to approach 500 N, equal to the user gain of 5 multiplied by the user input force of 100 N, as expected. This illustrates the characteristic of the manipulator that it is a force amplifier at steady-state by a factor of the user gain.

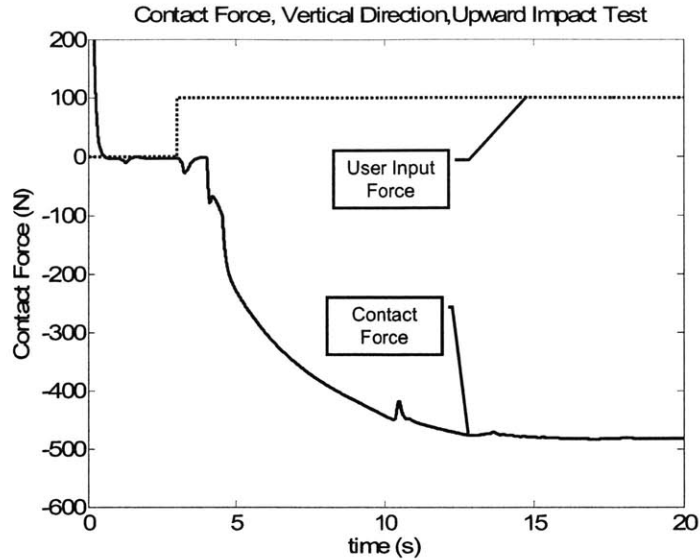


**Figure 28: Contact force in the payload Y direction (roughly normal to wing) for the force impact test with 20% uncompensated joint friction in joints 4-6**

Figure 29 illustrates the differences that occur during this simple impact test as the ability of the feed-forward model to compensate for friction is varied. Two distinct characteristics can be observed as the level of uncompensated joint friction is raised. The first is that the angular error of the payload about the payload X axis during the initial raising motion increases, causing the two lugs to hit at more disparate times. The second is that as uncompensated joint friction is increased, the contact force immediately after impact is larger, indicating that the desired position of the manipulator is further inside the wing at the moment of impact. This indicates that, as one would expect, free space tracking errors are larger in the cases with higher joint friction. However, all of the cases demonstrate stable behavior with the environment during these simulations.

It should be noted that the behavior of the manipulator during these simulations is not exactly as desired. The contact force from the environment results in small joint errors, particularly in joint 6, as shown previously in Figure 26B. However, this is to be expected when employing purely open loop force commands, and an actual user would be able to feel and see this angular error, and apply a rotational torque to align the payload vertically.



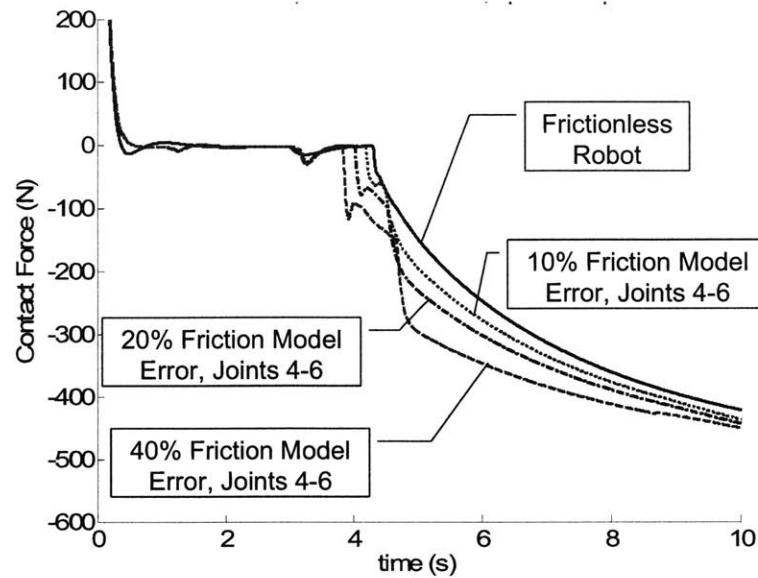
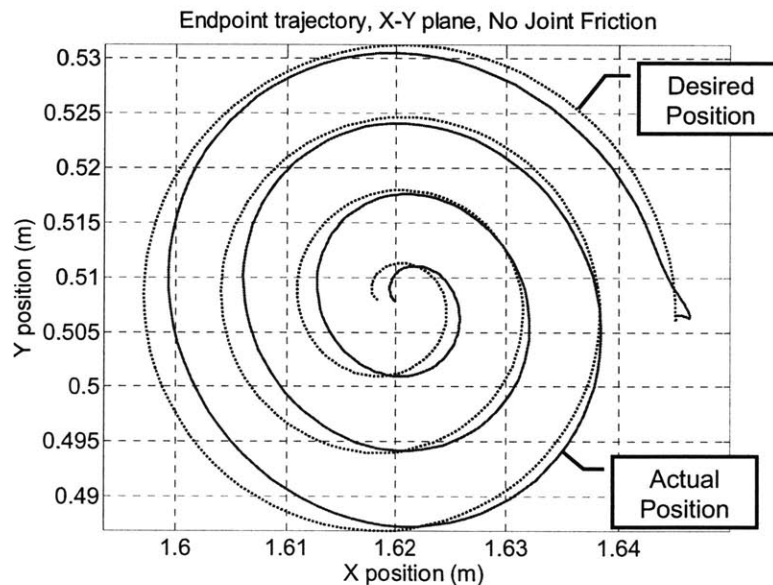


Figure 29: Comparison of contact force in the manipulator Z direction during the force impact simulation for several values of joint friction compensation

### 3.3.2 Endpoint Spirals

Due to the tight tolerances of the payload insertion geometry, the user of the manipulator must be able to make fine adjustments to the endpoint position of the manipulator when it is in contact with the environment in order to successfully insert the payload. In this simulation, the payload is lifted into contact with a wing, as in the previous simulation. The upward force is then reduced to 25N for the remainder of the simulation. For 15 seconds, an additional user force is applied in the Z-X plane of the payload axes. This force increases from 0 to 120 N at a constant rate, and the direction of the force rotates within the Z-X plane every 4 seconds. This force input should result in an expanding spiral motion of the manipulator endpoint. The purpose of this test is to observe the ability of the manipulator to follow a quickly changing desired user input when it is in contact with the environment. The desired and actual manipulator endpoint trajectories are monitored during this test in order to evaluate the ability of the manipulator to follow a desired user force. The actual tracking accuracy of the manipulator is a secondary concern to the ability of the manipulator to move in the same direction as the user input.

Figure 30 shows the desired and actual endpoint trajectory response to the spiral force input in a frictionless manipulator for the 15 second force application in the manipulator coordinate frame. It can be seen that the manipulator follows the desired trajectory closely. Even in this frictionless manipulator, tracking errors approach the tightest insertion tolerance of 3.18 mm. However, in insertion control mode, the magnitude of the tracking error is not an accurate measure of performance. The user of the manipulator does not know how close the manipulator is to its desired point; he only knows how well the manipulator responds to his commands. Figure 30 shows that the directional response of the frictionless manipulator is good, even in the presence of surface friction and environmental contact. During position control mode, the manipulator should be brought to within 2.5 cm. of the insertion point. Figure 31 shows the ability of the manipulator under insertion control to cover an area of the wing during the spiral input test using the tolerance of the chamfered insertion slot. This tolerance is approximately 5 mm. combining the insertion tolerance and the dimensions of the chamfer. The physical meaning of this coverage is that if the payload begins within an inch of its insertion point, the user will be able to find the insertion slot, even without visual feedback. From this point, the contact forces can be utilized by the user to perform a successful insertion, as will be shown in sections 3.3.3 and 3.3.4.



**Figure 30: Desired and actual endpoint trajectories in a frictionless manipulator during the contact spiral test**

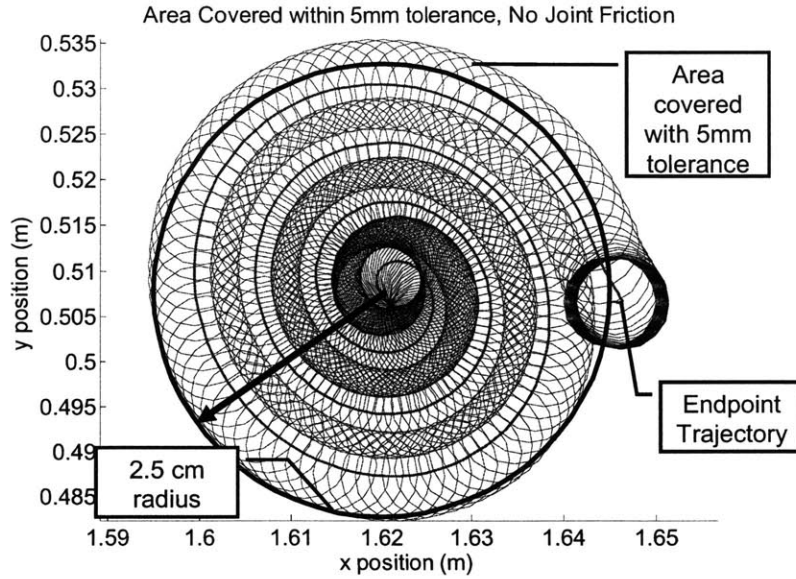


**Figure 31: Area covered with a 5mm tolerance for a frictionless manipulator during the contact spiral test**

Figure 32 shows the actual and desired trajectories to the same input of a manipulator with sensor-based friction compensation in joints 1-3, and a feed-forward model which compensates for 80% of the friction in joints 4-6. It can be seen that the tracking ability of the manipulator is degraded from the zero friction case, and some overshoots occur as the direction of the trajectory turns. However, the movement of the manipulator remains faithful to the shape of the desired trajectory, suggesting that the user will be able to make fine movements in contact with the environment, even in the presence of some uncompensated friction in the joints of the manipulator. Additionally, the ability of the manipulator to cover an area within 2.5cm of the initial point is maintained, as seen in Figure 33.

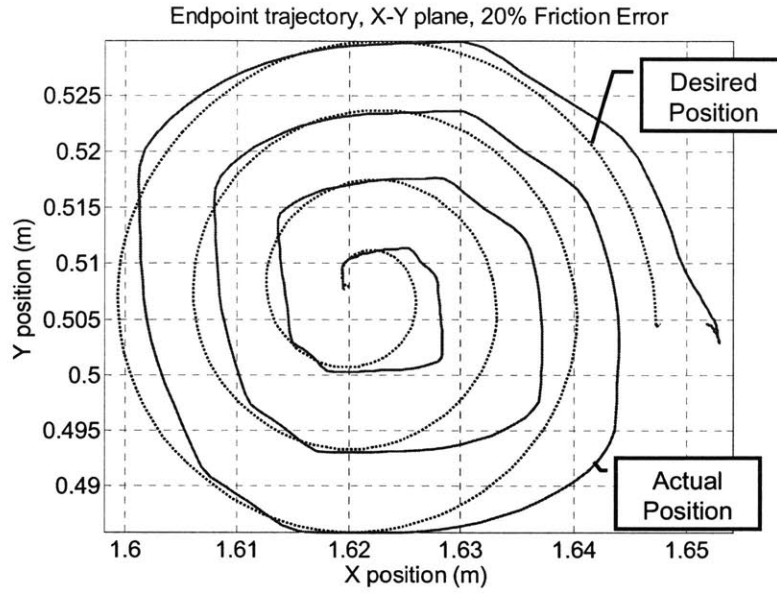


**Figure 32: Desired and actual endpoint trajectories in a manipulator with 20% uncompensated friction in joints 4, 5, and 6 during the contact spiral test**

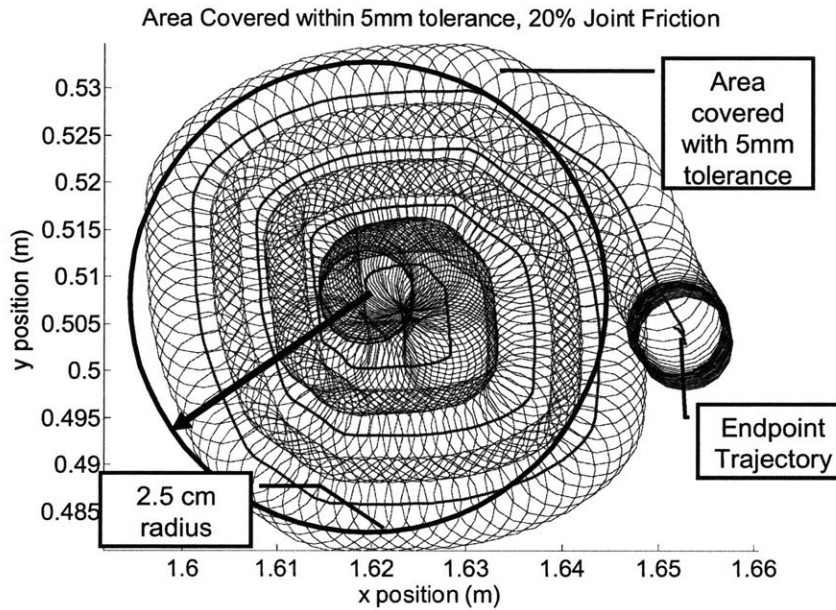


**Figure 33: Area covered with a 5mm tolerance by a manipulator with 20% uncompensated friction in joints 4, 5, and 6 during the contact spiral test**

The simulations in this section show that the insertion control mode gives the user an intuitive tool which moves in the desired direction, even in the presence of joint friction and contact forces. Uncompensated joint friction in the manipulator can lead to some tracking errors and slight overshoots while the manipulator is in contact with the

environment, but the overall trajectory remains faithful to the expected. The insertion controller allows the user to cover a sufficiently large area in a blind search pattern to find the insertion geometry. In the actual manipulator, a user would be able to use tactile clues and some visual feedback to close the loop, and search for the insertion point in a more educated way. The next two sections discuss the actual insertion tasks, and the ability of the insertion controller to utilize contact forces to aid a user in inserting the payload.

### **3.3.3: Aligned Insertion Simulation**

The first insertion task considered is the aligned insertion simulation. This simulation uses the simulated 2-lug light payload and insertion geometry, as described in section 3.1. The insertion geometry is a slot running down the length of a simulated wing. In this simulation, a payload which is rotationally aligned with the insertion slot is pushed horizontally across the wing until the lugs of the payload come into contact with the insertion slot, and enter the slot. Once the payload lugs are inside the insertion slot, the ability of the control algorithm to slide the payload along the slot in response to a user force at an offset angle to the desired direction of motion is demonstrated. This simulation demonstrates the ability of the insertion control algorithm to insert a payload aligned with the axis of the insertion geometry when the exact location of this geometry is unknown.

Figure 34 shows a side view of the manipulator and a close up of the insertion geometry during the aligned insertion simulation. Figure 34A shows the manipulator at time zero, several centimeters below and to the side of the insertion slot. At 3 seconds, a 100N upward force is applied by the user. This force is maintained throughout the insertion task. During the upward motion of the manipulator, the uncompensated joint friction in joint 4 causes the payload to slightly rotate about its pitch axis. At about 4.5 seconds, the forward lug of the payload impacts the wing (Figure 34B). This results in a contact torque fed back to the controller which causes the payload to level against the wing by 6 seconds (Figure 34C). At 7 seconds, a horizontal user force of 100N is applied along the negative payload X axis payload towards the slot. At about 11 seconds (Figure 34D), the lugs of the payload enter the slot in unison. At this point in time, the

manipulator is pushing up on the wing as a result of the error between the desired and actual endpoints of the manipulator, as seen in Figure 35. This upward force is sufficient to cause the payload lugs to enter the slot. The lugs contact the opposite side of the slot. The resulting horizontal force is enough to counteract the horizontal user input force, and because the only remaining force on the manipulator is the upward user force, the payload lugs move upward into the slot (Figure 34E). At 14 seconds, a horizontal user force of 70.7 N is applied to the manipulator at an angle of  $45^\circ$  to the direction of the slot. Despite this misaligned user force, the manipulator slides the payload down the slot (Figure 34F). Further analysis of the movement of the manipulator in the slot is seen in Figure 38.

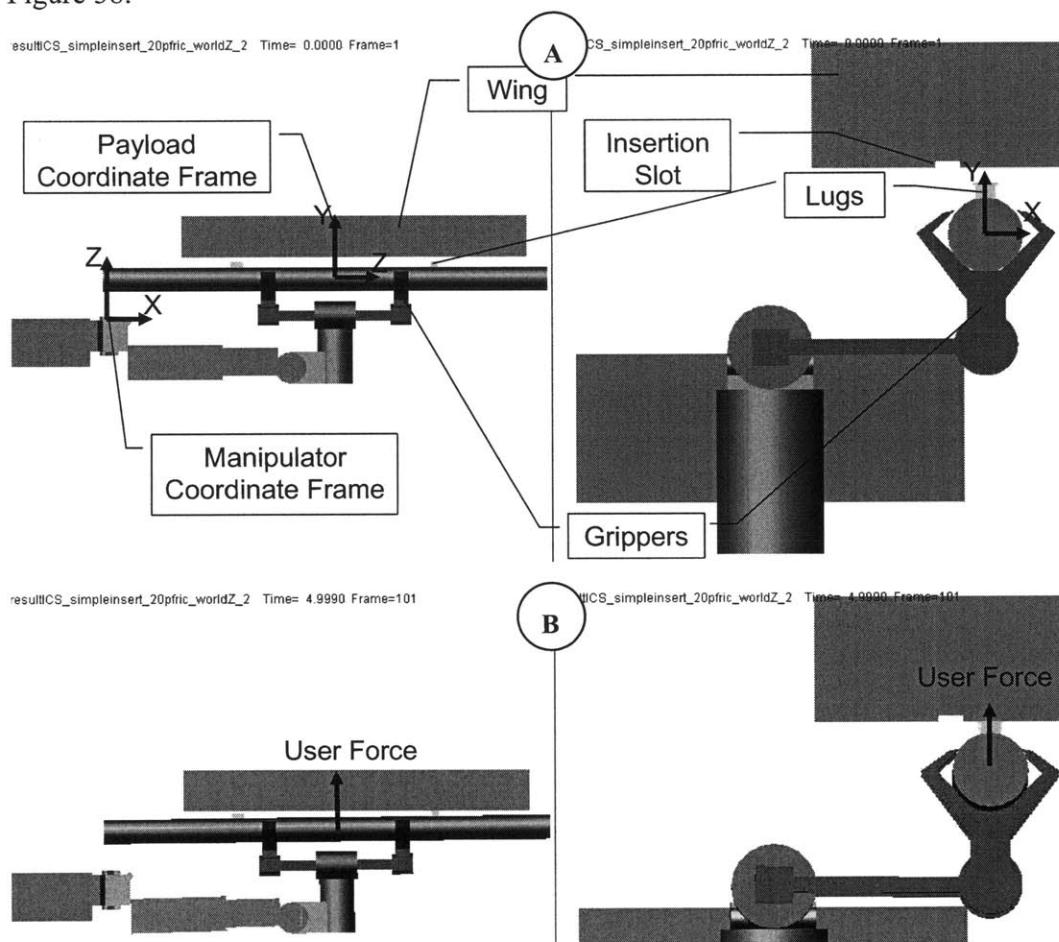


Figure 34 A-B: Aligned insertion task

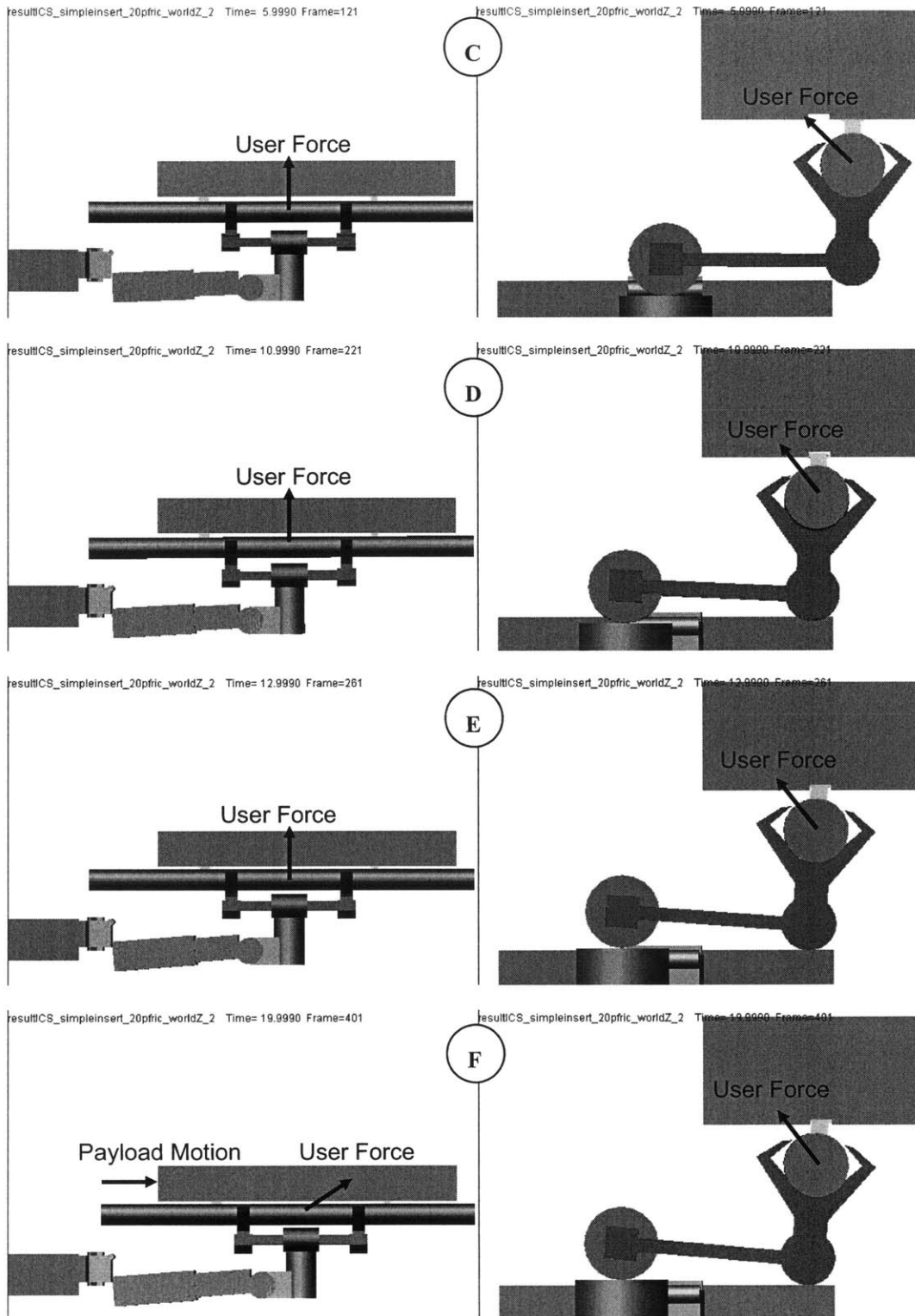
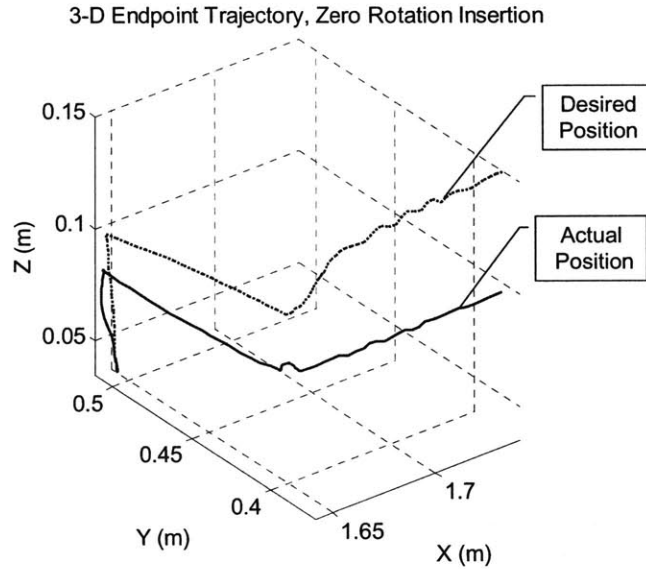


Figure 34 C-F: Aligned insertion task

Figure 35 shows a 3-D trajectory plot of the desired and actual positions of the manipulator during this zero rotation insertion task. The manipulator is seen to follow the desired trajectory closely, with the exception of the desired vertical position of the manipulator lying within the wing. The lengths of the initial rising motion, horizontal translation of the payload to the insertion slot, and the straight motion of the payload along the slot are clear from this plot.



**Figure 35: 3-D trajectory trace of the desired and actual endpoint positions of the manipulator during the aligned insertion task. The locations are in the manipulator coordinate frame.**

Figure 36 shows the input and user forces along the X axis of the payload. The friction from the payload movement along the wing is seen from 7-11 seconds. At 11 seconds, the lug impact with the wall of the slot is apparent, and from 11-14 seconds the contact force is rising to a value near 500 N (input force times user gain) when at 14 seconds the input force in the plane of the wing direction is shifted from perpendicular to the slot to an angle of  $45^\circ$  with respect to the slot. As the payload is pushed along the slot, the stick-slip friction causes noise in the contact force, but the force averages approximately 250N, which offsets the 50N component of user input force perpendicular to the slot. Figure 37 shows the contact and input forces along the Z axis of the payload. The contact force from 14-20 seconds, when the manipulator is pushed down the slot, is insufficient to



offset the input force. This results in the desired position of the manipulator endpoint moving down the insertion slot.

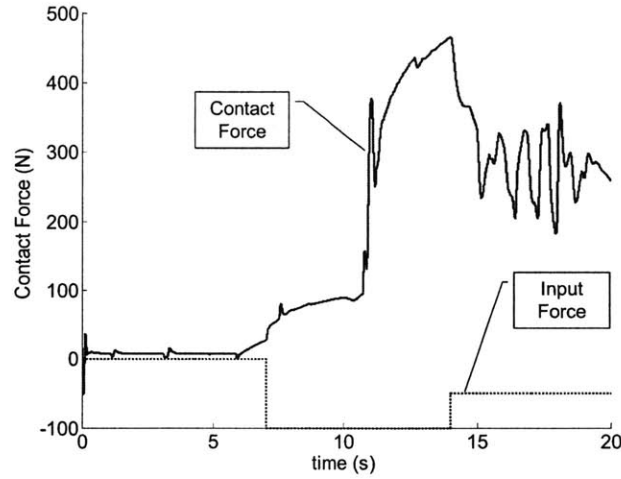


**Figure 36: Input and contact forces along the X axis of the payload during the aligned insertion test**

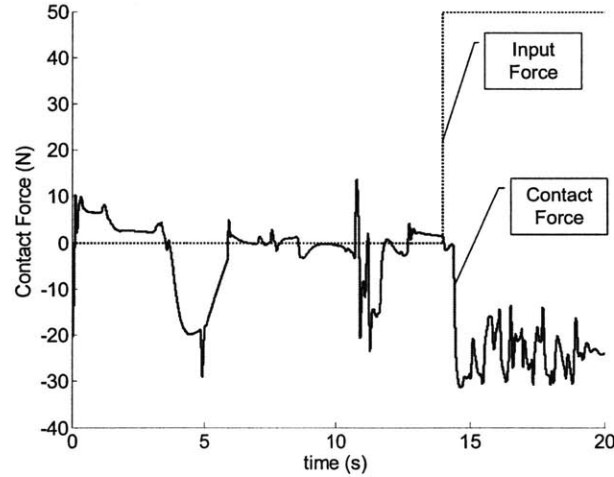


**Figure 37: Input and contact forces along the Z axis of the payload during the aligned insertion test**

A more detailed plot of the motion of the manipulator motion in the slot is seen in Figure 38. This plot shows a top view of the desired and actual manipulator trajectories, as well as contact and insertion force vectors sampled at a rate of 1Hz. The contact force vectors are scaled to 1/5 of their actual length to accurately represent their effect on the desired velocity of the manipulator when compared to the input force vectors. This plot clearly shows how the contact forces counteract the component of the input force perpendicular to the slot, while using the unopposed component of the input force to push the desired position of the manipulator along the slot. The small component of the

contact force in the endpoint X direction comes from friction between the lugs of the payload and the slot.

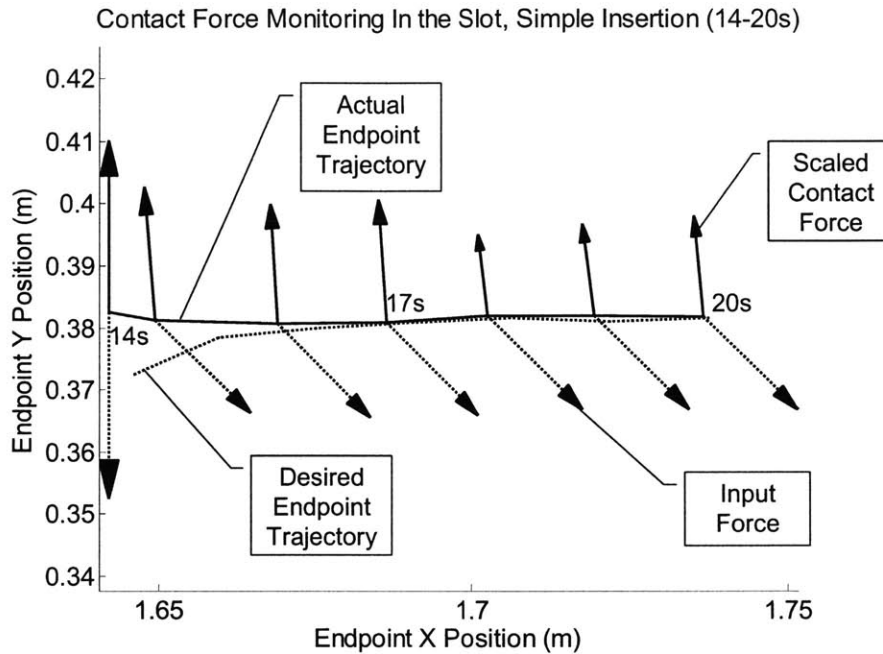


**Figure 38: Top view, plot of the actual and desired endpoint trajectory and sampled contact and contact forces of the manipulator as it slides in the slot from 14 sec – 16 sec**

The aligned insertion simulation described in this section demonstrates the ability of the insertion controller to use payload interaction with the environment and the resulting contact forces and torques to insert the payload and move it along a slot without jamming. These abilities are desirable and necessary to allow the user of the manipulator to safely and easily insert large payloads with the manipulator. As a final note, in Figure 34D-F, it can be seen that the payload and end of the robot rotate slightly about the Z axis of the payload. This is a result of the contact force pushing the endpoint of the robot downward. The error is small enough that it does not detract from the results of this test, and the test in the following section. In actual practice, this error would be easily corrected by rotational input from the user. However, this error is impossible to correct with open-loop inputs.

### 3.3.4: Misaligned Insertion Simulation

The simulation in the previous section showed the insertion controller using the contact forces from the insertion geometry to aid the manipulator in inserting its payload. The simulation in this section is similar, except that the payload does not begin the simulation aligned with the insertion slot. Throughout this section, references will be made to yaw, pitch, and roll. These correspond to rotations about the Y, X, and Z axes of the manipulator, respectively.

Figure 39 shows the progression of events during the misaligned insertion simulation. The manipulator begins the task several centimeters below and to the side of the insertion slot. Additionally, the payload is misaligned  $3^\circ$  in both pitch and yaw to the slot (Figure 39A). At 2 seconds, the payload is pushed upwards with a 100N force. At about 4 seconds, the rear lug of the manipulator comes into contact with the wing (Figure 39B).

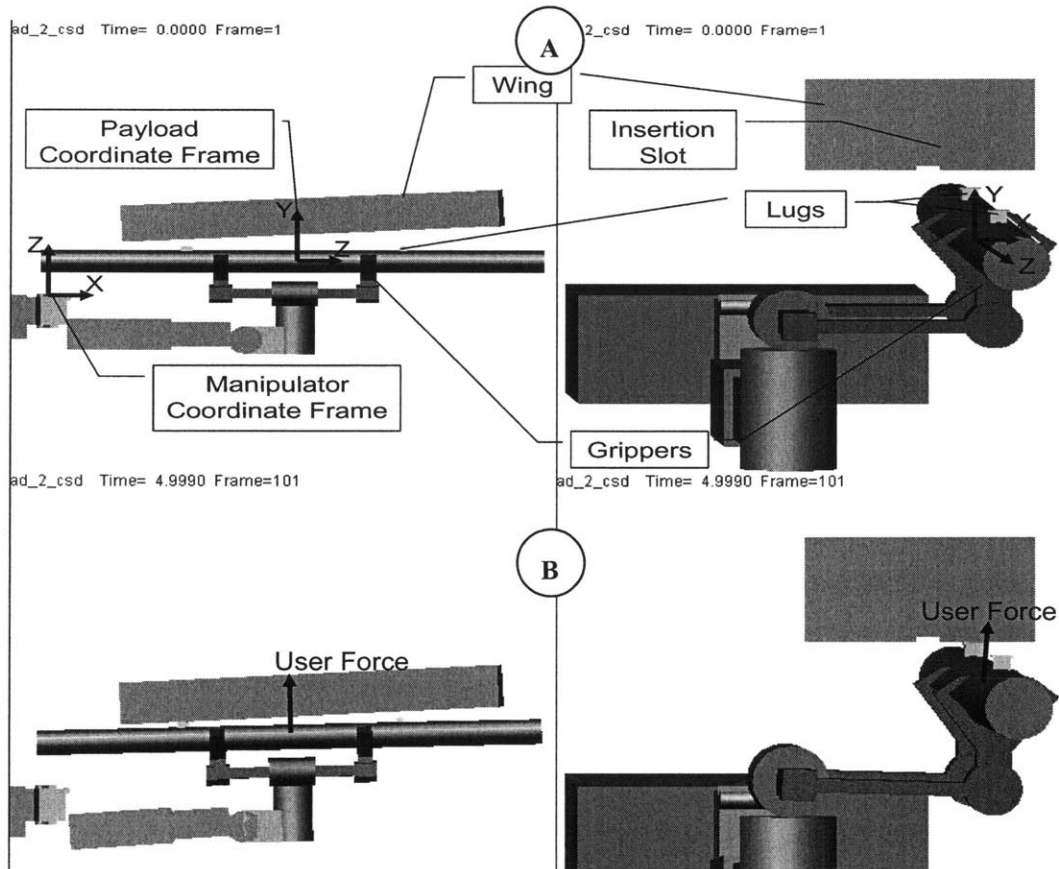
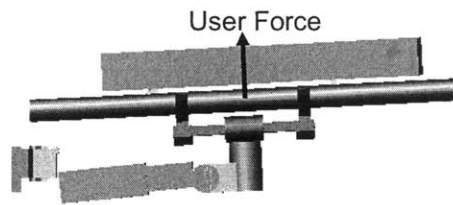
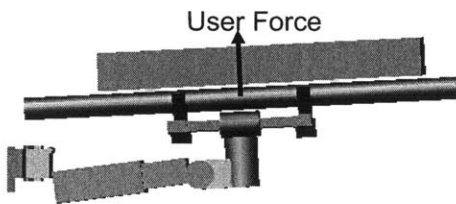


Figure 39 A-B: Complex insertion task with both yaw and pitch errors

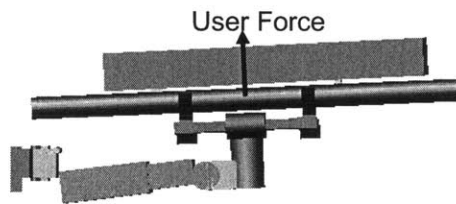
id\_2\_csd Time= 7.9990 Frame=161



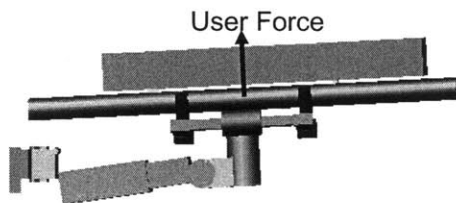
d\_2\_csd Time= 11.9990 Frame=241



ad\_2\_csd Time= 10.9990 Frame=221

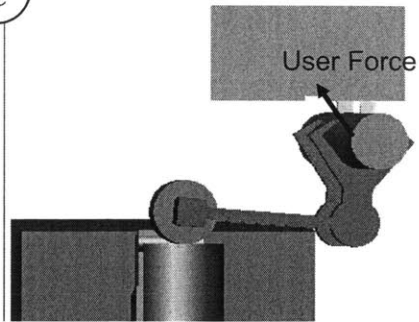


ad\_2\_csd Time= 13.9990 Frame=281

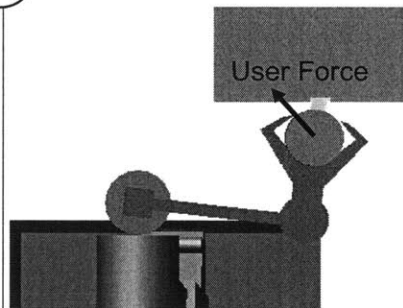


id\_2\_csd Time= 7.9990 Frame=161

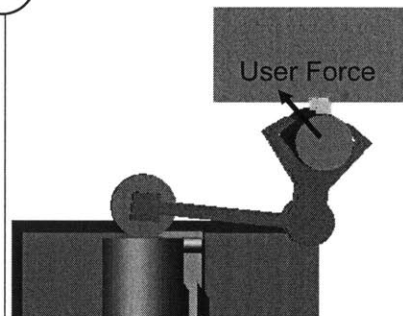
C



D



E



F

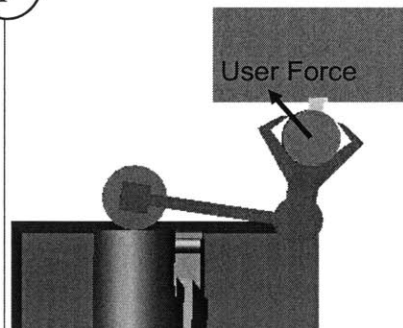
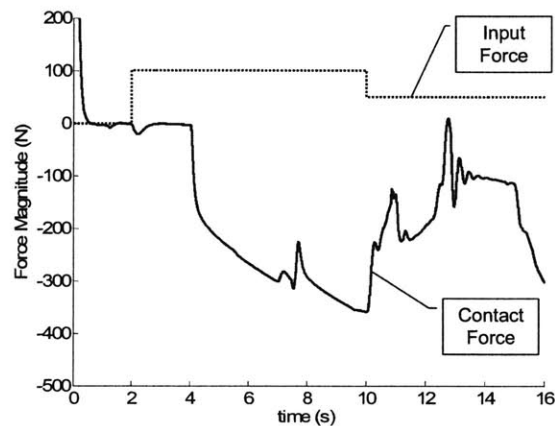
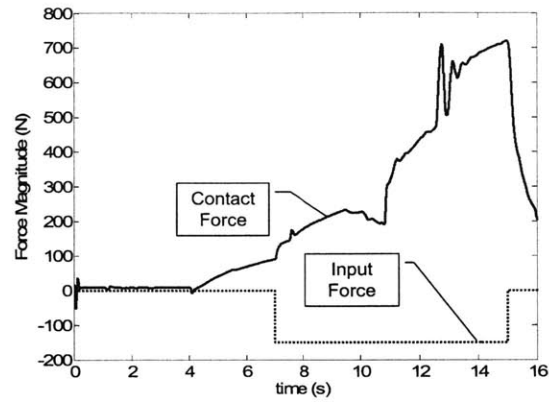


Figure 39 D-F: Misaligned insertion task with both yaw and pitch errors

This contact results in both a downward contact force, as seen in Figure 40, and a negative contact torque about the pitch axis, as seen in Figure 42. These forces and torques cause the manipulator to slow and rotate about its pitch axis until both lugs are in contact with the wing at 8 seconds (Figure 39C). As the payload is rotating in this direction, a horizontal user force of 150N is applied in the negative payload X direction at 7 seconds. This force results in manipulator movement towards the slot. At 11 seconds, the corner of the rear lug of the manipulator comes into contact with the insertion slot (Figure 39D). This contact causes a contact force opposing the user force in the payload X direction, as seen in Figure 41, and a negative torque about the yaw axis of the payload as seen in Figure 43. The user force on the manipulator and the reaction force from the slot result in a contact yaw torque, which rotate the payload of the manipulator towards the insertion slot (Figure 39E). At 14 seconds (Figure 39F), the front lug of the manipulator enters the insertion slot, and the rear lug of the manipulator fully engages in the slot. The upward force of the manipulator pushes both lugs into their slots, resulting in a successful insertion of the payload. The entire insertion task takes 14 seconds, within the 15 second goal.



**Figure 40: Contact and input forces in the payload Y axis during the misaligned insertion task**



**Figure 41: Contact and input forces in the payload X axis during the misaligned insertion task**

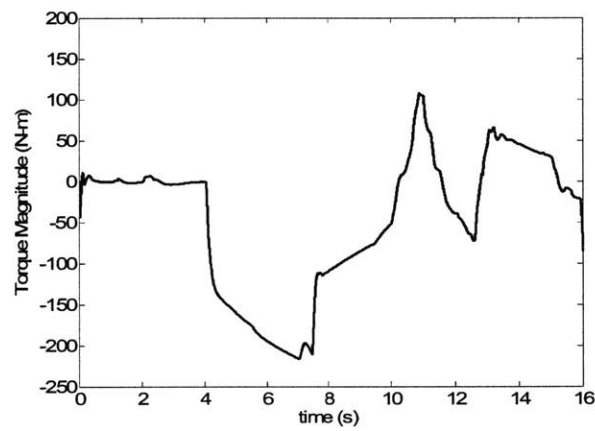


**Figure 42: Contact torque about the pitch axis of the payload during the misaligned insertion task**

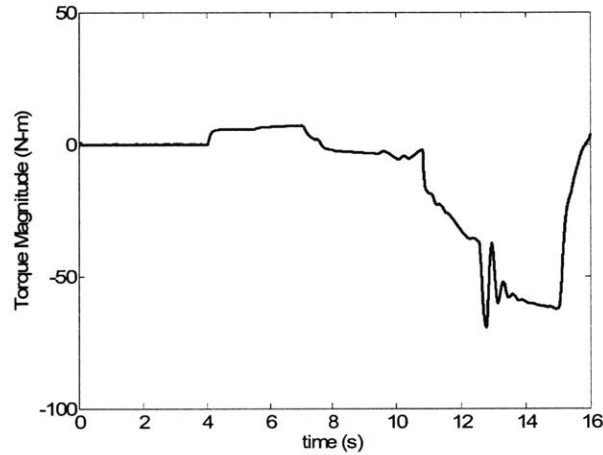


**Figure 43: Contact torque about the yaw axis of the payload during the misaligned insertion task**

This test demonstrates the compliance of the manipulator to the effects of contact forces. When the manipulator is pushed into a misaligned wall, the manipulator uses the

contact forces to align the payload with the wall. Similarly, as the payload is pushed across the wing and a single lug partially enters the hole, the torque resulting from this partial engagement is used to align the other lug with the insertion slot. This compliance to environmental forces and torques is extremely helpful to a user, and should give him or her a "feel" for the environmental effects on the manipulator. The successful insertion task with a misaligned payload and simple open-loop force inputs suggests that a human user should be able to use the insertion controller to exploit environmental forces to aid in payload insertion tasks.

### **3.4 Summary**

The simulation results presented in this chapter suggest that the manipulator will enable a user to maneuver and successfully insert the light payload. The position control tests demonstrate adequate performance when joint friction compensation is used. In the joints using adaptive friction compensation, the output from the joint estimators is able to calculate a feed-forward model of friction which should be able to compensate for at least 80% of the friction in those joints. The insertion control algorithm was shown to enable stable contact, and to allow a user to make fine motions in contact with the environment. Finally, two sample insertion tasks were performed that showed the ability of the insertion control algorithm to both insert a misaligned payload, and move the payload down a slot, when only imprecise simple open loop force commands are input to the system. Unfortunately, due to hardware construction difficulties, these simulation results will not be able to be compared against results from the actual full-scale manipulator. In the following chapter, the position and insertion control algorithms are implemented and evaluated on a reduced scale laboratory manipulator in order to examine the controller performance on a hardware system.

## CHAPTER 4: LABORATORY TESTS

---

Unfortunately, the full-scale manipulator hardware was not fully assembled and available in time to implement the control algorithms developed in chapter 2. Some aspects of the controller, particularly involving the user interface for the insertion control mode, cannot be properly tested without a human in the loop. Other aspects, like the ability of the adaptive estimators to extract parameters of a friction model for feed-forward compensation during insertion control mode, are better tested with hardware than by dynamic simulation. Therefore, the control algorithms developed in this thesis are applied to a small laboratory manipulator (Figure 44) in order to provide some experimental validation of the control algorithms.

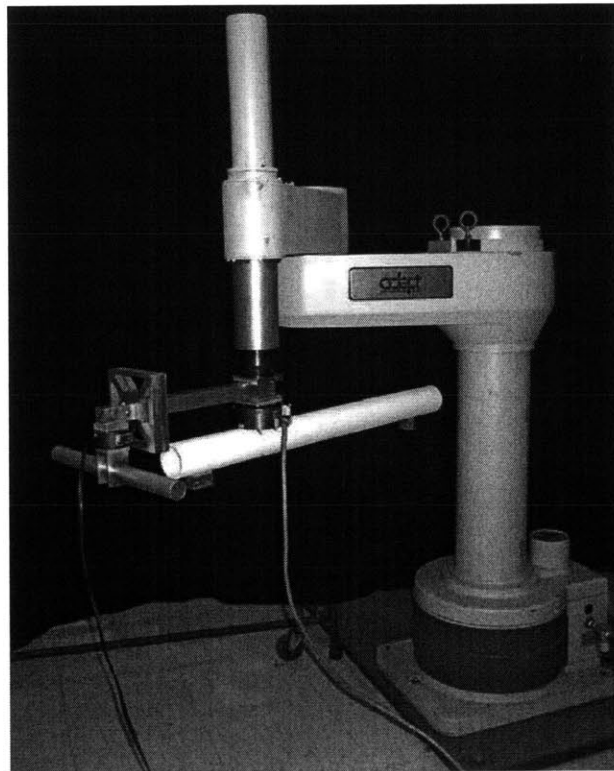


Figure 44: The AdeptOne manipulator experimental setup



The laboratory system which will be used is an AdeptOne robot. It is a four degree-of-freedom SCARA configuration manipulator. This configuration is significantly different from the full scale heavy lift manipulator system tested in simulation, and the payload capabilities of the Adept are significantly smaller than those of the full-scale manipulator. However, these differences show the validity of the control architecture outlined in Chapter 2 when tuned and applied to other systems.

## **4.1 Experimental Setup**

The Adept robot, as seen in Figure 45, is a 4 degree of freedom manipulator, which allows the end effector and payload to be translated in three axes, and rotated about the world yaw axis. It is rigidly mounted to the ground. Joint 1 (the shoulder joint) is a rotational joint about the base of the manipulator. Joint 2 (the elbow joint) is a rotational joint in the same plane as joint 1, and together these first two joints form a classical 2 degree of freedom planar manipulator. Joint 3 is a prismatic joint allowing vertical translation of the payload. Joint 4 is a screw joint which simultaneously rotates the payload about the yaw axis and vertically translates the payload. The motors for the first two joints are direct-drive motors with a belt transmission. The motor for joint 3 is a belt-driven gear motor, and joint 4 is actuated by a direct drive motor along its axis of rotation. A kinematic singularity occurs in this configuration when joint 2 is extended straight out, and during Cartesian motions, a software block does not allow joint 2 to approach the extended position. Mass and inertia properties for the Adept robot were calculated by observing the manipulator response to a series of open-loop torque inputs. Details of these tests can be found in Appendix B.

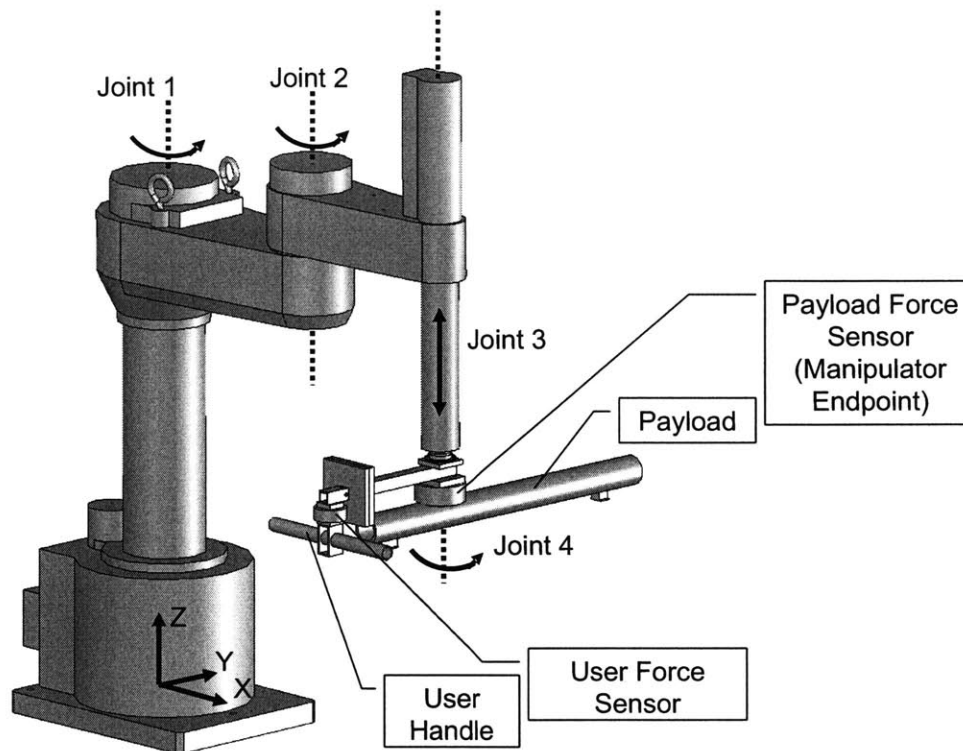


**Figure 45: The Adept robot with labeled joints, coordinate frame, and sensors**

The robot is equipped with two six axis force/torque sensors that allow sensing of user input and contact forces. The user input sensor is located under a handle which rotates with joint 4. To reduce potential danger to users and the force sensor, a breakaway mechanism is incorporated on the user force sensor handle which enables it to break away when the force on the handle approaches a dangerous level. The payload force sensor is located along the axis of joint 4, below the attachment point of the user force handle. This arrangement ensures that the sensing of the input and contact forces are decoupled. The payload is mounted underneath the payload force sensor. The robot is equipped with encoders on each joint to read joint positions. The robot is not equipped with any joint-level load cells for sensor-based friction compensation.

The control software for the Adept is implemented in C/C++ language on a 160 MHz Pentium I PC running Windows 95. It uses the Windows multimedia library for timing, and runs at a control frequency and sensor sampling rate of 200 Hz. The interface between the Adept and the control is a custom ISA bus card, and desired joint torque signals from the control software are translated into currents to the motors through an

external amplifier. The user and payload force sensors are identical six axis JR3 model 67M25A-U562 with a maximum load of 50 lbs. and 65 in-lbs. The force sensors are connected to the control computer through separate dedicated ISA interface cards.

The user interface allows the user to input desired joint position commands from the keyboard, as well as remove the user force handle from the Adept to use as a joystick for either joint-level or Cartesian trajectories. Open-loop position and force trajectories may also be input from the interface in both joint and Cartesian space. In insertion control mode, the user grasps the handle and pushes or pulls the payload in the desired direction of movement.

## **4.2 Controller Details and Modifications**

The Adept control architecture has maintained the basic architecture used for the end three joints of the heavy lift manipulator, with several modifications.

### **4.2.1 Endpoint Selection**

Cartesian endpoint control is achieved by inverse Jacobian resolved-rate control, as in the full-scale manipulator. The center of the contact force/torque sensor is used as the endpoint of the robot for calculation of the manipulator Jacobian and forward kinematics. As stated in section 2.3.1, this is a convenient place to choose as the endpoint, as it means that the force feedback from the contact force sensor may be used in a control law without converting the forces to another reference frame. The user input force at the force handle is transformed in the admittance law so that the forces and torques move the endpoint in an intuitive manner.

### **4.2.2 Scaling and Joint Controller Modifications**

The joint position controllers are tuned to a 1 Hz bandwidth, which is approximately the bandwidth of the joint controllers on the full scale manipulator with the light payload. The individual joint controllers are PD with added plant damping instead of PID and added plant damping. The admittance law for the force-feedback is also tuned to this 1 Hz bandwidth. See Appendices A and B for details on the tuning of

the joint controllers and admittance law. Constant gravity compensation torques are applied to joints 3 and 4 to offset the effects of gravity on these joints.

Matching the bandwidth of the controllers makes both systems respond to desired inputs in a similar manner. However, it results in the Adept, which is a much less massive manipulator, being far more susceptible to external disturbance forces, including the disturbance from the user pushing on the force handle and the disturbance from the environmental contact. To avoid as many disturbances as possible from the user pushing on the manipulator, open loop force tests are performed without the user touching the manipulator. This attempts to simulate the full scale manipulator, where the disturbance torque from the user would be negligible compared to the joint torques.

#### 4.2.3 Modifications to the Friedland-Park Algorithm

In several of the joints of the Adept, the stick-slip behavior of friction, coupled with the low bandwidth of the controllers, requires a significant joint error to move the joints. The Friedland-Park friction compensation algorithm applies the estimate of the friction magnitude multiplied by the sign of the joint velocity to calculate the friction compensation torque (4.1).

$$\tau_{fc} = \hat{a} \operatorname{sgn}(\dot{q}) \quad (4.1)$$

This algorithm is referred to as the “standard adaptive friction compensation algorithm”. This results in compensation of the friction when the velocity of the joint is not zero. However, during stick-slip behavior, the velocity of the joint is zero, and no friction compensation torque is applied until the joint begins to move. This results in some undesirable behaviors, which will be shown in the next section. A simple change to the friction compensation algorithm is to replace the friction compensation law to (4.2).

$$\tau_{fc} = \hat{a} \operatorname{sgn}(s) \quad (4.2)$$

where  $s$  is a “composite variable” of form (4.3):

$$s = \dot{q} + \lambda(q_d - q) \quad (4.3)$$

This algorithm is referred to as the “composite variable adaptive friction compensation algorithm”. If  $\lambda$  is chosen to be sufficiently small, and the adaptation law remains

unchanged, this control law results in behavior identical to the standard Friedland-Park compensator when the joint is moving. However, when the joint is at zero velocity, a friction compensation torque is still applied in the direction of the joint error. Ideally, this should result in smaller steady state errors and lessen the large jerk that occurs at the beginning of joint movement when the friction compensation torque is suddenly applied. In practice, however, this control law leads to chattering about the desired point at zero velocity. Therefore a small change is made to the control law by multiplying the estimate of the friction by a saturation function of  $s$ . A saturation function is defined as 1 at any point where the argument is greater than 1, -1 where the argument is less than -1, and equal to the argument in between -1 and 1. A plot of a saturation function is shown in Figure 46.

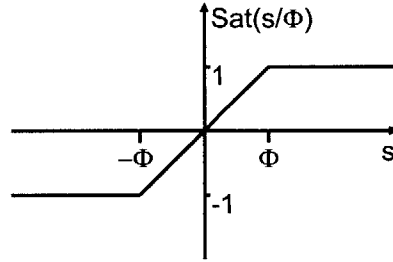


Figure 46: The saturation function  $\text{sat}(s/\Phi)$

The new control law is given by

$$\tau_{fc} = \hat{a} \text{sat}\left(\frac{s}{\Phi}\right) \quad (4.4)$$

where  $\Phi$  is the minimum magnitude of the sliding variable which results in application of the full friction compensation torque.  $\Phi$  is selected by choosing  $\Phi/\lambda$  to be the minimum joint error magnitude which will result in the application of the full friction compensation torque at zero velocity. Again, if  $\lambda$  is sufficiently small, this has negligible effect on the behavior of the friction compensation when the joint is moving. This “composite variable friction compensation algorithm” will be tested and its performance will be compared to the standard Friedland-Park algorithm.

#### 4.2.4 Payloads and Insertion Setup

Two payloads are used on the Adept robot. The first consists of a simple circular peg (See Figure 47). The second is a half-scale mockup of the light payload to be used on the heavy lift manipulator, and consists of a cylinder with two lugs (See Figure 48). Corresponding mating geometries were constructed for each payload: a chamfered hole for the single peg payload, and a slotted rail with two holes for the two lug payload. Detailed drawings of both payloads and the mating tolerances are shown in Appendix F. The mating tolerances for the single peg payload is approximately 0.3 mm, with a 3mm chamfer, which is similar to the tolerances on the rear lug of the payload of the full-scale manipulator.

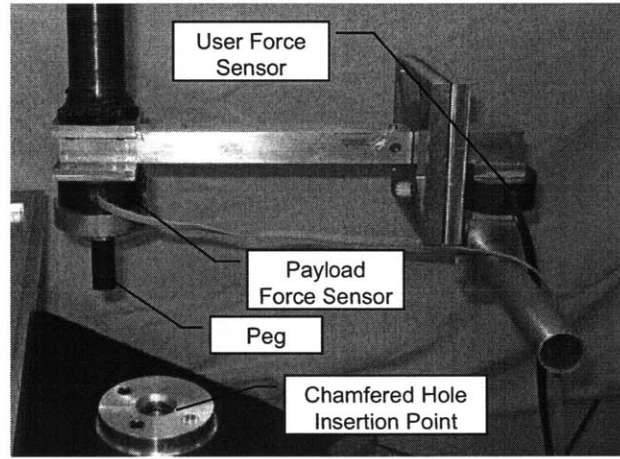


**Figure 47: The single peg payload and insertion geometry**

The tolerances for the two lug payload are shown in Table 5. The tightest mating tolerances for the two lug payload are in the payload X direction (using the coordinate systems shown in Figure 3 and Figure 48). The tolerance is 1.28 mm for each lug, with a 2mm chamfer on the rear insertion point. These tolerances are approximately half of the tolerances which occur in the insertion task for the full-scale manipulator.

**Table 5: Comparison of tolerances between the light payload on the full-scale manipulator and the 2-lug payload on the laboratory manipulator**

Payload	Front Lug X direction	Front Lug Z direction	Rear Lug X direction	Rear Lug Chamfer (X)	Rear Lug Z direction
Actual	3.61 mm	20.83 mm	4.74 mm	3.18 mm	123.19 mm
Laboratory	1.36 mm	10.64 mm	1.36 mm	2.0 mm	34.59 mm

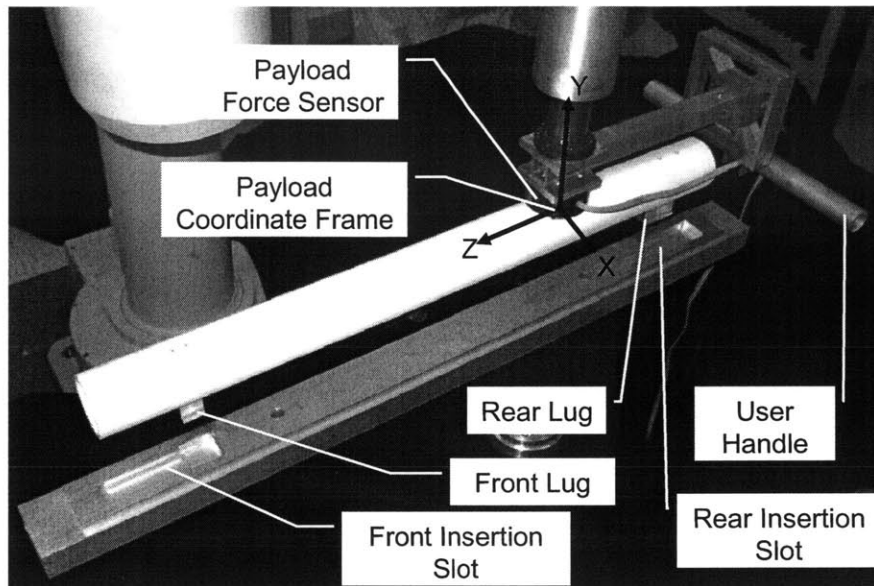


Figure 48: The two lug payload and insertion geometry

### 4.3 Position Control Tests

The position controller is vital to the proper function of the manipulator in both position control and insertion control mode. Several tests confirm that its behavior is as expected, and validate the standard and composite variable adaptive friction compensation algorithms. These tests consist of joint-level trajectory following tests and Cartesian-space trajectory following tests. Finally, the extracted feed-forward model of friction is evaluated. The two-lug payload is mounted on the manipulator during all position control tests.

#### 4.3.1 Joint-Level Tests

The joint controllers are tested by inputting a sinusoidal desired trajectory to each joint controller, and observing the ability of the joint to follow the trajectory without friction compensation, with the standard Friedland-Park compensation, and with the modified composite variable friction compensation. For a fair comparison, both compensation methods use the same gains  $k$  and  $\mu$  in the adaptive compensation law. The tuning process for these gains is detailed in Section 4.3.3.

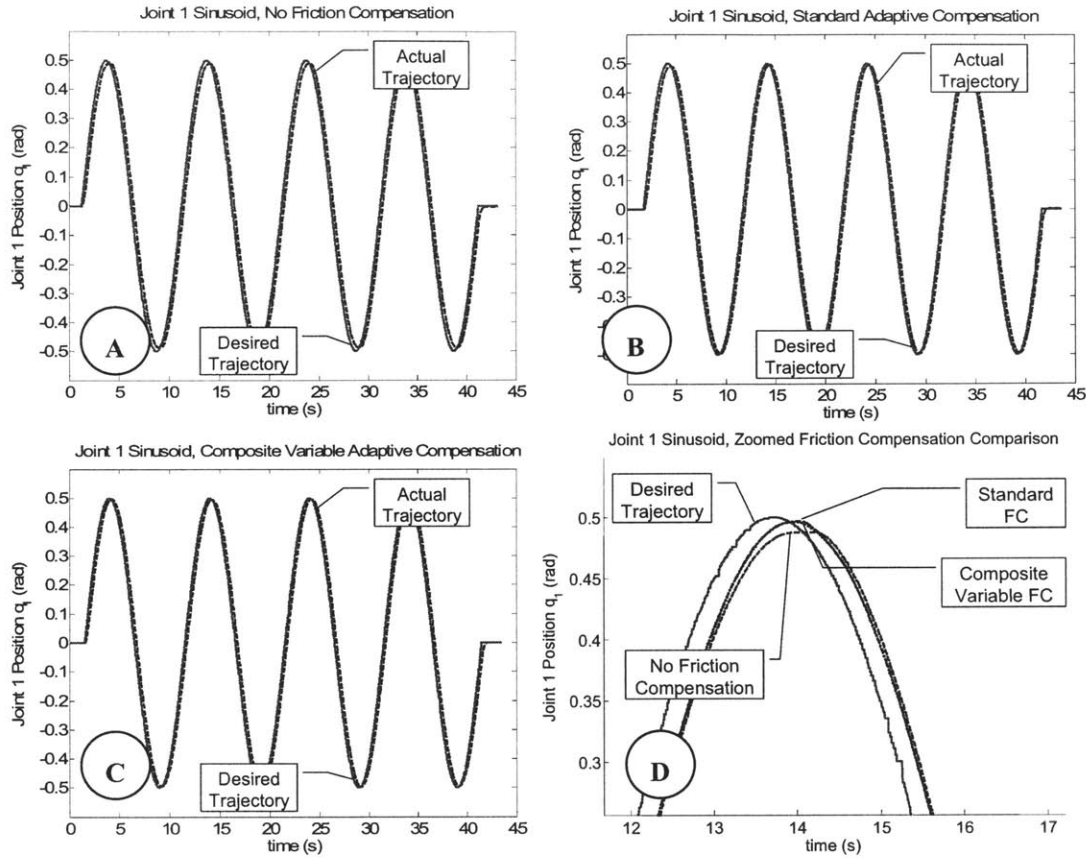


**Figure 49: Joint 1 Sinusoidal Trajectory Following Tests**

In joint 1 (the shoulder joint of the Adept), the position controller is sufficient to overcome most of the effects of friction without a separate compensation algorithm (Figure 49A). The gains are sufficiently high to overcome most of the effects of friction. The effects of both the standard and composite-variable friction compensation algorithms on the trajectory tracking are minimal (Figure 49B and C). Figure 49D shows a zoomed in picture that shows both friction compensation algorithms perform similarly, and very slightly improve the joint tracking response from the zero compensation case.



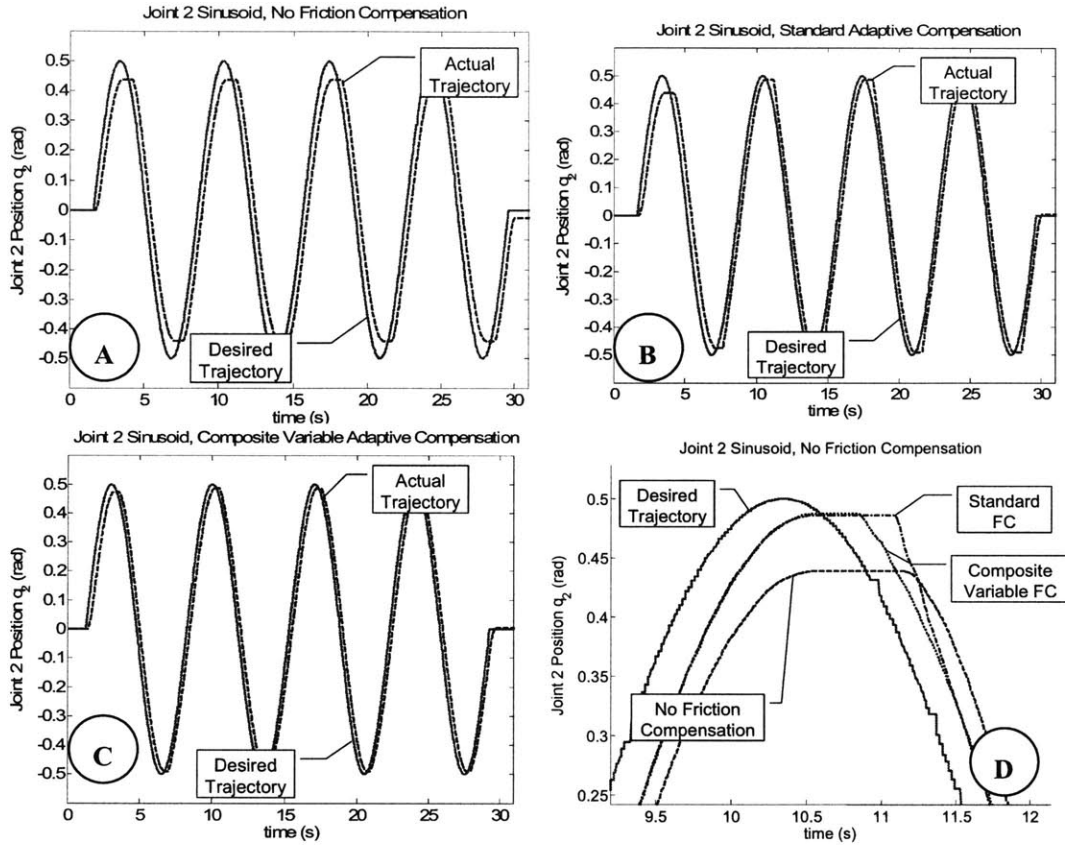


**Figure 50: Joint 2 Sinusoidal Trajectory Following Tests**

In joint 2 (the elbow joint of the Adept), friction has a much greater effect on the performance than in joint 1. It can be seen that without friction compensation (Figure 50A), the top of the waveform is cut off. When the standard Friedland-Park algorithm is used to compensate for friction (Figure 50B), the error at the top of the waveform is significantly reduced. However, when the joint is switching directions, a lag occurs until the joint begins to move. This effect is presumably because, as mentioned in Section 4.2.3, the estimate of the friction is multiplied by the sign of the velocity. The composite variable friction compensation algorithm (Figure 50C) eliminates this lag when the direction is switched. Figure 50D shows a more detailed look at the cutoff that occurs at the top of the waveform with no friction compensation, and the lag of the standard friction compensation algorithm. It also shows that both friction compensation algorithms serve to reduce the lag between the desired and actual joint position.

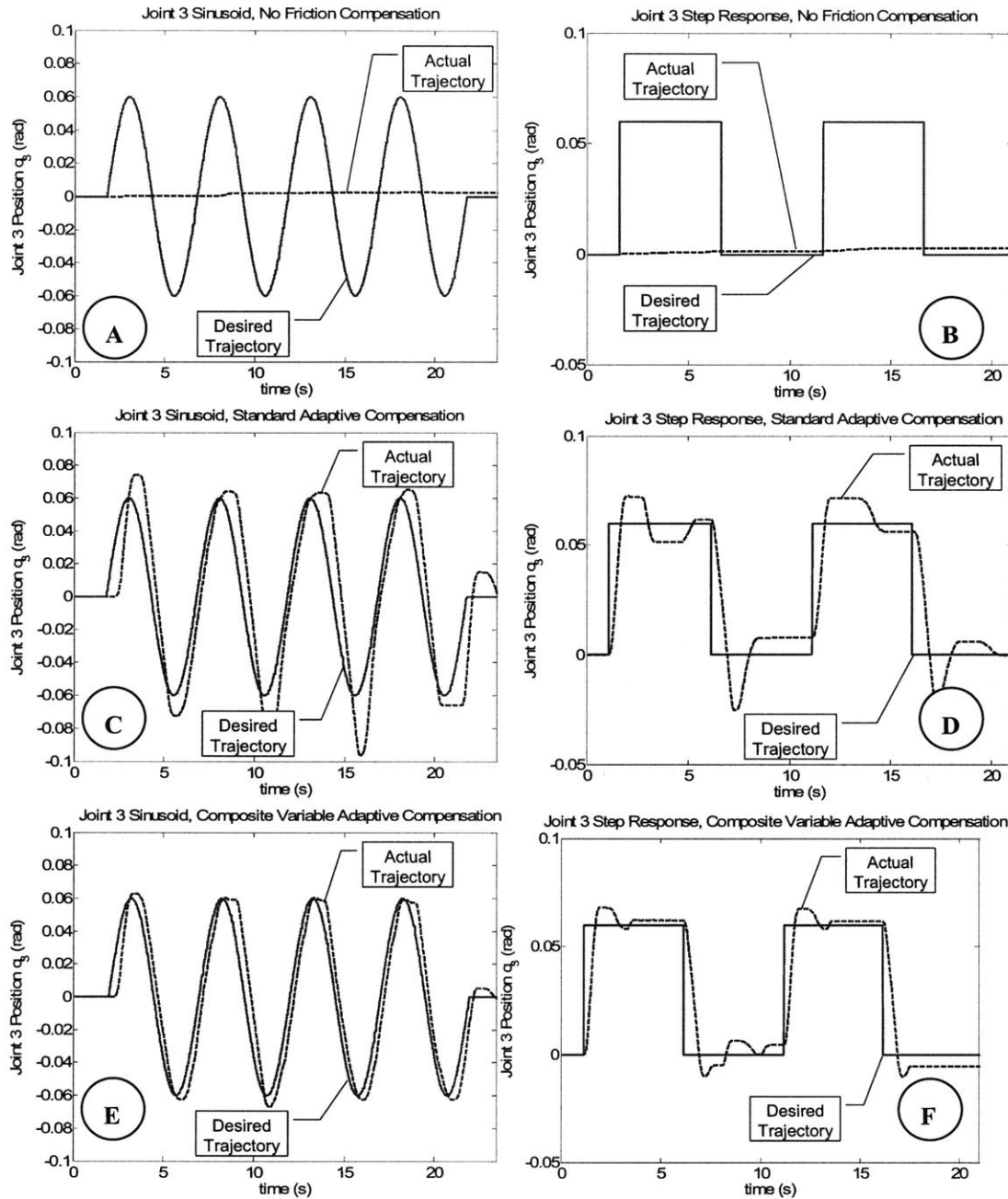


**Figure 51: Joint 3 sinusoidal and step response following tests**

In joint 3 (the prismatic joint allowing vertical translation of the payload) the effects of friction are significantly more pronounced than in the two previously examined joints. Examination of joint sinusoids and step functions without friction compensation (Figure 51A and B) show that a joint error of 6 cm is insufficient to break the joint free of the

static friction torque. The entire range of travel of joint 3 is 20 cm, so the joint errors caused by friction are quite significant. If the Adept manipulator were optimized for performance, the joint gains for this joint would be significantly raised, and the effects of friction would be reduced. However, the evaluation of this laboratory manipulator dictates that the bandwidth of the joint controllers be limited to 1 Hz, similar to the heavy lift manipulator. Because the force of friction in the joint is larger than the torque from the PD joint controller, the ability of the friction compensation torque to accurately track and compensate for friction is far more important than in the other joints.

When the standard friction compensation algorithm is employed during sinusoidal and step tests (Figure 51C and D), the tracking performance of the joint is greatly improved. However, large position overshoots occur during both tests. In Section 4.3.3, the friction profile in joint 3 will be shown to have both coulomb and viscous components. The viscous components are very pronounced, and these overshoots are possibly caused by a lag in the observer estimate of friction. Lags such as these can occur with a rapidly varying friction profile, and are one of the drawbacks of using an observer-based friction compensation method that works best for minimal-variance friction profiles.

Figure 51E and F show that the position overshoots are less pronounced when using the composite variable friction compensation algorithm. The improvement in the performance of this algorithm over the standard adaptive algorithm is particularly noticeable during the sinusoid trace.

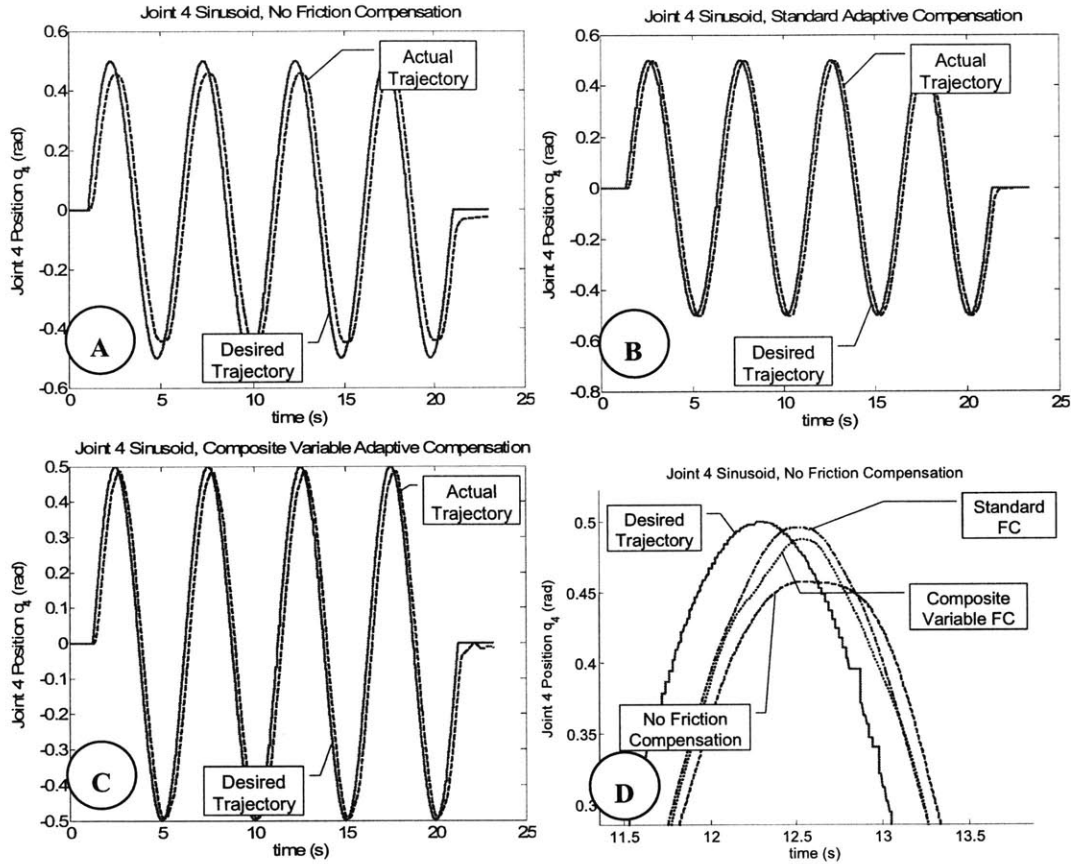


**Figure 52: Joint 4 Sinusoidal Trajectory Following Tests**

In joint 4, the joint allowing yaw rotation of the payload, the effects of friction are reasonably small, as seen in Figure 52A. The standard friction compensation algorithm (Figure 52B) shows a significant improvement in tracking ability, eliminating the cut-off of the top of the waveform and slightly reducing the error. The joint does not appear to stick when the direction of the joint changes is not observed, as it was in joint 2. The composite variable algorithm (Figure 52C) does not perform as well as the standard algorithm in this joint, and demonstrates undesirable chattering behavior when the joint comes to a stop. In Figure 52D, it can be seen that the composite variable algorithm results in slightly larger errors than the standard algorithm, but both show an improvement in tracking ability than the absence of any compensation.

### 4.3.2 Cartesian Trajectories

In addition to individual joint tests, the ability of the adaptive friction compensation algorithms to reduce tracking errors is tested during coordinated joint movement. The input to the system is a clockwise square velocity input in the horizontal (manipulator X-Y, as defined in Figure 45) plane. This trajectory requires coordinated motion from joints 1 and 2 of the manipulator. The performance metric used to evaluate the friction compensation algorithms in this experiment is the tracking error in the horizontal plane. The tracking error is measured perpendicular to the desired path of the manipulator. A summary of the tracking error results for this experiment is shown in Table 6.

Figure 53A shows a top view of the trajectory trace of the manipulator following this input with no friction compensation. As seen in Figure 53B, the maximum endpoint tracking error during this test is about 3 cm, and the mean tracking error during the trajectory is 0.79 cm. Figure 54 shows the results of the Cartesian tracking test with the standard friction compensation algorithm implemented on the manipulator. The peak tracking error is approximately the same as in the case with no friction compensation. However, the mean tracking error is significantly reduced, with a peak value of 0.28cm. As stated previously, the standard friction compensation algorithm does not apply the compensation torque until the manipulator begins to move, resulting in an initial lag. The peak tracking error occurs at the first corner of the trajectory (6-7s), and is likely the result of the desired trajectory changing direction before the controller has time to overcome the lag. Later in the trajectory, when the manipulator is moving, the tracking error is significantly lower than the case with no friction compensation. Figure 55 shows the results of the Cartesian trajectory tracking test using the composite variable algorithm. The tracking error is similar to that exhibited by the standard algorithm, except the error at the first corner is significantly smaller. This is likely because the composite variable algorithm applies a friction compensation torque before the manipulator begins to move, removing the initial lag seen in the standard adaptive algorithm. The maximum tracking error during this test is 1.5 cm, and the mean tracking error during the trajectory is 0.20 cm.

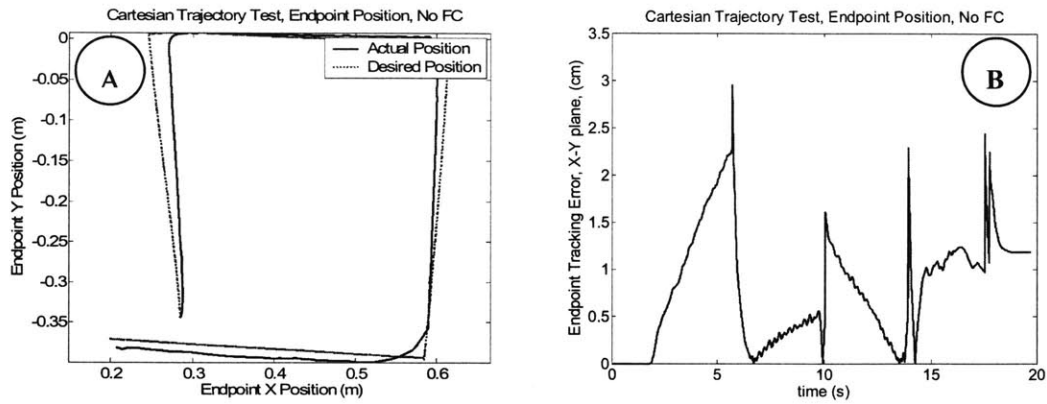


**Figure 53: Trajectory trace and tracking error plot of the Cartesian trajectory with no friction compensation**

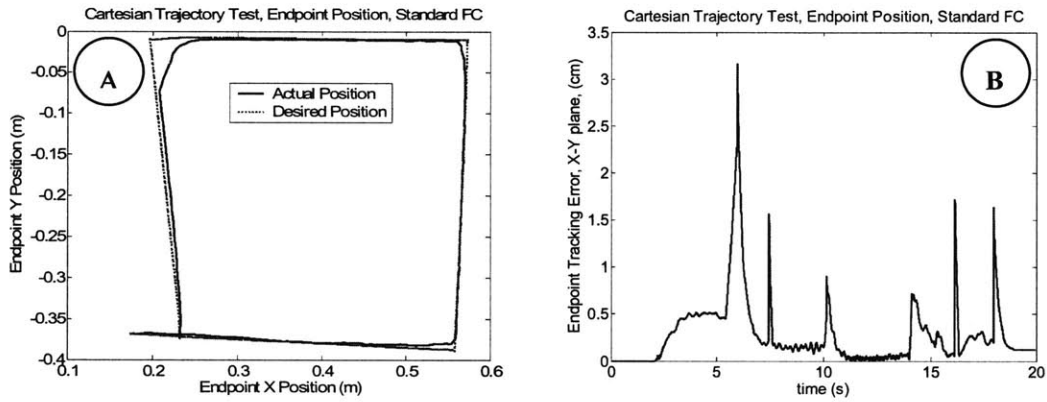


**Figure 54: Trajectory trace and tracking error plot of the Cartesian trajectory with standard adaptive friction compensation**

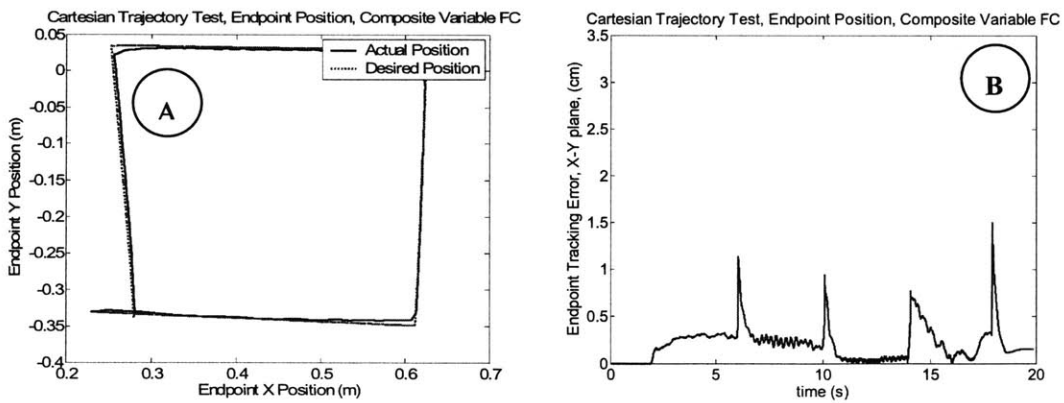


**Figure 55: Trajectory trace and tracking error plot of the Cartesian trajectory with composite variable friction compensation**

**Table 6: Tracking error comparison for the Cartesian trajectory tracking experiment**

Friction Compensation	Max. Tracking Error	Mean Tracking Error
No FC	2.96 cm	0.79 cm
Standard FC	3.16 cm	0.28 cm
Composite Variable	1.50 cm	0.20 cm

The results from the position control tests demonstrate the ability of the adaptive friction compensation algorithms to reduce tracking errors of the Adept robot. Therefore, during position control mode, the composite variable adaptive friction compensation algorithm will be implemented in the joints 1, 2, and 3, where it demonstrated superior performance to the standard adaptive algorithm. In joint 4, the standard friction compensation algorithm will be used.

#### **4.4 Friction Model Extraction**

The performance of the manipulator under position control was significantly improved by the addition of the adaptive friction compensators. Under insertion control, which will have disturbances from both user and contact forces, any friction compensation must be performed by a non-adaptive method. This method will be a model-based feed-forward friction compensation that uses prior estimates from the adaptive estimators to formulate a model of friction.

##### **4.4.1 Adaptive Law Tuning**

Generally, adaptive control laws work best to identify constant or slowly-varying uncertain parameters in a system. Unmodeled disturbances can lead to inaccurate identification of system parameters, but the stable nature of most adaptive controllers means that while the adaptation law is being updated, the adaptive parameters will change to maintain accurate tracking performance [52]. Even in the absence of significant unmodeled disturbances, excessively large adaptation gains can lead to oscillatory parameter estimates. Therefore, it is necessary to tune the adaptation law to not only provide an improvement in tracking during position control, but to provide a usable estimate of the friction for use in constructing a model for feed-forward friction compensation.

The Friedland-Park adaptive algorithm uses two parameters in its adaptation law (4.5),  $k$  and  $\mu$ .

$$\dot{z} = k\mu|\dot{q}|^{\mu-1}[\tau_{app} - \tau_{fc}] \text{sgn}(\dot{q}) \quad (4.5)$$

$k$  is a general adaptive gain that increases the rate of convergence of the algorithm.  $\mu$  is a modifier that makes the adaptation law less sensitive at lower velocities as it is raised. These parameters were tuned so that the estimate quickly converged to a steady-state value, but had minimal parameter oscillation at steady-state. Table 7 shows the final adaptive gains used on the Adept robot. Figure 56 is a plot of the absolute value of the friction estimate from joint 2 against joint velocity from the sinusoidal trajectory following test of Section 4.3.1. It demonstrates that the friction estimate converges to a symmetrical function of velocity after less than one full sinusoidal oscillation.

**Table 7: Adaptive algorithm parameters for the Adept Robot**

Joint	K	$\mu$
1	1	1.5
2	1	1.5
3	50	1.1
4	10	1.5

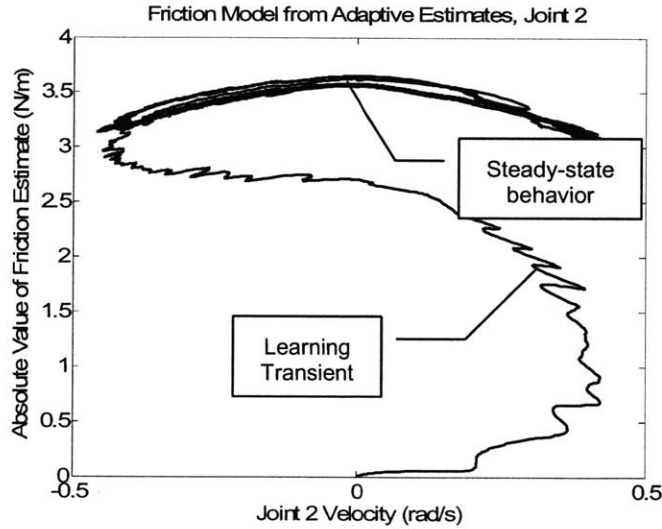


**Figure 56: Plot of the absolute value of the friction estimate vs. joint velocity for a sinusoidal movement of joint 2 of the Adept manipulator**



#### 4.4.2: Friction Model Identification

As mentioned in the previous section, the adaptive estimators work best for friction profiles which vary minimally over time, such as Coulomb friction. Joint 2, as previously shown, exhibits a symmetrical profile which varies slightly with velocity. Joints 1 and 3 demonstrated a model of friction dependent upon the sign of the joint velocity. These dependencies will be shown in section 4.3.4.1 and 4.3.4.3, respectively. In joint 3, this is likely due to a small error in the gravity compensation. In joint 1, the cause for this difference is unknown. The discontinuity in the friction model at zero velocity causes undesired behavior, due to the dynamics of the internal state of the estimator. A simple fix of this is to make two separate adaptive compensation laws, and switch between the two when the joint velocity changes sign.

##### 4.3.4.1: Joint 1

By using this discontinuous control law, and preventing joint 2 from sympathetically moving with joint 1 movements, the output from the adaptive estimator during a sinusoidal motion of joint 1 indicated an asymmetric Coulomb + viscous friction model (Figure 57).

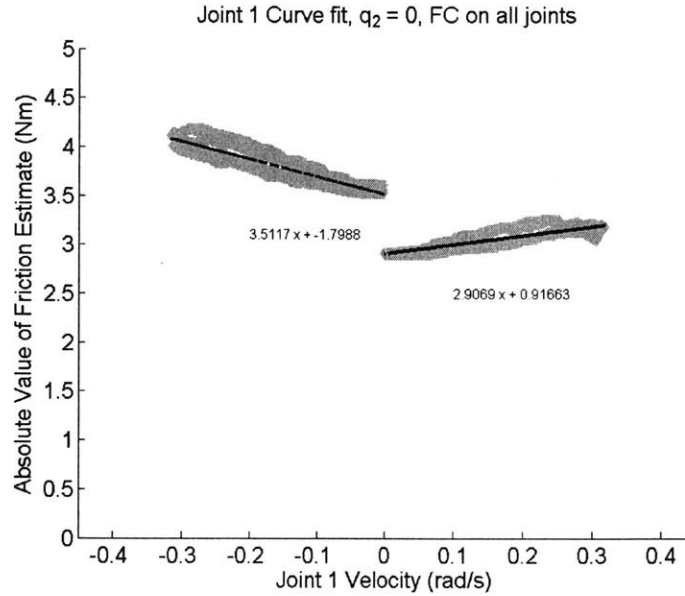


Figure 57: Plot of friction estimate against time for a sinusoidal trajectory of Joint 1 using the discontinuous composite variable control law, with friction compensation to other joints turned off

The friction was also found to vary with the angle of joint 2. Equation 4.6 represents a model with coulomb and viscous coefficients that vary with the angle of joint 2. The parameters of the friction model, as well as the maximum and mean modeling errors are shown in Table 8. The modeling error is defined as the percent error between the curve-fit model of friction and the friction estimate from the adaptive algorithm. Further details of the derivation of this model and the least-squares curve fit to identify the parameters are in Appendix C. To ensure friction is not overcompensated, the feed-forward compensation will be this estimate of friction multiplied by a gain of 0.9.

$$F_{fric1} = -\text{sgn}(\dot{q}_1) * (a_1 + a_2 \cos(q_2 - a_3) + \dot{q}_1(a_4 + a_5 \cos(q_2 - a_3))) \quad (4.6)$$

**Table 8: Coefficients of Equation (4.2) for joint 1 friction**

Direction	$a_1$	$a_2$	$a_3$	$a_4$	$a_5$	Mean % err	Max % err
Positive	3.18	.142	-2.1	.28	-.27	3.3%	10.1%
Negative	4.12	.42	-.74	-.77	-.62	2.6%	9.0%

Identifying the form of the friction for joint 1 was time-consuming. This effort may be unnecessary for actual implementation, as the results of Section 4.3.1 demonstrate that joint friction does not significantly affect the performance of joint 1, and a simple asymmetric coulomb model may suffice to compensate for most of the friction. However, a similar process to that described in Appendix C may need to be undertaken in the full-scale robot if the friction does not match the predicted form.

#### 4.3.4.2: Joint 2

Identification of a friction profile for joint 2 provides much less of a challenge than joint 1. Figure 58 shows the friction estimate from joint 2 as a function of joint velocity over its expected operating range during a sinusoidal motion. It appears to be a parabolic function with a peak value of 3.6 Nm at zero velocity. The magnitude of the friction estimate does not vary widely, so a simple Coulomb model can be used to approximate the friction. The adaptive estimator data was fit to this model, and the Coulomb friction parameter  $a_1$  was identified.

$$F_{fric_2} = -\text{sgn}(\dot{q}_1) * a_1 \quad (4.7)$$

$$a_1 = 3.34 Nm$$

The maximum error of this model for the data used in the curve fit was 10.2%. As in joint 1, the feed-forward friction compensation torque will be 90% of this modeled estimate.

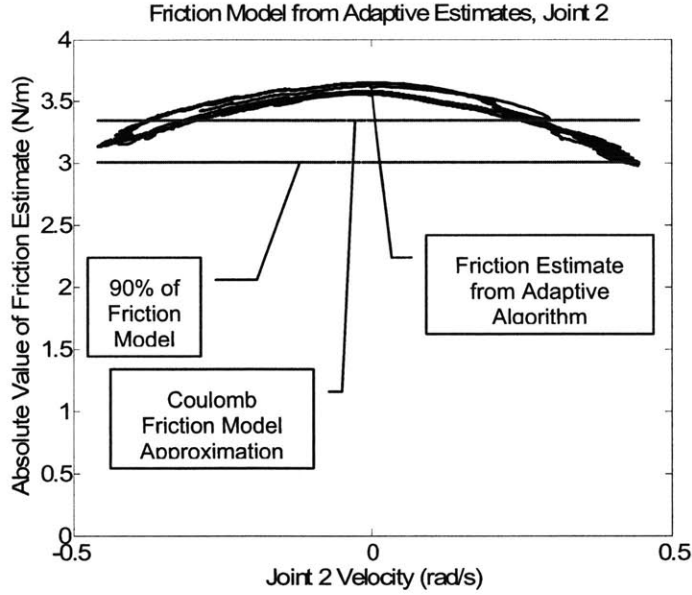


Figure 58: Friction model extraction for joint 2

#### 4.3.4.3: Joint 3

The friction in joint 3 can be modeled as an asymmetric Coulomb and viscous friction (Equation 4.8). The large friction in this joint compared to the control forces from the PD controllers results in a noisier estimate of friction than in the other joints. Figure 59 shows the friction estimate from the adaptive compensator as a function of joint velocity for both positive and negative joint velocities, as well as the curve-fit model of friction for the joint. The asymmetry in the models is likely caused by uncompensated gravitational effects. The coefficients of the curve fit are shown in Table 9. Because of the higher uncertainties in this model from the noisy data, the feed-forward friction compensation torque will be 80% of this modeled estimate.

$$F_{fric_3} = -\text{sgn}(\dot{q}_1) * (a_1 + a_2 * \dot{q}_3) \quad (4.8)$$

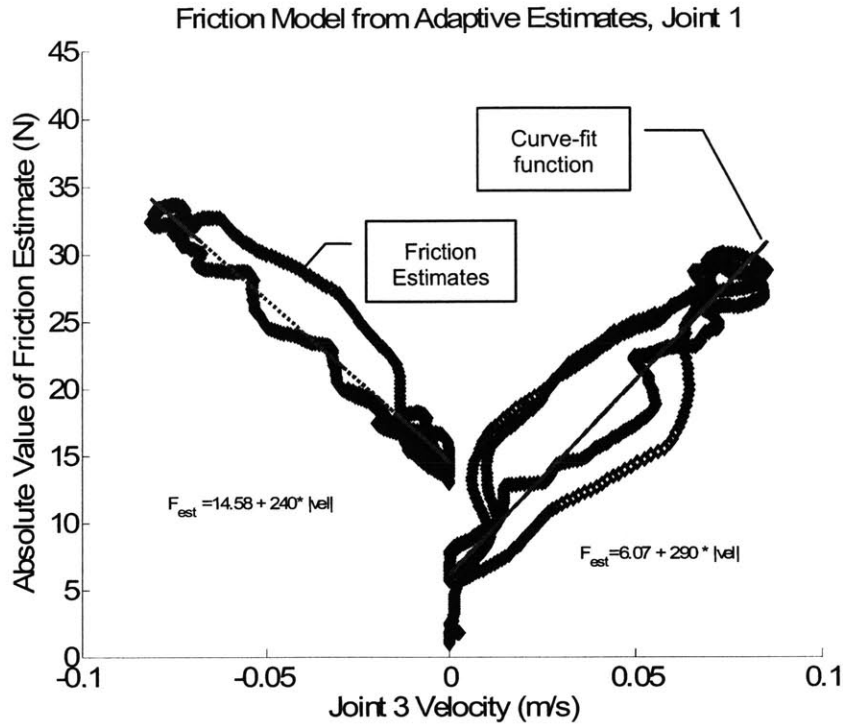


Table 9: Coefficients for the feed-forward model of joint 3

Joint velocity	$a_1$	$a_2$
Positive	6.01 N	289 Ns/m
Negative	14.58 N	240 Ns/m

#### 4.3.4.4: Joint 4

The adaptive gains necessary to provide stable tracking in position control mode result in an estimate of friction that is too noisy to be used to make a feed-forward model. However, the overall amount of friction in joint 4 is extremely low (on the order of 0.1 Nm). This friction is insignificant compared to the disturbance forces that the user places on the joint when moving the force handle, and therefore no feed-forward friction compensation is used on joint 4 during insertion control.

In this section, the adaptive friction estimator output from position control mode was shown to provide data adequate for estimating a feed-forward model of friction in three joints of the Adept robot. The effects of friction in the other joint were determined

to be insignificant compared to the direct forces applied on the joint by a user. This feed-forward friction compensation is used during the insertion control mode to improve the response of the robot the user and environment inputs.

## **4.4 Insertion Control Tests**

The insertion control tests are separated into two groups: open-loop force input tests, and human in the loop tests. The purpose of the open loop tests is to evaluate several different admittance laws, and to ensure that the insertion control algorithm behaves as expected. The purpose of the human in the loop tests is to show that the insertion control algorithm does, in fact, allow an user to insert a payload with similar tolerances as the light payload on the full scale manipulator, and to evaluate qualitatively the effects of different contact gains on the admittance law.

### **4.4.1 Control Notes**

The model-based feed-forward algorithm developed in Section 4.3.4 is used during all insertion control tests in joints 1, 2, and 3. Joint 4 does not use friction compensation. The model-based feed-forward algorithm used during insertion control mode acts only upon the sign of the joint velocity, not a composite variable of joint velocity and joint error, as used in the position control mode friction compensation. Preliminary informal feedback from users of the manipulator indicated a strong dislike for the feel of a feed-forward friction algorithm using a composite variable of joint velocity and joint error. Users commented that the manipulator felt like it was "hunting" for the desired joint location instead of reacting to their inputs. Therefore, using the sign of a composite variable of joint velocity and error in the friction compensation was quickly discarded in favor of an algorithm using only the sign of velocity. User comments on this form of friction compensation are discussed in section 4.4.5.

Additionally, a gain of less than one (0.9 in joints 1 and 2, 0.8 in joint 3) is applied to the estimate of friction from the model-based algorithm to ensure that friction is never overcompensated. A small dead zone was used on the user and contact force sensors to prevent movement of the desired position of the manipulator due to sensor

noise. Other than these modifications, the insertion control on the Adept is unchanged from the control description of the full-scale manipulator in Chapter 2.

#### 4.4.2. Horizontal Open Loop Force Impact Experiment

The first open loop experiment is designed to ensure that the manipulator reacts in a stable manner as it impacts a rigid object under insertion control. The single peg payload (see Figure 47) will be used for this test. The experimental setup is shown in Figure 60, and a depiction of the test is shown in Figure 61. The payload of the manipulator begins the test several centimeters away from a rigid object. A simulated constant 10N force is applied horizontally to the user force handle, moving the desired endpoint of the manipulator towards the rigid object. The manipulator moves forward in the direction of the force, and impacts the rigid object.

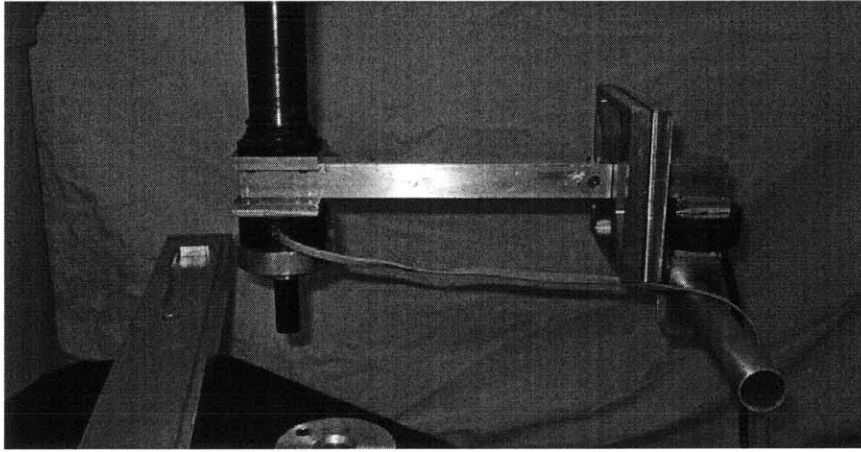


Figure 60: Experimental setup of the horizontal open loop impact test

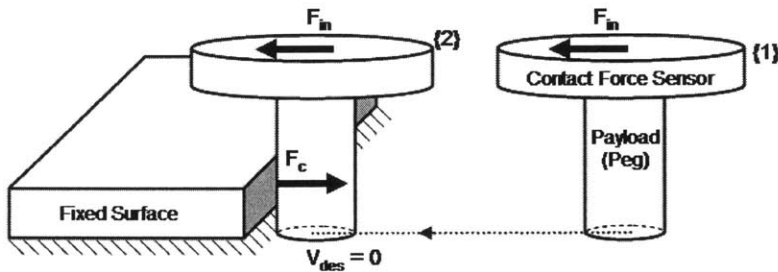


Figure 61: Ideal depiction of the horizontal open loop impact test

The contact force sensor then registers a contact force, and the desired endpoint of the manipulator moves according to the admittance law on both forces. Ideally, after a few

seconds, the manipulator should have a desired velocity of zero, and the manipulator will be pressing on the rigid surface with a force equal to the user gain multiplied by the user input force.

In Appendix B, viscous contact admittance laws of less than 0.01 m/s/N are shown to be stable for this manipulator. With this knowledge, four combinations of user and contact admittance laws are constructed (Table 10). These laws will be used in both the open-loop and user in the loop evaluations of the manipulator. Each admittance law has the same user admittance, and the contact admittance is varied over a factor of ten within the stable range. Effectively, four different contact admittances are tested with varying user gains to keep the free-space response of each admittance law identical.

**Table 10: Translational admittance gains used in the open-loop tests**

Contact Gain	User Admittance	Contact Admittance
1	0.01 m/s/N	0.01 m/s/N
0.5	0.01 m/s/N	0.005 m/s/N
0.2	0.01 m/s/N	0.002 m/s/N
0.1	0.01 m/s/N	0.001 m/s/N

To a user, this means that all four admittance laws feel identical when the manipulator is not in contact with the environment, but they exhibit very different force amplification behaviors in contact with the environment. The four admittance laws are referred to by the ratio of contact to user admittance contact admittance, which is the inverse of the user gain of each admittance law. In this open-loop impact test, this means that the manipulator will be traveling at the same velocity upon impact, and the variance in contact behavior is a function of the contact admittance.

Figure 62A, C, E, and G show the input and contact force in the direction of motion for the horizontal impact tests for the various contact gains. Figure 62B, D, F, and H show the actual and reference positions of the endpoint of the manipulator for the horizontal impact tests along the path of motion of the endpoint. The reference position is the position calculated by applying forward kinematic transforms to the desired joint positions used in the joint controllers.

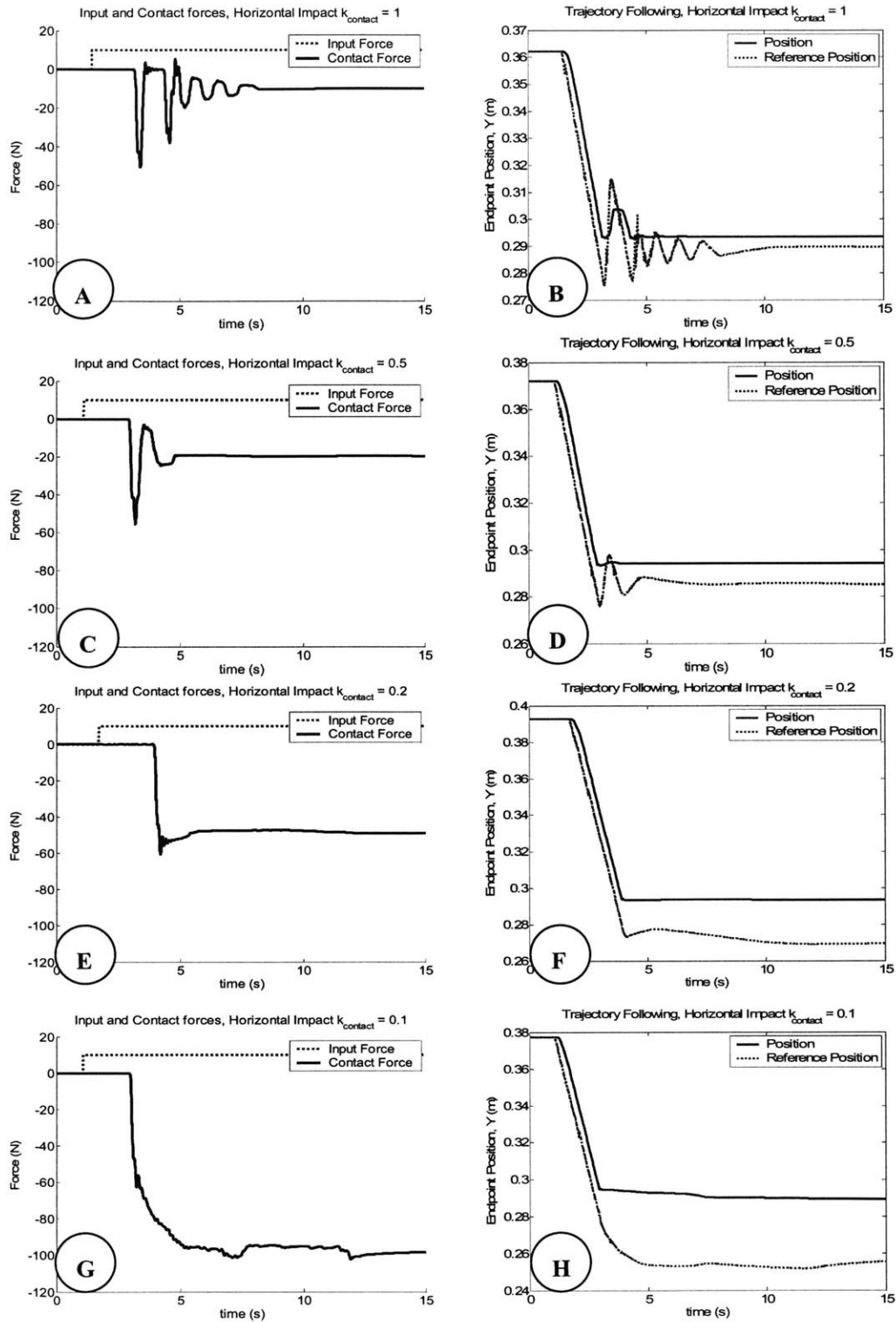


Figure 62: Plots of user vs. contact forces and reference vs. actual endpoint position for the horizontal open loop impact test



The plots in Figure 62 demonstrate that the manipulator behaves as expected in these tests. The contact force converges to a value equal to the inverse of the contact gain multiplied by the 10 N input force, and the desired position of the manipulator is inside the rigid object, causing the manipulator to press against the object. Some interesting phenomena are apparent when comparing the results of the varying contact admittances. When  $k_{\text{contact}}=1$  (Figure 62A and B), the contact force is initially oscillatory, and the manipulator bounces off of the rigid body before settling. The oscillatory force behavior is a result of the effects of the initial contact causing a larger force than the input force, temporarily pushing the desired position of the end-effector off of the rigid body. This effect would possibly be reduced if an actual user were operating the manipulator, as a user would push the manipulator slightly harder into the rigid body if it began to lift off. When  $k_{\text{contact}}=0.5$  (Figure 62C and D), the oscillatory force behavior is significantly reduced, and the manipulator remains in contact with the environment after the impact. When  $k_{\text{contact}}=0.2$  (Figure 62E and F) and  $k_{\text{contact}}=0.1$  (Figure 62G and H), this oscillatory behavior is not seen. A final interesting behavior is observed when  $k_{\text{user}}=0.1$ , as the manipulator continues to move forward once it contacts the "rigid body". This is due to the fact that the 100N contact force needed to offset the 10N input force is sufficient to slightly tip the workpiece that the "rigid body" is mounted to off the floor.

This experiment demonstrates the differences which occur in the contact force profile after an impact as the contact admittance gain is varied. It is unclear from this experiment if the oscillations and other behavior are purely a function of contact admittance, or if the behaviors vary with the force and speed of impact. This could be further examined by applying different user forces to these same admittance laws, resulting in different impact speeds, and observing the contact force response.

#### **4.4.3. Vertical Open Loop Force Impact Experiment**

The next open loop test is designed to ensure that the manipulator reacts in a stable manner when impacting a rigid object vertically. The test again consists of the manipulator moving the single peg payload into contact from a position several centimeters away (Figure 63). The input force in this test is provided by a 5 N weight attached to the user force handle, which provides a slightly more accurate representation

of an actual user than a simulated force. The manipulator then moves the payload downward until it impacts a rigid object and comes to rest. The same translational admittance laws were tested as in the horizontal impact test.

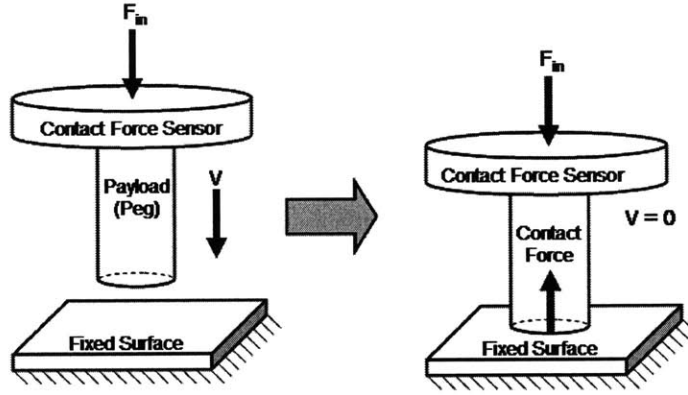


Figure 63: Depiction of the ideal vertical open loop impact test

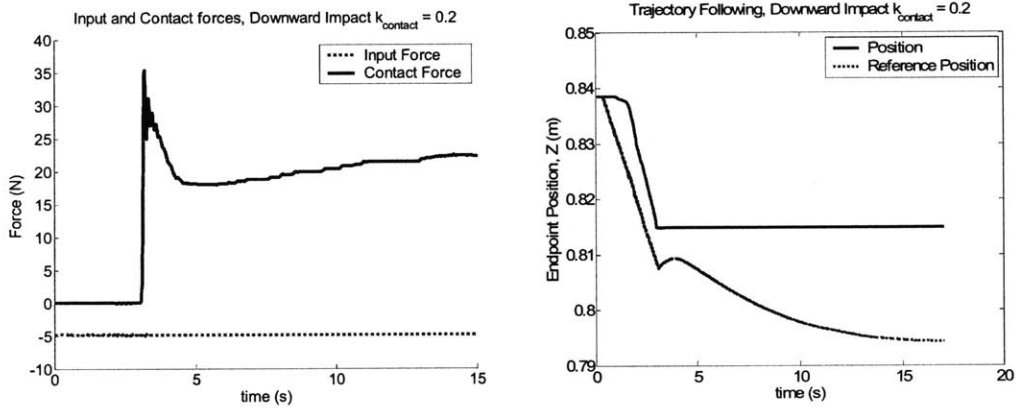


Figure 64: Force and position results from the vertical open loop force impact test with  $k_{contact}=0.2$

The results from this test again show that the manipulator behaves much as it did in the horizontal tests. For brevity, only the force and position plots of the  $k_{user} = 5$  test are shown. One slight difference from the previous tests is that the contact force converges to its final value at a much slower rate. This is likely due to uncompensated joint friction in joint 3 slowing the response of the joint when it is in contact with the environment, since the friction compensation is not applied when the velocity is zero.

#### 4.4.5: Open Loop Compliance Experiments

The next two experiments demonstrate the compliant behavior of the admittance control law when in contact with the environment.

##### 4.4.5.1: Chamfer Behavior Experiment

In this experiment, shown in Figure 65, the payload is pushed downward by a constant user force. The peg is positioned above its mating geometry, which is a hole with a 0.3mm clearance and 3mm 45° chamfer (Figure 65). For drawings of the payload and mating geometry, see section 4.2.4 and Appendix F. The downward input force moves the peg payload downward, into contact with the chamfer. The contact forces from the chamfer then act to push the peg towards the hole. This test was performed using the admittance law described in section 4.4.2 with  $k_{\text{contact}}=0.2$ .

Figure 66 shows the trace of the manipulator endpoint from a successful chamfer insertion test. The trajectory is shown in the manipulator coordinate frame, as shown in Figure 45. The solid line down the middle of the circles is the path of the center point of the peg. The circles represent the edges of the peg at 15ms intervals. A horizontal movement at  $Z = 0.78$  m occurs as a result of the impact of the peg with the chamfer.

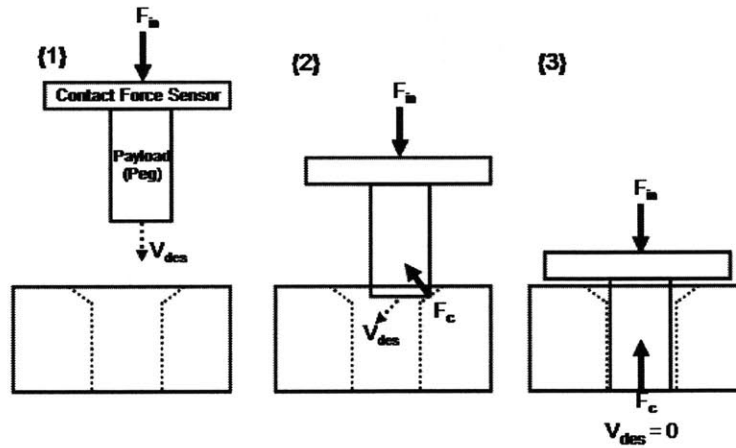
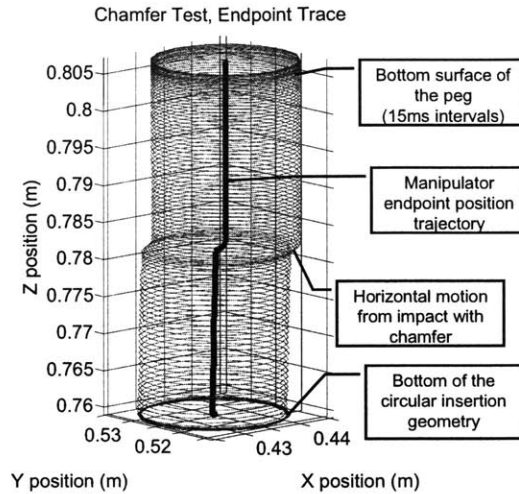
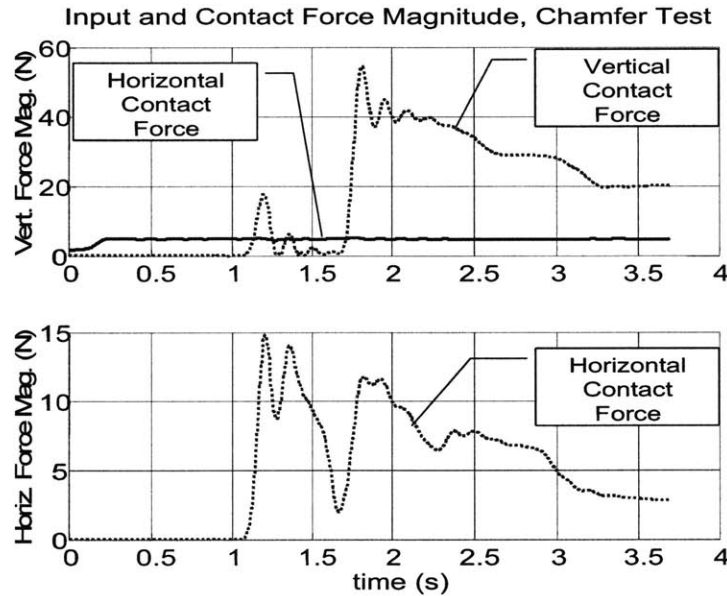


Figure 65: Diagram of the ideal insertion behavior of the manipulator to a chamfered hole



**Figure 66: 3-D trace of the manipulator during the chamfer insertion test.**



**Figure 67: Plot of the contact and user forces during the chamfer insertion test**

The manipulator quickly moves to the side into the hole, and slides to the bottom of the hole. Force plots of the input and contact force are shown in Figure 67. The impact with the chamfer occurs just after 1 s, and causes a small vertical reaction force, along with a larger horizontal force, which, as seen in Figure 66, moves the peg towards the center of the hole. The horizontal force then decreases until about 1.75 s, when the peg reaches the bottom of the hole.

#### 4.4.5.2: Corner Settling Test

This test, shown in Figure 68, tests the compliance of the control system as it moves horizontally into a rigid body, and slides along the body until it comes into contact with a concave corner. The endpoint of the manipulator should then stop, and the contact force should stabilize to a value equal and opposite to the input force multiplied by the user gain. A plot of the trajectory of the manipulator is shown in Figure 69.

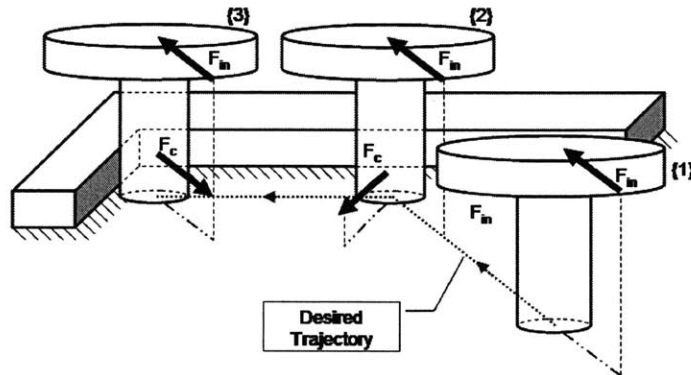


Figure 68: Diagram of the ideal corner settling test

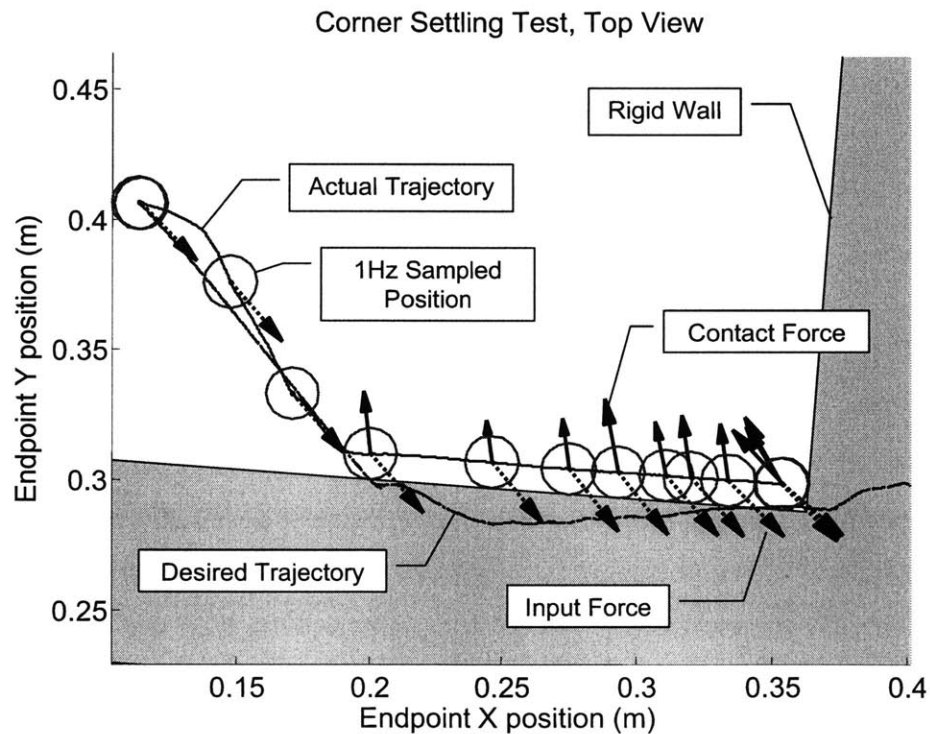


Figure 69: Top view of the manipulator trajectory during the corner settling test

The trajectory plot shows the desired path and actual path of the manipulator. The contact and user force vectors, sampled at a rate of 1 Hz and scaled by the user force gain, are also shown. By combining the information in this plot with the force plot of Figure 70, the behavior of the manipulator can be understood. A simulated input force of 10 N is applied to the user force handle at approximately a 45° angle to the rigid surface. The peg moves forward, towards the surface. At about 4.5 s, the peg impacts the surface. The contact force modifies the desired velocity to pull the manipulator along the surface. The noisy forces from surface friction as the manipulator moves along the surface can be seen in the contact force plot, and the sampled manipulator positions show that the endpoint speed varies as it slides along the surface. At approximately 12 seconds, the endpoint of the manipulator impacts the corner. The contact force then converges to a magnitude of approximately 5 times the input force, in the opposite direction, as expected. This compliant behavior, which allows the manipulator to slide along rigid surfaces, even with simple open loop force inputs, is exactly what is needed to insert and move a payload down a slot. Even if a user is pushing in a slightly incorrect direction, the contact force counteracts the user force perpendicular to the wall, and changes the desired velocity so the manipulator is pulled along the wall. This behavior demonstrates the insertion controller resistance to jamming from a user applying forces in a slightly incorrect direction.

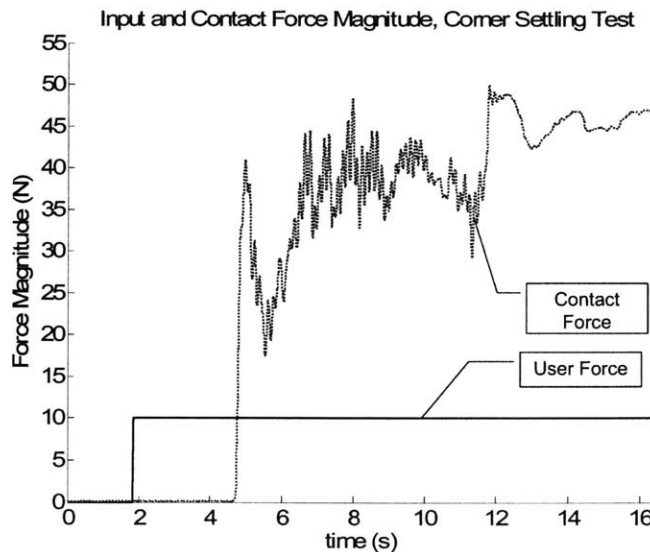


Figure 70: Force magnitude plot of the corner settling test

#### **4.4.5: Human in the Loop Tests**

The insertion controller is designed to be operated with a user in the loop, and in order for the controller to be successful, the user must be able to use the robot to insert a payload. In the full-scale manipulator, the user will sometimes have limited or no visual feedback, and will have to rely on tactile clues from the robot and his knowledge of the payload-environment system to perform the insertion task. All human in the loop tests discussed in this section are performed with the two lug payload with insertion geometry resembling the light payload of the full scale manipulator. For a list of tolerances and drawings of the payload and insertion geometry, see section 4.2.4 and Appendix F.

##### **4.4.5.1: Successful Insertion**

For all four contact admittance gains discussed previously, and both the single peg and two lug payloads, a user can acquaint himself with the manipulator and perform an insertion task with visual feedback with only a few minutes of practice. Practice allows the user to formulate a mental model of the insertion geometry, and to utilize the geometry to aid in the insertion task when the user has limited or no visual feedback. One particular method of insertion that allowed an experienced user to successfully insert the payload without visual feedback is shown in Figure 71. First, the payload is brought to within a few centimeters of the insertion geometry. Second, under insertion control, the user moves the payload downwards into contact with the environment. Third, maintaining a downward force, the user pushes the payload sideways until the rear lug enters the hole. The user is able to feel the sideways force from the hole, as the payload is not able to move sideways, and can only rotate slightly about the lug in the hole. Fourth, the user slides the payload forward until it meets resistance from the slot narrowing. The front lug is now slightly to the side of its hole, but is in the correct position along the axis of the payload. Fifth, the user then twists the payload until the front lug engages in the hole. The user can feel this lug engaging because the payload can no longer be rotated. Sixth, the lugs are pressed to the bottom of the hole, and the user presses forward until the payload is in the fully forward position.

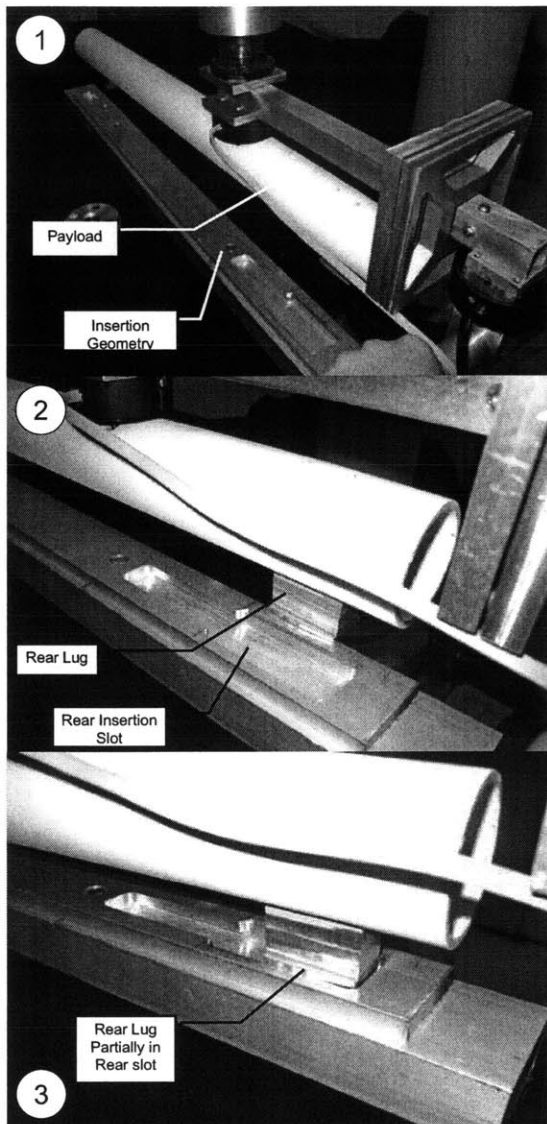
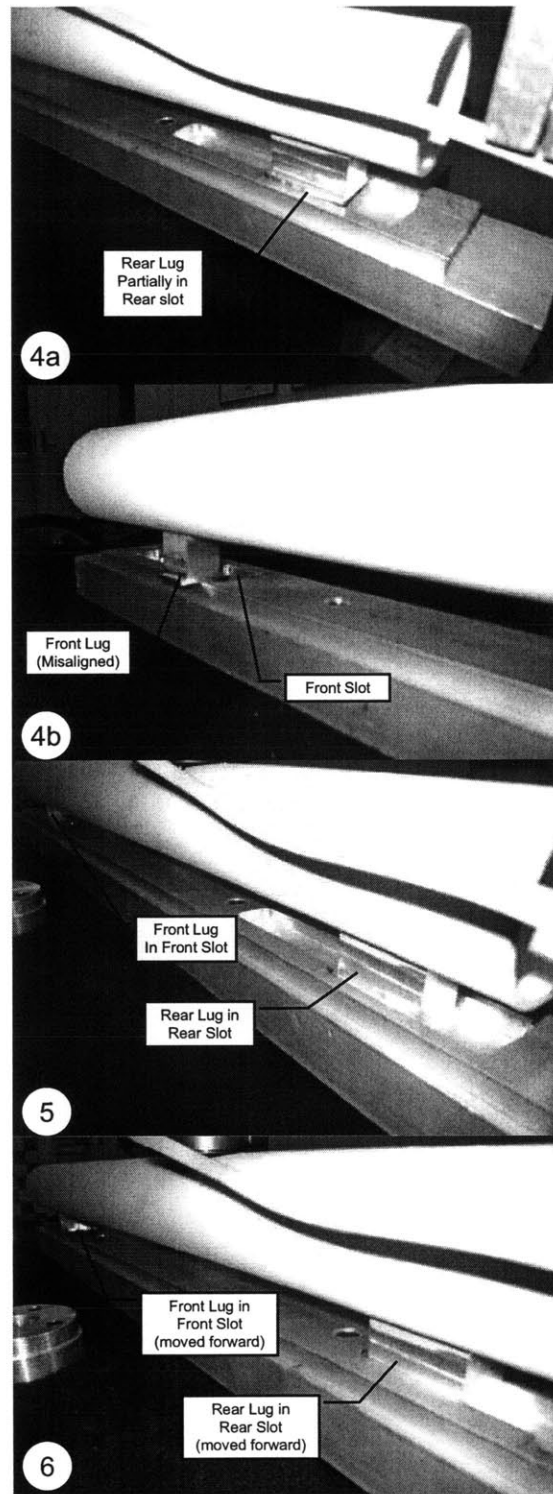


**Figure 71: Step-by-step demonstration of a successful payload insertion.**

**1:** The payload is brought near the insertion point. **2:** The payload is pressed down into contact with the surface. **3:** The payload is pushed sideways until the rear lug engages with its hole. **4:** The payload is pushed forward until the rear lug contacts the front of the hole. **5:** The payload is rotated until the front lug engages in its hole. **6:** The payload is pushed down and forward until it reaches the end of its slot.





A similar insertion process could be used on the full scale manipulator with the challenging insertion geometry of the light payload. Using this method of insertion and the  $k_{\text{contact}} = 0.2$  admittance law, one experienced user of the manipulator was able to perform an entire start to finish insertion with an average time of ten seconds, and as fast as six seconds. With limited visual feedback (only looking at the rear lug), his ability to insert the payload was only slightly slowed. Without any visual feedback aside from an initial glance at the orientation, he was capable of inserting the payload in 20-30 seconds. He reported that the most difficult part of the no visual feedback test was in initially finding the hole for the rear lug. Once this hole was located, engaging the second lug was not difficult, and sliding the payload inside the slot was no more challenging than with visual feedback. Comments from less experienced users will be discussed in Section 4.4.5.3.

#### 4.4.5.2: Slot Sliding Test

One quantitative evaluation of the manipulator under human control is an examination of the contact forces that occur as the user moves the payload down the slot. A diagram of this test is shown in Figure 72. With the two-lug payload in the slot, a user pushes at an angle to the slot. The reaction contact forces push the payload sideways along the slot. The combined forces from the user and contact create a desired velocity of the payload along the axis of the slot, moving the payload forward.

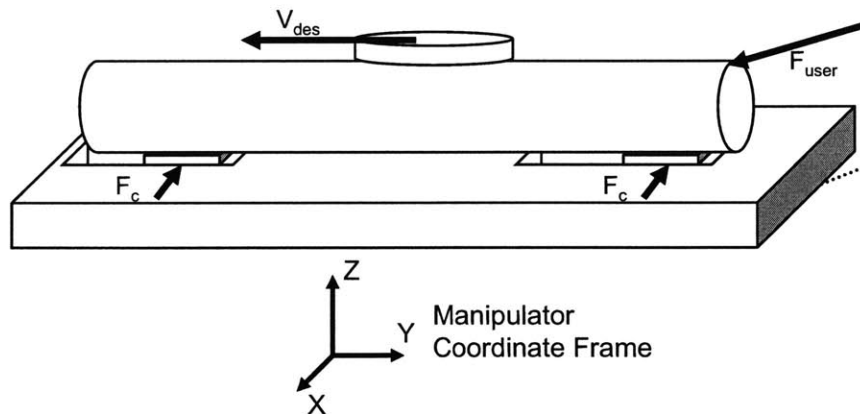
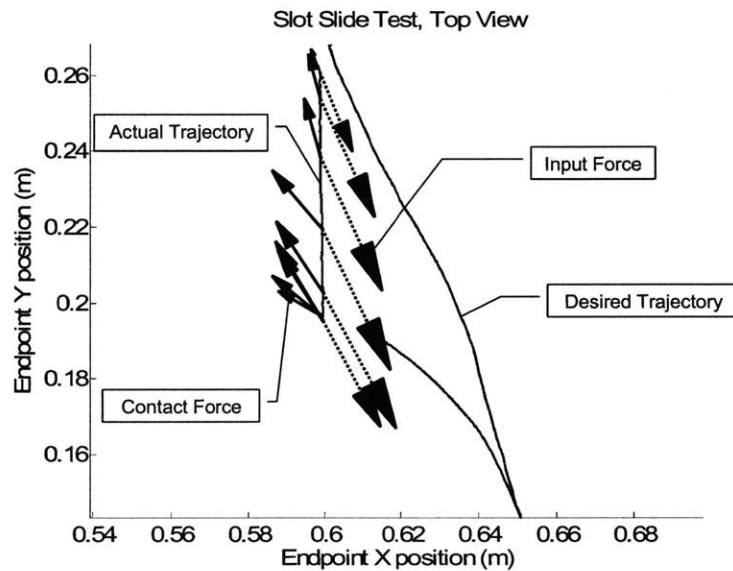


Figure 72: Diagram of the slot sliding test

The slot is aligned with the Y axis of the manipulator as defined in Figure 45 and shown in Figure 72, and the payload is positioned at the entrance of the slot. The contact

admittance gain during this test is set to 0.2. Figure 73 shows a trace of the trajectory of the manipulator as the payload moves down the slot, as well as the scaled user and input force vectors sampled at 1 Hz. It is seen that the user pushes at approximately a  $30^\circ$  angle to the slot. This pushes the desired position of the manipulator into the rigid insertion geometry. The manipulator then pulls the payload down the slot. Figure 74 shows the user and contact force magnitudes during this test. By the end of the trajectory, the contact force is approaching the steady state value of five times the input force. Corresponding to this, the desired trajectory in Figure 73 can be seen to approach a direction parallel to the slot. Figure 75 shows that despite the variance in the contact force compared to the reasonably stable user force, the progress of the manipulator as it moves down the slot is steady.



**Figure 73: Top view of the manipulator trajectory, user force vectors, and contact force vectors during the slot sliding test**

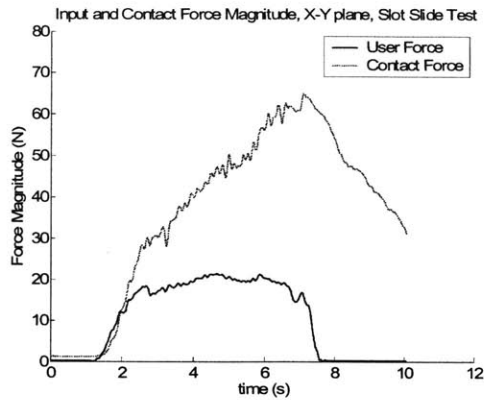


**Figure 74: User and contact force magnitude plot during the slot sliding test**

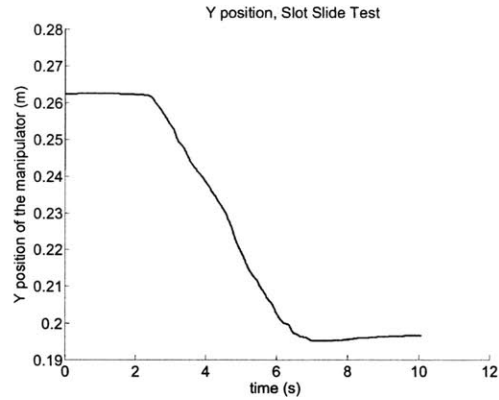


**Figure 75: Position plot of the manipulator along the slot during the slot sliding test**

#### 4.4.5.3: User Comments and Qualitative Analysis

A small survey of novice users was used to judge the usability and learning curve of the insertion controller (See Appendix G for the questionnaire). The purpose of this survey was not to gain statistically significant data, but to receive general feedback about the differences in several iterations of the insertion controller. The users attempted to perform an insertion task with the two-lug payload. Each user tested insertion controllers with contact force gains of 1, 0.2, and 0.1, and tried each controller with and without friction compensation. They were then asked to rate each controller in several categories, including their ability to insert a payload with visual feedback, with partial visual feedback, and with no visual feedback. They were also asked to rate how well they could "feel" the environment through the manipulator, and if they felt in control of the manipulator, as well as their overall rating of the controller.

Due to a hardware malfunction, the survey sample was limited to two users. Among those two users, however, some trends did appear in the evaluation of the controllers.

Both users rated the admittance law with a contact gain of 0.2 and feed-forward friction compensation as their most preferred controller. The controller with a user gain of 0.1 felt "more eager to push itself into place and fight against alignment" than the controller with a contact gain of 0.2, which "had enough gain to pop [the payload] into alignment, but did not try to push against contacting metal".

Both users were able to complete an insertion task reasonably easily with visual feedback with all controllers. One user was able to quickly learn to insert the payload with partial visual feedback (only viewing the rear lug of the payload) for all three controllers, although the only controller he rated as 'excellent' in this ability was the controller with a contact gain of 0.2 and friction compensation. The other user was able to insert the payload with partial visual feedback for controllers with contact force gains of 1 and 0.2, but had great difficulty in inserting the payload with a contact gain of 0.1, creating several situations where one lug was inserted, but the other was not. Both users had difficulty inserting the payload without visual feedback with all controllers. However, one user, after some practice, was able to insert the payload with the controller with a contact gain of 0.2 both with and without friction compensation with some regularity using a method similar to that described in Section 4.4.5.1. As a final note, both users felt that their ability to use all of the controllers would increase dramatically with practice, and felt that the 20 to 30 minute evaluation of six controllers was not sufficient to reach a high level of proficiency with the manipulator.

Both users rated the controller with feed forward compensation equal to or better than its counterpart with no friction compensation in all categories for all tested user gains. In particular, the friction compensation seemed to improve the user's perceived "feel" of the environment.

This test of novice users, though abbreviated, shows that the fundamental insertion control algorithm can successfully be utilized to insert payloads, even by inexperienced users. The user comments indicate that a properly selected contact gain and the implementation friction compensation can have a positive impact on the usability of the manipulator. A contact admittance gain of 0.2 appeared to provide a good tradeoff between having enough power to overcome minor environmental forces, and providing a user with too much power. It will be interesting to see if a similar gain is equally well-suited for the full-scale manipulator.

## **4.5 Summary**

In this chapter, the control system described in Chapter 2 was implemented on a scaled-down, four-degree of freedom manipulator. Both the position and insertion

controllers were implemented and successfully tested. The adaptive friction algorithm was shown to increase the tracking ability of the manipulator under position control. Using the output of a friction estimator to formulate a model of friction was shown to be a valid manner of formulating a feed-forward model of friction. The insertion controller was shown to have predictable, compliant behavior to open-loop force inputs. Finally the combination of the position and insertion controller was shown to provide an intuitive interface allowing users to successfully maneuver and insert a representative mock payload.

## **CHAPTER 5: CONCLUSIONS**

---

This thesis presented the design and evaluation of a control system to enable the user of a high-precision, heavy lift manipulator to acquire, maneuver, and insert heavy payloads with tight tolerances. It has also demonstrated the flexibility of this control architecture by applying it to a lower capacity laboratory manipulator.

Chapter 2 detailed the two modes of the controller: a position control mode for use when the manipulator is operating in free space, and an insertion controller for when the manipulator or its payload would come into contact with the environment. Both controllers utilize joint friction and ship motion compensation to improve their performance, as well as decentralized PID joint controllers. These two modes differ in several different ways, including the method of user input, and the method of joint friction compensation. During position control, the user inputs desired position velocities with a joystick, and during insertion control mode, the robot acts as a force amplifier as the user pushes on a force handle located near the payload. The position control algorithm uses a combination of sensor-based and adaptive friction compensation in order to improve performance. A novel method of utilizing the output from adaptive friction estimators during the position control mode to formulate a feed-forward model of friction during insertion control mode was presented.

Chapter 3 demonstrated the performance of both position control and insertion control algorithms in dynamic simulation. The necessity of dedicated friction compensation was shown, and the ability of the position control algorithm to predictably maneuver a payload in free space was demonstrated when the friction compensation algorithms detailed in chapter 2 were implemented. The estimates of friction during this motion were used to make a feed-forward model of friction which was shown to be at least 80% accurate for the expected range of operation of the joint motors. The insertion control algorithm was shown to have stable contact with the environment, allow a user to

make fine motions in contact with the environment, and was shown to be capable of inserting the most complex payloads with only simple open loop force inputs.

Due to hardware difficulties, the full-scale manipulator was not available to test the control algorithms developed in Chapter 2. Therefore, in Chapter 4, the position and insertion control algorithms were implemented and tested on a scaled-down laboratory manipulator. The adaptive algorithm improved the tracking performance of the joints of the manipulator, and the output from these estimators was used to form a model of friction used in the insertion control algorithm. Open-loop tests of the insertion control algorithm confirmed that the controller behaved as expected. The insertion control algorithm was used with a human in the loop to perform successful insertion tasks, and feedback from users of the manipulator indicated that the feed-forward friction compensation algorithm improved the user's feel of the environment and ability to control the manipulator. User feedback was also used to evaluate user preferences when varying the human amplification gain of the manipulator.

### ***5.1 Suggestions for Future Work on this Project***

While the results presented in this paper demonstrate the successful implementation of the control algorithms on a simulated full-scale manipulator and a scaled down laboratory manipulator, the controller has yet to be validated on the actual hardware it was designed for. Work remains in the area of implementing and tuning the algorithms on the full-scale manipulator. Implementation of the control algorithms on the full-scale manipulator will likely involve extensive tuning and modification of the control algorithms to deal with the difficulties which inevitably arise on a complex system to be used in the field. Additionally, studies of the effects of disturbances such as ship motions, modeling errors, and sensor errors on the performance of the manipulator, particularly on the ability of the adaptive estimators to form a feed-forward model of friction, would be useful.

One particularly likely source of manipulator modeling error which could lead to reduced manipulator accuracy is the positioning of the payload on the manipulator. The payload is secured by hand, and it is likely that the position of the payload will vary by several centimeters from insertion task to insertion task. This could lead to errors in the

gravity compensation algorithm which would have to be compensated by the joint PID controllers, and these disturbances would be observed as added friction by the adaptive compensators, likely causing degradation in the extracted feed-forward model. One way around this would be to formulate a simple adaptive algorithm using the contact force sensor in conjunction with the joint encoders to identify the position of the payload center of mass. The gravity and base motion sensing algorithm would then be computed using this identified center of mass location instead of the ideal location, and errors from uncompensated gravity and acceleration effects would be minimized.

The current requirements for the control system specify that the manipulator must be operated under human control for all movements. The workload on the user of the manipulator could be greatly reduced if some of the motions of the robot were performed autonomously. Some of the manipulator motions, such as the movement of the payload after acquisition into the carrying position could be treated by the robot as a time or power optimal control problem, and the user could act as a watchdog during this process instead of actively controlling it. This would simplify the workload of the user and improve the throughput of the process, as the user would only have to actively control the manipulator only during acquisition, fine adjustment, and insertion tasks.

Another method of improving the ability of the user to insert large payloads without bilateral force feedback would be to use the position of the manipulator and force feedback from the contact force sensor to map the environment, and identify the position and orientation of the insertion geometry relative to the payload of the manipulator. This output could be used to provide autonomous commands to the manipulator to direct it to the insertion point, or output a video image of the identified geometry to the user of the manipulator for an "augmented user interface". Prior studies have examined the problem of efficiently identifying the shape of an object with position and force information [46,40]. However, these previous studies were performed to identify the optimal means of identifying the shape of an object with precise knowledge of the point of contact and measurement of the surface normal. Expanding this work to identify the position and orientation of a known object with a less precise measurement of force, and multiple possible contact locations the new contributions would be an interesting direction of study.



These suggestions for control system improvement are a natural progression of the problem of allowing a robot to perform a fine insertion task without bilateral force-feedback to the user. The necessity of these additional algorithms may increase as robotic hardware increases in capability and the expected throughput of each manipulator increases. The control architecture presented in this thesis has been shown to allow successful insertion of payloads in simulation and in a scaled-down laboratory manipulator for the current design requirements. These algorithms will likely need to be adjusted when applied to the full-scale manipulator or other similar systems, but they provide a framework which will allow a human to utilize the strength of a robotic manipulator to lift and insert large payloads and perform other tasks without bilateral force-feedback.

## REFERENCES

---

1. An, C.H. and J.M. Hollerbach. "Dynamic Stability Issues in Force Control of Manipulators." Proceedings of the IEEE Conference on Robotics and Automation. 1987. pp. 890-896.
2. Anderson, R.J., and M.W. Spong. "Bilateral Control of Teleoperators with Time Delay." IEEE Transactions on Automatic Control. Vol. 34, no. 5. pp. 494-501.
3. Armstrong B, Dupont P, Canudas-de-Wit C. "A Survey of Models, Analysis Tools and Compensation Methods for the Control of Machines with Friction." Automatica, Vol. 30, Issue 7, pp. 1083-1138, July 1994.
4. Asada, H, and J.E. Slotine. Robot Analysis and Control. Wiley-IEEE, New York. 1986.
5. Canudas de Wit C., Lischinsky P. "Adaptive Friction Compensation with Partially Known Dynamic Friction Model." International Journal of Adaptive Control and Signal Processing, Vol. 11, 65-80, 1997.
6. Chiaverini, S., B. Siciliano, and L. Villani. "A Survey of Robot Interaction Control Schemes with Experimental Comparison." IEEE/ASME Transactions on Mechatronics, Vol. 4, no. 3. pp 273-285. September 1999.
7. Craig, J.J., P.Hsu, and S.S. Sastry. "Adaptive Control of Mechanical Manipulators." Proceedings of the 1986 IEEE International Conference on Robotics and Automation, Vol. 3, pp. 190-195. April 2006.
8. Deeter T, Koury G, Rabideau K, Leahy M, Turner T. "The Next Generation Munitions Handler Advanced Technology Demonstrator Program." Proceedings of the 1997 IEEE International Conference on Robotics and Automation, pp. 341-345, 1997.
9. DiCicco, Matthew. "Force Control of Heavy Lift Manipulators for High Precision Insertion Tasks." Master's Thesis. Mechanical Engineering Dept. Massachusetts Institute of Technology. 2005.
10. Dohring, Mark and Wyatt S. Newman. "The Passivity of Natural Admittance Control Implementations." IEEE International Conference on Robotics and Automation. 2003. 3710-3715.

11. Draper, J.V., F.G. Pin, J.C. Rowe, J.F. Jansen. "Next Generation Munitions Handler: Human-Machine Interface and Preliminary Performance Evaluation." ORNL/CP-101966, April 1999.
12. Eppinger, Steven D. and Warren P. Seering. "Introduction to Dynamic Models for Robot Force Control." IEEE Control Systems Magazine. 1987. 48-52.
13. Eppinger, Steven D. and Warren P. Seering. "Three Dynamic Problems in Robot Force Control." IEEE Transactions on Robotics and Automation, Vol 8, No 6. 1992. 751-758.
14. Eppinger, Steven D. and Warren P. Seering. "Understanding Bandwidth Limitations in Robot Force Control." IEEE. 1987. 904-909.
15. Friedland B, Mentzelopoulou S. "On Estimation of Dynamic Friction." Proceeding of the 32nd Conference on Decision and Control, Vol. 2, 15-17, pp. 1919-1924, December 1993.
16. Friedland B, Park Y. "On Adaptive Friction Compensation." IEEE Transactions on Automatic Control, Vol. 37, Issue 10, pp. 1609-1612, October 1992.
17. Garretson, Justin. "High-Precision Control of a Heavy-Lift Manipulator in a Dynamic Environment." Master's Thesis. Mechanical Engineering Dept. Massachusetts Institute of Technology. 2005.
18. Glosser, Gregory D. and Wyatt S. Newman. "The Implementation of a Natural Admittance Controller on an Industrial Manipulator." IEEE. 1994. 1209-1215.
19. Gomes S, Santos da Rosa V. "A New Approach to Compensate Friction in Robotic Actuators." Proceedings. ICRA '03. IEEE International Conference on Robotics and Automation, Vol. 1, 14-19, September 2003.
20. Henrichfreise H, Witte C. "Experimental Results with Observer-Based Nonlinear Compensation of Friction in a Positioning System." IEEE Intl. Conference on Robotics and Automation, Vol. 1, 16-20, May 1998.
21. Hogan, N. "Impedance Control: An Approach to Manipulation: Parts 1-3: Theory, Implementation, and Applications." Journal of Dynamic Systems, Measurement and Control. 1985, Vol 107. 1-24.
22. Hogan, N. "Stable Execution of Contact Tasks using Impedance Control." Proceedings of the IEEE Conference on Robotics and Automation, 1987. pp. 1047-1054.
23. Iagnemma K. "Manipulator Identification and Control Using a Base-Mounted Force/Torque Sensor." Master's Thesis, Department of Mechanical Engineering, MIT, 1997.
24. Ishikawa, H., C.Sawada, K. Kawase, and M. Takata, "Stable Compliance Control and its Implementation for a 6 D.O.F. Manipulator." Proceedings of the IEEE Conference on Robotics and Automation. 1980. pp. 98-103.

25. De Schutter, J. and H. Van Brussel, "Compliant Robot Motion II. A Control Approach Based on External Control Loops." *International Journal of Robotics Research*, Vol. 7, no. 4, pp. 18-33, 1988.
26. Jacobsen, S. C., I. D. McCammon, K. B. Biggers, and R. P. Phillips. "Tactile Sensing System Design Issues in Machine Manipulation." *IEEE*. 1987. pp 2087-2096.
27. Aström, K. and T. Hagglund, *PID Controllers: Theory, Design and Tuning*. Research Triangle Park, NC: Instrum. Soc. America, 1995.
28. Kazerooni, H. "Extender: A Case Study for Human-Robot Interaction via Transfer of Power and Information Signals." *IEEE International Workshop on Robot and Human Communication*, 1993. pp 10-20.
29. Kazerooni, H. and Ming-Guo Her. "The Dynamics and Control of a Haptic Interface Device." *IEEE Transactions on Robotics and Automation*, Vol 10. No 4. 1994. pp 453-464.
30. Kazerooni, H., Tsing-luan Tsay, and Karin Hollerbach. "A Controller Design Framework for Telerobotic Systems." *IEEE Transactions on Control Systems Technology*, Vol 1, No 1. 1993. pp 50-62.
31. Khatib, O, and J. Burdick. "Motion and Force Control of Robot Manipulators." *Proceedings of the IEEE Conference on Robotics and Automation*, 1986, pp. 1381-1386.
32. Kim H, Cho Y, Lee K. "Robust Nonlinear Task Space Control for a 6 DOF Parallel Manipulator." *Proceedings of the 41st IEEE Conference on Decision and Control*, Vol. 2, 10-13, December 2002.
33. Lewis, F.L., K Liu, and A. Yesildirek. "Neural Net Robot Controller with Guaranteed Tracking Performance." *Proceedings of the 1993 International Symposium on Intelligent Control*. pp. 225- 231. August 1993.
34. Lischinsky P, Canudas-de-Wit C, Morel G. "Friction Compensation of a Schilling Hydraulic Robot," *Proceedings of the 1997 IEEE International Conference on Control Applications*, 5-7, pp. 294-299, October 1997.
35. Love L, Jansen J, Pin F. "On the Modeling of Robots Operating on Ships." *Proceedings of the 2004 IEEE International Conference on Robotics and Automation*, Vol. 3, pp. 2436-2443, April 26 – May 1, 2004.
36. Love, L.J., J.F. Jansen, and F.G. Pin. "Compensation of Wave-Induced Motion and force Phenomena for Ship-Based High Performance Robotic and Human Amplifying Systems." *ORNL/TM-2003/233*. October, 2003.
37. Luh J, Fisher W, Paul R. "Joint Torque Control by Direct Feedback for Industrial Robots." *IEEE Transactions on Automatic Control*, Vol. 28, No. 1, Feb. 1983.

38. Raibert M. and J. Craig. "Hybrid Position/Force Control of Manipulators." *Journal of Dynamic Systems, Measurement and Control*, Vol. 103, no. 2. pp 126-133, 1981.
39. Massie, T.M., Salisbury, J.K., "The PHANTom Haptic Interface: A Device for Probing Virtual Objects." ASME Haptic Interfaces for Virtual Environment and Teleoperator Systems 1994, In *Dynamic Systems and Control 1994* (Chicago, Nov 1994), pp.295-301.
40. Moll, M. and Erdmann, M. A. "Reconstructing shape from motion using tactile sensors." In *Proc. 2001 IEEE/RSJ Intl. Conf. on Intelligent Robots and Systems*, Maui, HI.
41. Morel G, Iagnemma K, Dubowsky S. "The Precise Control of Manipulators with High Joint-Friction Using Base Force/Torque Sensing." *Automatica: Journal of the Int. Federation of Automatic Control*, Vol. 36, No. 7, pp. 931-941, 2000.
42. Moreno J, Kelly R, Campa R. "Manipulator Velocity Control using Friction Compensation." *IEE Proceedings on Control Theory Applications*, Vol. 150, No. 2, March 2003.
43. Niemeyer G, Slotine J. "Performance in Adaptive Manipulator Control." *Proceedings of the 27th IEEE Conference on Decision and Control*, Vol. 2, 7-9, pp. 1585-1591, December 1988.
44. Olsson H, Astrom K, Canudas-de-Wit C, Gafvert M, Lichinsky P. "Friction Models and Friction Compensation." *European Journal of Control*, Vol. 4, No. 3, 1998.
45. Pfeiffer L, Khatib O, Hake J. "Joint Torque Sensory Feedback of a PUMA Manipulator." *IEEE Transactions on Robotics and Automation*, Vol. 5, No. 4, pp. 418-425, 1989.
46. Schneider, J. L. and Sheridan, T. B. (1990). "An Automated Tactile Sensing Strategy for Planar Object Recognition and Localization." *IEEE Trans. on Pattern Analysis and Machine Intelligence*, 12(8):775-786.
47. Sciavicco L, Siciliano B. Modeling and Control of Robot Manipulators. Springer, London. 2000.
48. Seraji, Homayoun and Richard Colbaugh. "Adaptive Force-Based Impedance Control." *IEEE International Conference on Intelligent Robots and Systems*. 1993. 1537-1544.
49. Seraji, Homayoun. "Adaptive Admittance Control: An Approach to Explicit Force Control in Compliant Motion." *IEEE*. 1994. 2705-2712.
50. Slotine, J.E. "Robust Control of Robot Manipulators." *International Journal of Robotics Research*. Vol. 4, no. 2, pp. 49-64. 1985.

51. Slotine, J.E. and W. Li "On the Adaptive Control of Robot Manipulators." International Journal of Robotics Research. Vol. 6, no. 3, pp. 49-59. 1987.
52. Slotine, J.J. E., & Weiping Li. Applied Nonlinear Control. Englewood Cliffs, NJ: Prentice-Hall, 1991.
53. Spong, M.W, and M Vidyasagar. Robot Dynamics and Control. John Wiley & Sons, New York. 1989.
54. Visioli A, Legnani G. "On the Trajectory Tracking Control of Industrial SCARA Robot Manipulators." IEEE Transactions on Industrial Electronics, Vol. 49, No. 1, February 2002.
55. Volpe, Richard and Pradeep Khosla. "A Theoretical And Experimental Investigation of Explicit Force Control Strategies for Manipulators." IEEE Transactions on Automatic Control, Vol 38, No 11. 1993. 1624-1650.
56. Volpe, Richard and Pradeep Khosla. "Analysis and Experimental Verification of a Fourth Order Plant Model for Manipulator Force." IEEE Robotics and Automation Magazine. 1994. 4-13.
57. Whitcomb, L, S. Arimoto, T. Naniwa, and F. Ozaki. " Adaptive Model-Based Hybrid Control of Geometrically Constrained Robot Arms." IEEE Transactions on Robotics and Automation, Vol. 13, no. 1. February 1997.
58. Whitney, D.E., "Resolved Motion Rate Control of Manipulators and Human Prostheses." IEEE Transactions on Man-Machine Systems, Vol. MMS-10 No. 2 June 1969.
59. Yoo, B.K. and W.C. Ham. "Adaptive Control of Robot Manipulator Using Fuzzy Compensator." IEEE Transactions on Fuzzy Systems. Vol. 8, no. 2, pp 186-199. April 2000.
60. Youcef-Toumi, K. "Force Control of Direct-Drive Manipulators for Surface Following." Proceedings of the IEEE Conference on Robotics and Automation, 1987. pp. 2055-2060.



## APPENDIX A: JOINT AND ADMITTANCE TUNING

### Joint Controller Tuning:

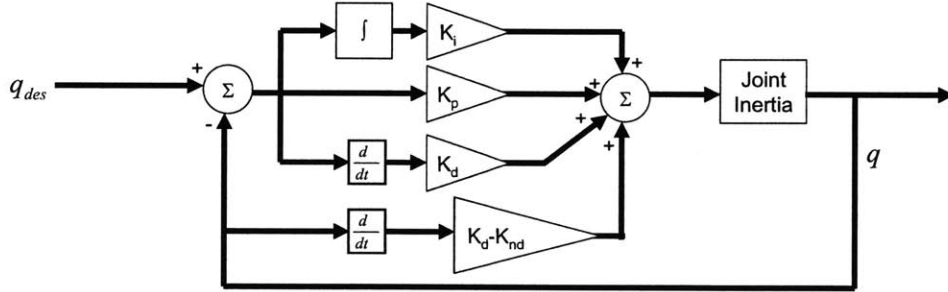


Figure 76: Model used for tuning joint PID gains

The lowest structural resonant frequencies of the heavy manipulator discussed in this paper vary from 5 Hz to 9 Hz, depending on the payload. These frequencies have been determined by a separate finite element analysis of the manipulator structure. To avoid exciting these resonances, the joint and admittance controllers are tuned so that their bandwidth is 1 decade below the resonant frequency.

The model used to tune the joint controllers is shown in Figure 76. The closed loop transfer function that represents this model is

$$\frac{K_D s^2 + K_P s + K_I}{I s^3 + K_{ND} s^2 + K_P s + K_I} \quad (A.1)$$

where  $I$  is the moment of inertia of the robot past the joint, and  $K_P$ ,  $K_I$ ,  $K_D$ , and  $K_{ND}$  are the proportional, integral, derivative, and plant damping gains of the joint controller.  $J$  is a function of joint angles, and can be calculated by using the command 'inertia' found in the Matlab robotics toolbox, or by deriving closed loop equations. The manipulator should be placed in the position where the lowest structural natural frequency occurs. The parameters  $K_P$ ,  $K_I$ ,  $K_D$ , and  $K_{ND}$  are then be varied so that the damping ratio of the closed loop transfer function is 0.707, and the bandwidth of the closed loop transfer

function is below 1/10 of the resonant natural frequency of the system. In this tuning, the  $K_D$  term should be set to roughly half of the  $K_{ND}$  term, and the  $K_I$  should be set to  $K_D/4$ , a value used by the Ziegler-Nichols tuning rules, an accepted tuning standard used when the integral term is wished to eliminate steady-state errors without significantly changing the dynamics of the PD controller. Finally, when the manipulator is used in insertion control mode, the integral gains should be set to zero to eliminate joint limit-cycle behavior due to the contact forces.

**Table 11: PID gains for the joint controllers with the light payload**

Joint	$K_P$	$K_I$	$K_D$	$K_{ND}$
1	62600	2590	10350	20700
2	54500	2240	8950	17900
3	17300	712	2850	5700
4	6500	265	1060	2120
5	5000	192	770	1630
6	1470	43	171	430

In order to improve performance, the output from the integral term is saturated. The maximum allowable output from the joint integral terms is given in Table 12.

**Table 12: Joint controller integral saturation limits**

	$S_i$
Joint 1:	3000 Nm
Joint 2:	3000 Nm
Joint 3:	1000 N
Joint 4:	500 Nm
Joint 5:	500 Nm
Joint 6:	100 Nm

### **Friction Compensation Tuning:**

The torque control loops described in section 2.2.3.1 use a PI control loop to drive the error between the desired torque and the actual torque to zero. The gains for these torque control loops are shown in Table 13. Several parameters in the adaptive friction compensators used in joints 4-6 are tuned to ensure that the estimators track the friction



well without excessive overshooting behavior or noise amplification. The tuned values for these parameters are shown in Table 14.

**Table 13: PI gains for use in the torque control loops for the linear actuators for joints 1-3**

	$K_p$	$K_i$
Right Base Actuator:	2	100
Left Base Actuator:	2	100
Joint 3 Actuator:	2	100

**Table 14: Gains for use in the adaptive friction compensators in joints 4-6**

	$\mu$	$k$
Joint 4:	2	80
Joint 5:	2	40
Joint 6:	2	100

### **Admittance Law Tuning:**

In addition to the joint controllers, the admittance law must be tuned so that the environmental interaction does not lead to control instabilities or excitation on the resonant frequencies of the manipulator.

In this section, a vibration analysis as proposed in [56] and modified to add a gripper compliance and separate payload as in [12] is used to determine a range of stable admittance laws for the insertion controller. A stable admittance law will have a bandwidth sufficiently low to avoid manipulator structural resonances, as well as to avoid resonances arising from the payload-environment interaction. The analysis in this section heavily borrows from the earlier work of DiCicco [9], with small modifications in the method of simulating the robot controllers and approximating damping in the robot.

The model shown in Figure 77 is used to derive state space equations for the robot. The system is approximated as a one-directional, sixth order system of vibrating masses. These masses are the robot, sensor, and payload of the manipulator. A state space vector (A.3) is constructed of the positions and velocities of these masses.

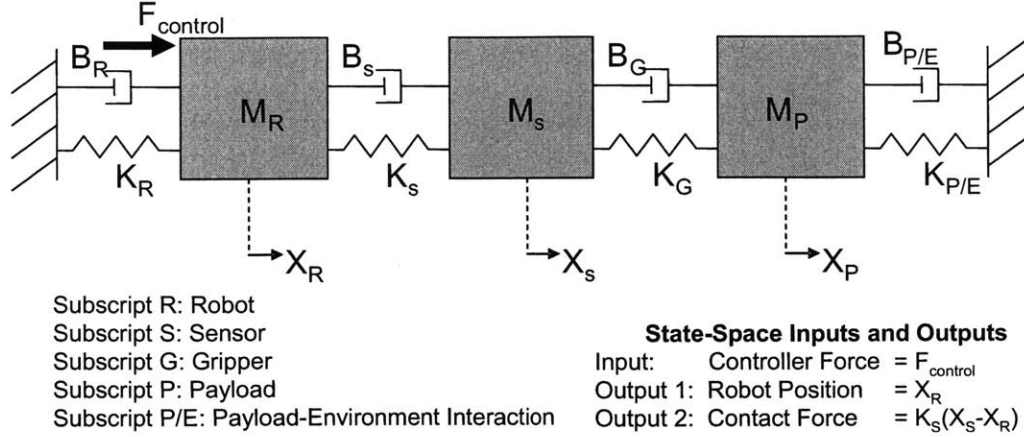


Figure 77: 6<sup>th</sup>-order model used for tuning the admittance law (Adapted from DiCicco [2])

$$\vec{X} = \begin{bmatrix} X_R \\ X_S \\ X_P \\ V_R \\ V_S \\ V_P \end{bmatrix} \quad (\text{A.3})$$

The state space equations (A.4) describe the system and its response to the controller force  $F$ . The output equations (A.5) describe outputs of the system, which are  $X_R$ , the endpoint position of the robot, and  $F_C$ , the force sensed by the contact force sensor. The transfer functions from  $F$  to  $X_R$  and  $F_C$  will be referred to as  $TF_{XR}(s)$  and  $TF_{FC}(s)$ , respectively.

$$\dot{\vec{X}} = \begin{bmatrix} 0 & 0 & 0 & 1 & 0 & 0 \\ 0 & 0 & 0 & 0 & 1 & 0 \\ 0 & 0 & 0 & 0 & 0 & 1 \\ \frac{-(K_R + K_S)}{M_R} & \frac{K_S}{M_R} & 0 & \frac{-(B_R + B_S)}{M_R} & \frac{B_S}{M_R} & 0 \\ \frac{K_S}{M_S} & \frac{-(K_S + K_C)}{M_S} & \frac{K_C}{M_S} & \frac{B_S}{M_S} & \frac{-(B_S + B_C)}{M_S} & \frac{B_C}{M_S} \\ 0 & \frac{K_C}{M_P} & \frac{-(K_C + K_{P/E})}{M_P} & 0 & \frac{B_C}{M_P} & \frac{-(B_C + B_{P/E})}{M_P} \end{bmatrix} \cdot \vec{X} + \begin{bmatrix} 0 \\ 0 \\ 0 \\ 1 \\ 0 \\ 0 \end{bmatrix} \cdot F \quad (\text{A.4})$$

$$\begin{bmatrix} X_R \\ F_C \end{bmatrix} = \begin{bmatrix} 1 & 0 & 0 & 0 & 0 & 0 \\ K_S & -K_S & 0 & 0 & 0 & 0 \end{bmatrix} \cdot \vec{X} + \begin{bmatrix} 0 \\ 0 \end{bmatrix} \cdot F \quad (\text{A.5})$$

This controller force  $F$  is approximated as a PID controller with natural damping, with a transfer function of the form (A.1). The inertia term  $I$  is the diagonal of the endpoint inertia matrix, was calculated using the 'cinertia' command in the Matlab robotics toolbox. The terms  $K_P$ ,  $K_I$ ,  $K_D$ , and  $K_{ND}$  are tuned to  $0.707 \zeta$  and  $1/10$  structural natural frequency bandwidth as before. This control law provides an approximation of the joint controller effect on the payload position. The transfer function  $C(s)$  of joint error to output torque from the controller is shown in (A.6). The natural damping term of the controller does not appear in this transfer function, as  $K_{ND} = B_R$  appears as the robot damping term in the state space equations.

$$C(s) = \frac{K_D s^2 + K_P s + K_I}{s} \quad (\text{A.6})$$

The feedback law can be used to combine the dynamics of the controller and the transfer function from controller input force to position. The dynamics of this inner position controller  $PC(s)$  loop are represented by transfer function from desired position to robot position (A.7).

$$PC(s) = \frac{C(s)}{1 + TF_{XR}(s) \cdot C(s)} \quad (\text{A.7})$$

The desired position of the robot is a function of the contact force multiplied by an admittance law. As discussed in Section 2.3.1, the admittance law is a purely viscous law, where desired payload velocity is directly proportional to the contact force. The transfer function of contact force to desired position is given by equation (A.8).

$$A(s) = \frac{K_A}{s} \quad (\text{A.8})$$

A closed loop transfer function between input force and output force (A.9) can be calculated using the admittance law, position controller, and controller force to contact force transfer function in the forward path with unity feedback.

$$G(s) = \frac{A(s)PC(s)TF_{CF}(s)}{1 + A(s)PC(s)TF_{CF}(s)} \quad (\text{A.9})$$

The bandwidth of the function  $G(s)$  must be limited to  $1/10$  of the structural natural frequency of the manipulator, or  $1/10$  of any resonant frequencies of the payload-gripper-

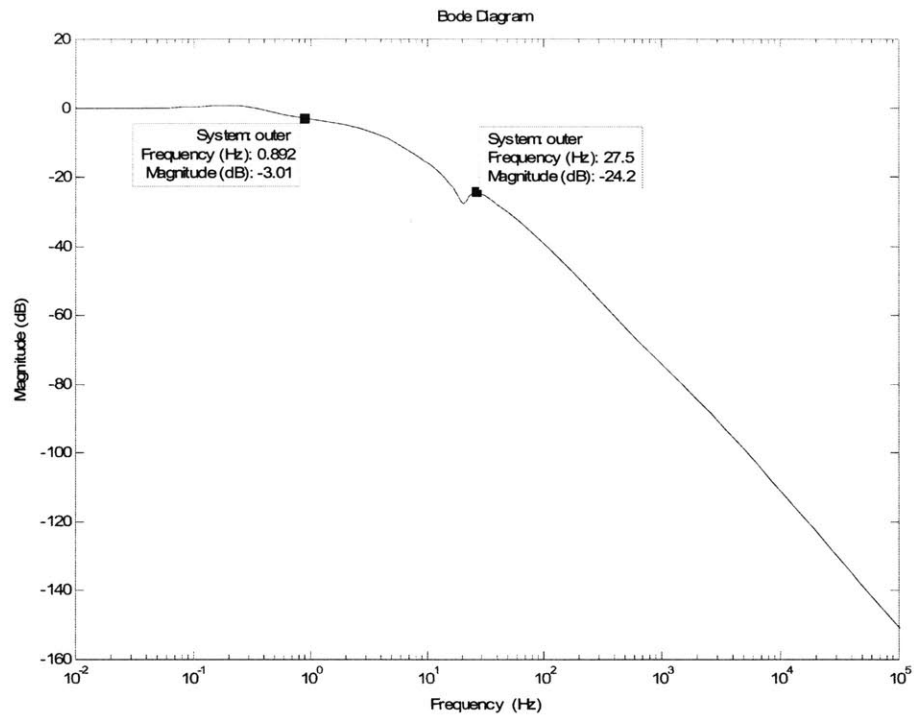


**Figure 78: Bode diagram of the transfer function of input force to output force  $G(s)$  with a translational admittance law  $7.2 \times 10^{-5}$  Ns/m. The bandwidth of 0.9 Hz and the resonant frequency of the payload-environment-gripper system are highlighted.**

environment interaction system. The state-space analysis outlined above was performed with the values in Table 15, and tested for different admittance gains  $K_A$ . A translational admittance gain of  $7.2 \cdot 10^{-5}$  Ns/m was found to have a 0.9 Hz bandwidth, which is a decade below the structural natural frequency of the manipulator, and more than a decade below the lowest natural frequency of the simplified mass-spring-damper system discussed in this section. A rotational admittance law of  $30.0 \cdot 10^{-5}$  Nms/rad was found to have a 0.9 Hz bandwidth as well. A Bode plot of the closed-loop system force response is shown in Figure 78.

**Table 15: Parameters used for adaptive tuning of the heavy-lift manipulator**

	Value (translation)	Value (rotation)	Source
$M_R$	697.1 kg	239.8 kgm <sup>2</sup>	Robot mass or moment of inertia from 'cinert'
$M_S$	1 kg	1 kgm <sup>2</sup>	Approximation that $M_S \ll M_P$ and $M_R$
$M_P$	156 kg	130 kgm <sup>2</sup>	Mass/Inertia of payload
$B_R$	36800 Ns/m	8270 Nms/rad	Natural Damping Gain
$K_R$	0 N/m	0 Nm/rad	Assume motors have no stiffness
$B_S$	500 Ns/m	500 Nms/rad	Approximation that $B_S \ll B_{P/E}$
$K_S$	$5 \cdot 10^6$ N/m	$5 \cdot 10^6$ Nm/rad	Approximation that $K_S \gg K_{P/E}$
$B_G$	5000 Ns/m	4825 Nms/rad	Specified gripper damping, 0.956m b/w grips
$K_G$	$5.5 \cdot 10^5$ N/m	$5.3 \cdot 10^5$ Nm/rad	Specified gripper stiffness, 0.956m b/w grips
$B_{P/E}$	5000 Ns/m	6800 Nms/rad	Estimate of steel damping, 1.36m b/w lugs
$K_{P/E}$	$2.7 \cdot 10^6$ N/m	$3.6 \cdot 10^6$ Nm/rad	Estimate of steel stiffness, 1.36m b/w lugs

This analysis is useful for finding stable admittance laws for the contact force. A manipulator must also have stable interaction with the user. If the admittance gain for the user is sufficiently larger than the contact admittance gain, another analysis should be performed to ensure that user interaction does not create instabilities. However, because humans are orders of magnitude less stiff than the steel on steel contact modeled here, and the user admittance gain is small, it is unnecessary to perform a separate analysis.

# B

## APPENDIX B: ADEPT PARAMETER IDENTIFICATION

### Kinematic Parameters: Denavit-Hartenberg Convention

Link	Axis Name	$\alpha_i$	$a_i$ (m)	$\theta_i$	$d_i$ (m)	type	Range
1	Shoulder	0	0.425	0	0	0	-135° to 135°
2	Elbow	$\pi$	0.375	0	0	0	-135° to 135°
3	Vertical Prismatic	0	0	0	0	1	0 to 0.2 m
4	Screw	0	0	0	0	0	-360° to inf

### Mass and Inertia Parameters:

The mass parameters of the Adept robot were computed in several steps.

1. The mass of link 3 without a payload is identified by applying a sinusoidal desired position to a PD joint controller on joint 3. The joint force is recorded, and the offset of the joint force sinusoid from zero is the gravitational force on the joint. This force was converted into a mass by dividing by the acceleration of gravity.

$$I_{eff3} = M_3 = 1.02 \text{ kg}$$

2. The inertia of link 3 about the axis of joint four with no payload is estimated by using the formula for the moment of inertia of a hollow cylinder:  $I = MR^2$

$$I_{eff4} = I_4 = 1.02\text{kg} \cdot (0.025\text{m})^2 = 6.4 \cdot 10^{-4} \text{kgm}^2$$

3. The effective inertia of the robot about joint 2 with no payload is calculated by applying an open-loop torque to the joint. The deceleration of the joint after the application of motor torque is estimated in addition to the acceleration during the motor torque. The deceleration is then added to the acceleration to estimate the acceleration in the absence of friction. This is a valid assumption assuming Coulomb friction. This allows the calculation of the effective inertia of the robot about joint 2:  $I = \tau/\alpha$

$$I_{eff2} = 0.958 \text{ kgm}^2$$

4. The effective inertia of the robot about joint 1 with no payload is calculated by a similar method as in step three. The angle of joint 2 was varied, and the estimates of the effective inertia at several values of this angle were recorded. A curve was

fit to this data to determine which parameters of the inertia are constant and which vary with  $q_2$ .

$$I_{eff1} = 5.20 + 1.37\cos(q_2) \text{ kgm}^2$$

5. The mass of the payload is measured directly with a scale. The moment of inertia and location of the center of mass of the payload is calculated by estimating the individual moments of inertia and masses of the components of the payload, and combining them. The payload mass and inertia are then added to the effective interias of each joint by the following equations:

$$I_{eff1(+payload)} = I_{eff1} + I_P + M_P(l_1 + l_2 \cos(q_2))^2$$

$$I_{eff2(+payload)} = I_{eff2} + I_P + M_P l_2^2$$

$$I_{eff3(+payload)} = M_3 + M_P$$

$$I_{eff4(+payload)} = I_{eff4} + I_P + M_P l_{cP}^2$$

Due to the small value of  $l_{cP}$  (the distance of the center of mass of the payload from the axis of joint 4), the contributions of the rotation of joint 4 to the effective inertia are ignored for joints 1 and 2. These contributions are several orders of magnitude smaller than other contributions to the effective inertia. Ex:  $I_{eff2}$  would be  $1.06 + 0.004*\cos(q_4)$   $\text{kgm}^2$  instead of  $1.06 \text{ kgm}^2$ .

**Table 16: Mass and inertia properties of the end effector of the Adept robot**

	No Payload	Payload 1	Payload 2
$M_3$	1.02 kg	1.02 kg	1.02 kg
$I_4$	0.00064 $\text{kgm}^2$	0.00064 $\text{kgm}^2$	0.00064 $\text{kgm}^2$
$I_P$	0 $\text{kgm}^2$	0.047 $\text{kgm}^2$	0.125 $\text{kgm}^2$
$M_P$	0 kg	2.09 kg	2.83 kg
$L_{cP}$	0 m	0.206 m	0.039 m
$I_{eff3}$	1.02 kg	3.11 kg	3.85 kg
$I_{eff4}$	0.00064 $\text{kgm}^2$	0.090 $\text{kgm}^2$	0.161 $\text{kgm}^2$

The PD gains for the joint level controllers were tuned to a 1 Hz bandwidth with a damping ratio  $\zeta = 0.707$  using the method outlined in Appendix A. The lowest structural resonant frequency of the manipulator would occur when the manipulator is fully extended, when the robot is in the configuration with maximum effective inertia. Therefore, the maximum values of inertia are used when tuning the joint controllers.

**Table 17: PD gains, Tuned for 1 Hz bandwidth,  $\zeta=0.707$ , payload 2**

Joint	$I_{\text{eff}}$	P Gain	D Gain
1	$6.23 + 1.69 \cos(q_2) \text{ kgm}^2$	400	90
2	$1.48 \text{ kgm}^2$	50	11
3	$3.85 \text{ kg}$	160	36
4	$0.161 \text{ kgm}^2$	5	1.2

### Environmental Parameters:

In order to tune the admittance law as described in Appendix A, information about the environment must be gathered. The method described in [56] will be used to gather information about the spring, damper, and the effective mass of the robot in the oscillating system.

A quasi-static evaluation of the stiffness of the payload-environment system is performed by using the Adept to press on the environment with each payload. The force is recorded with the contact force-torque sensor, and the position is measured by the joint encoder of the Adept. A plot of the results of this test as well as the linear approximation of the spring constant is shown in Figure 79.

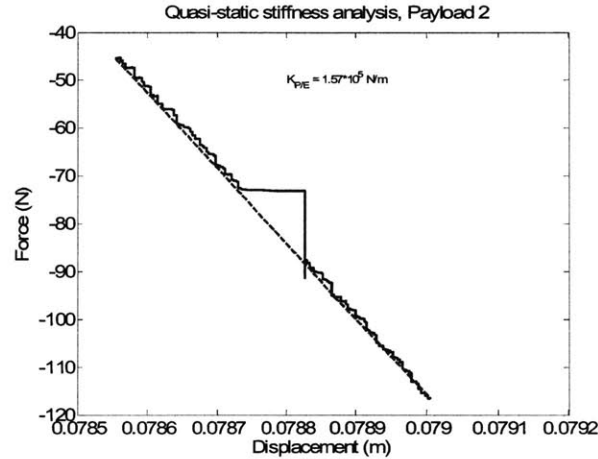


**Figure 79: Quasi-static evaluation of the payload-environment stiffness**



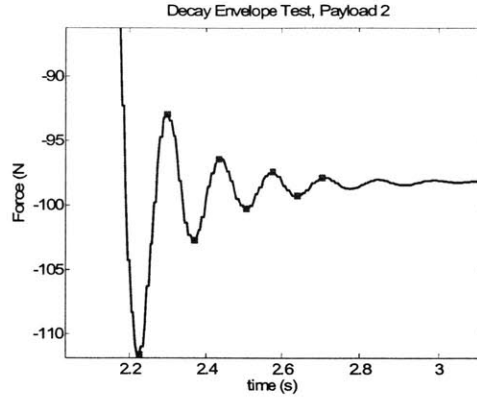


**Figure 80: Plot of the force step response oscillations of the Adept-Environment interaction**

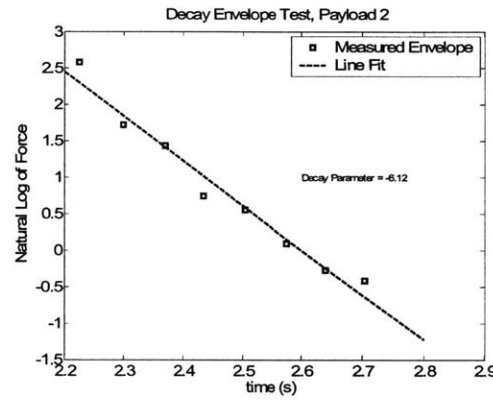


**Figure 81: Plot of the magnitude of the decay envelope of the Adept-environment system. This is used to estimate the decay parameter of the system**

In order to calculate the damping parameters of the environment, the Adept was used to apply a step change in force in contact with the environment. The oscillations that result from this step can be used to calculate the damping properties and natural frequency of the robot-environment system. The lowest natural frequency in the Adept-environment system can be calculated directly from observing the oscillations in Figure 80. In conjunction with the previously calculated environmental stiffness, the approximation

$$\omega_n = \sqrt{\frac{k_{P/E}}{M_R + M_S + M_P}} \quad (\text{B.1})$$

can be used to calculate the mass of the robot.

The natural logarithm of the magnitude of the peaks of the oscillations is plotted against time in Figure 81. The slope of this line is the decay parameter, which can be used to calculate the environmental damping.

In order to calculate the range of stable admittance laws, the analysis described in Appendix A was applied to parameters of the Adept robot. These parameters are shown in Table 18. The admittance controller was tuned so that its bandwidth was limited to 1 Hz (like the position controllers), or a decade below any resonances caused by the environmental interaction. An admittance law of 0.02 Nm/s fits these requirements. However, reducing the admittance to 0.01 Nm/s attenuates the structural resonance significantly more, and is still provides a good response. A bode plot for the input force to output force is shown in Figure 82.

**Table 18: Parameters used for admittance law tuning of the Adept robot**

	Value (Payload 1)	Value (Payload 2)	Source
$M_R$	86 kg	86 kg	Approximation from known stiffness and $\omega_n$
$M_S$	0.17 kg	0.17 kg	Direct Measurement of sensor mass
$M_P$	0.24 kg	1.08 kg	Direct Measurement of payload mass
$B_R$	36 Ns/m	36 Ns/m	Natural Damping Gain
$K_R$	0 N/m	0 Nm/rad	Assume motors have no stiffness
$B_S$	500 Ns/m	500 Nms/rad	Approximation that $B_S \ll B_{P/E}$
$K_S$	$5 \cdot 10^6$ N/m	$5 \cdot 10^6$ Nm/rad	Approximation that $K_S \gg K_{P/E}$
$B_G$	500 Ns/m	500 Nms/rad	Approximation that $B_G \ll B_{P/E}$
$K_G$	$5 \cdot 10^6$ N/m	$5 \cdot 10^6$ Nm/rad	Approximation that $K_G \gg K_{P/E}$
$B_{P/E}$	931.4 Ns/m	$1.15 \cdot 10^3$ Ns/m	Calculated from decay envelope
$K_{P/E}$	$1.99 \cdot 10^5$ N/m	$1.57 \cdot 10^5$ N/m	Calculated from quasi-static test
$\omega_n$	45.4 rad/s	45.4 rad/s	Calculated from oscillation test (7.22 Hz)

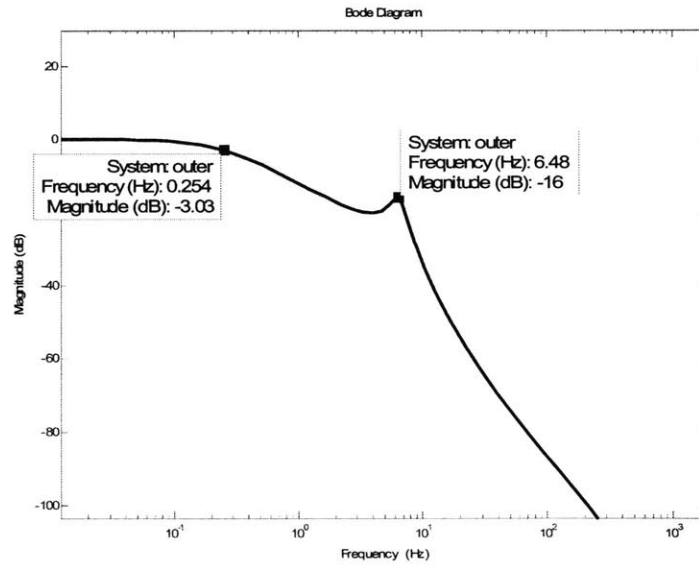


**Figure 82: Bode plot of the frequency response of the Adept admittance law when  $K_A = 0.01$  Nm/s**

## **APPENDIX C: ADEPT JOINT 1 FRICTION MODELING**

Extracting a friction model from joint 1 provides a good illustration of the improvement which occurs as a result of the discontinuous adaptation law. Figure 83 shows a plot of the friction estimate against joint velocity from Joint 1 following a sinusoidal trajectory (see Figure 49) using the composite variable friction compensation algorithm. Figure 84 shows the results of the same test with a discontinuous adaptation law. It is clear that the positive and negative velocity friction profiles are not identical, and instead of being functions of velocity, show a loop behavior. This loop behavior was determined to be a result of sympathetic motion of joint 2. In order to reduce the sympathetic motion, friction compensation to that joint was deactivated. The friction profile extracted from a sinusoidal test with this estimator is shown in Figure 85. The friction has an asymmetric coulomb + viscous profile. The coefficients of this profile were observed to vary when joint two is set to different angles. Data was collected from sinusoidal tests at several angles of joint 2, and the viscous and Coulomb coefficients extracted from these tests are shown in Figure 86 and Figure 87, respectively. The profiles of both Coulomb and viscous coefficients for both positive and negative velocity were found to vary with a roughly symmetric sinusoidal profile about a slightly negative angle of joint 2.

A function (4.1) was derived to describe the effect on the friction profile of joint 1 by varying joint 1 velocity and joint 2 angle.

$$F_{fric} = a_1 + a_2 \cos(q_2 - a_3) + \dot{q}_1(a_4 + a_5 \cos(q_2 - a_3)) \quad (C.1)$$

where  $a_1$  represents the mean value of coulomb friction,  $a_4$  represents the mean value of viscous friction,  $a_3$  represents the joint 2 angle about which the friction profile is symmetric, and  $a_2$  and  $a_5$  represent the coulomb and viscous friction coefficients that vary with the angle of joint 2.

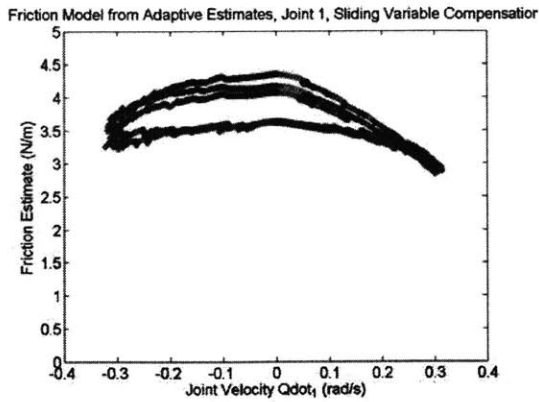


Figure 83: Plot of friction estimate against time for a sinusoidal trajectory of Joint 1, composite variable friction compensation.

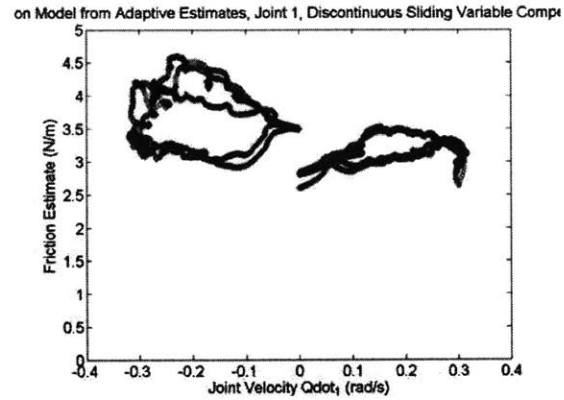


Figure 84: Plot of friction estimate against time for a sinusoidal trajectory of Joint 1, discontinuous composite variable friction compensation

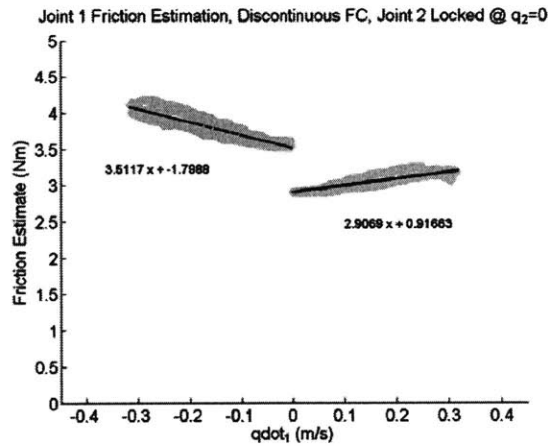


Figure 85: Plot of friction estimate against time for a sinusoidal trajectory of Joint 1 using the discontinuous composite variable control law, with friction compensation to other joints turned off

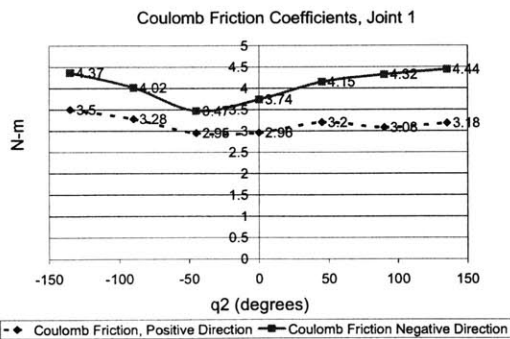


Figure 86: Coulomb friction coefficient of joint 1 as a function of joint 2 position

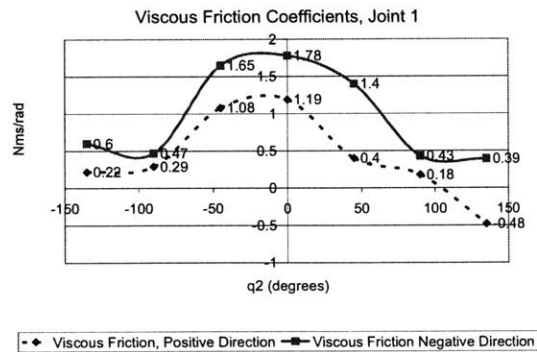


Figure 87: Viscous friction coefficient of joint 1 as a function of joint 2 position

The raw joint angle and velocity data from the joint sinusoid tests used to calculate the parameters in Figure 86 and Figure 87 was combined and used in a non-linear least squares curve fit to estimate the parameters of equation (C.1) for both positive and negative joint velocities. The identified parameters are shown in Table 19.

**Table 19: Coefficients of Equation (4.1) for joint 1 friction**

Direction	$a_1$	$a_2$	$a_3$	$a_4$	$a_5$	Mean % err	Max % err
Positive	3.18	.142	-2.1	.28	-.27	3.3%	10.1%
Negative	4.12	.42	-.74	-.77	-.62	2.6%	9.0%

The identified friction model and parameters provide a good fit to the data for both positive and negative velocity profiles. The model predicted data with a maximum error of just over 10%, and an average error of 2.6% for the negative velocity profile, and 3.3.% for the positive velocity profile. The raw friction estimates from the adaptive algorithm used to perform the curve-fit are plotted in Figure 88. Alongside this data is the model-based estimate of the friction from the curve-fit with the same input parameters, as well as a plot of 90% of the curve-fit. This gain of 90% of the curve-fit will be added to the actual feed-forward model in order to ensure that the friction compensation torque is always lower than the torque from friction.

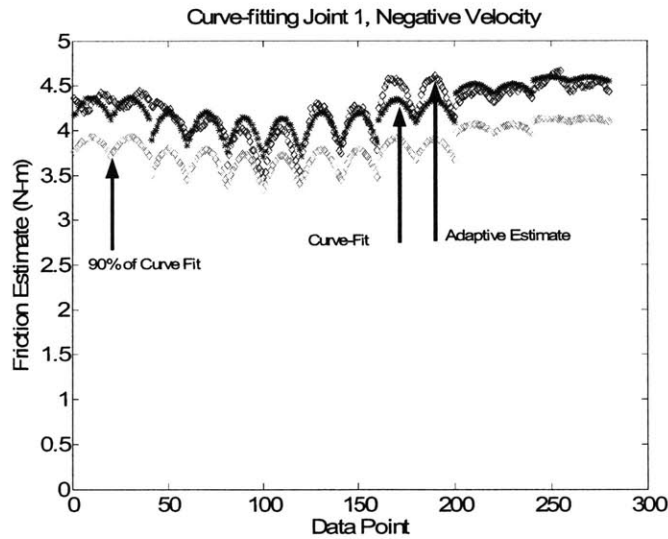


**Figure 88: Curve-fit accuracy of the joint 1 friction model, negative velocity**

# D

## **APPENDIX D: GRAVITY COMPENSATION EQUATIONS**

As stated in section 2.2.2, the joint torque necessary to overcome the effects of gravity is a function of the joint angles of the manipulator and an apparent gravity vector, as seen in equation (D.1). The apparent gravity vector  $\underline{g}$  is a combination of the acceleration of gravity and the acceleration from ship motion. The direction and magnitude of the vector is calculated from the accelerometers and tilt sensors located in the base of the manipulator.

$$\underline{\tau}_{gc} = \underline{\tau}_{gcX}(\underline{q}, g_x) + \underline{\tau}_{gcY}(\underline{q}, g_y) + \underline{\tau}_{gcZ}(\underline{q}, g_z) \quad (D.1)$$

The three directional components of the vector are referred to as  $g_x$ ,  $g_y$ , and  $g_z$ . Figure 89 shows the orientation of these components in a manipulator origin-fixed coordinate system.

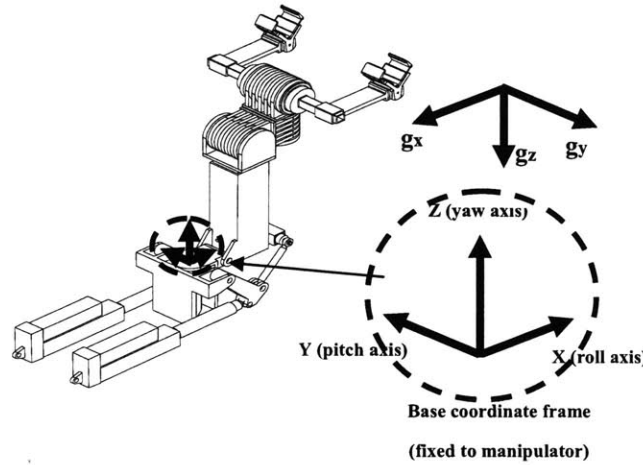


**Figure 89: Coordinate system for the gravity and ship motion compensation algorithm**

The equations to calculate the torque necessary to overcome are on the following three pages. A number of manipulator kinematic and inertial parameters are used in these calculations. These parameters are listed in Appendix E, and are notated as follows:

$q_i$  ( $i = 1, 2, 4, 5, 6$ ): angle of joint  $i$

$g_j$  ( $j = x, y, z$ ): Apparent gravity vector component in  $j$  direction (see Figure 79)

$M_i$  ( $i = 1, 2, \dots, 6$ ): Mass of link  $i$  (see Appendix E)

$M_{payload}$ : Mass of payload (see Appendix E)

$h$ : Height of payload COG with respect to link 6 coordinate frame (see Appendix E)

$a_i$  ( $i = 1, 2, \dots, 6$ ): D - H parameters (see Appendix E)

$d_i$  ( $i = 3, 5$ ): D - H parameters (see Appendix E)

$rx_i$  ( $i = 1, 2, \dots, 6$ ): Link  $i$  center of gravity (COG) with respect to link coordinate frame (see Appendix E)

$ry_i$  ( $i = 1, 2, \dots, 6$ ): Link  $i$  center of gravity (COG) with respect to link coordinate frame (see Appendix E)

$rz_i$  ( $i = 1, 2, \dots, 6$ ): Link  $i$  center of gravity (COG) with respect to link coordinate frame (see Appendix E)

The components of the gravity compensation torque for each joint are calculated independently and then added as in equation (D.1). The components are notated as follows:

$T_{ij}$  ( $i = 1, 2, 4, 5, 6$ )( $j = x, y, z$ ): Torque at joint  $i$  from acceleration in the  $j$  direction

$F_{3j}$  ( $j = x, y, z$ ): Force for joint 3 from acceleration in the  $j$  direction



### Gravity and ship motion compensation torque in the manipulator X direction:

$$T_{6x} = -[[ry_6[\cos q_1 \{ \cos(q_2 + q_4) \cos q_5 \cos q_6 - \sin(q_2 + q_4) \sin q_6 \} - \sin q_1 \sin q_5 \cos q_6] \\ + (a_6 + rx_6)[\cos q_1 \{ \cos(q_2 + q_4) \cos q_5 \sin q_6 + \sin(q_2 + q_4) \cos q_6 \} - \sin q_1 \sin q_5 \sin q_6]]M_6g_x \\ + [h[\cos q_1 \{ \cos(q_2 + q_4) \cos q_5 \cos q_6 - \sin(q_2 + q_4) \sin q_6 \} - \sin q_1 \sin q_5 \cos q_6] \\ + a_6[\cos q_1 \{ \cos(q_2 + q_4) \cos q_5 \sin q_6 + \sin(q_2 + q_4) \cos q_6 \} - \sin q_1 \sin q_5 \sin q_6]]M_{payload}g_x]$$

$$T_{5x} = \{(a_6 + rx_6) \cos q_6 - ry_6 \sin q_6\} \{\sin q_1 \cos q_5 + \cos(q_2 + q_4) \cos q_1 \sin q_5\} M_6 g_x \\ + (a_6 \cos q_6 - h \sin q_6) \{\sin q_1 \cos q_5 + \cos(q_2 + q_4) \cos q_1 \sin q_5\} M_{payload} g_x$$

$$T_{4x} = -[(a_4 + rx_4) \sin(q_2 + q_4) + rz_4 \cos(q_2 + q_4)] \cos q_1 M_4 g_x \\ + [a_4 \sin(q_2 + q_4) + (d_5 + ry_5) \cos(q_2 + q_4)] \cos q_1 M_5 g_x \\ + [a_4 \sin(q_2 + q_4) + d_5 \cos(q_2 + q_4)] \cos q_1 (M_6 + M_{payload}) g_x \\ + [(a_6 + rx_6) \{ \cos(q_2 + q_4) \sin q_6 + \sin(q_2 + q_4) \cos q_5 \cos q_6 \} \\ + ry_6 \{ \cos(q_2 + q_4) \cos q_6 - \sin(q_2 + q_4) \cos q_5 \sin q_6 \}] \cos q_1 M_6 g_x \\ + [a_6 \{ \cos(q_2 + q_4) \sin q_6 + \sin(q_2 + q_4) \cos q_5 \cos q_6 \} \\ + h \{ \cos(q_2 + q_4) \cos q_6 - \sin(q_2 + q_4) \cos q_5 \sin q_6 \}] \cos q_1 M_{payload} g_x]$$

$$F_{3x} = -\cos q_1 \sin q_2 * (M_3 + M_4 + M_5 + M_6 + M_{payload}) g_x$$

$$T_{2x} = -\cos q_1 [ \{ (a_2 + rx_2) \sin q_2 + rz_2 \cos q_2 \} M_2 g_x \\ + \{ (a_2 + a_3 + rx_3) \sin q_2 + (d_3 + ry_3) \cos q_2 \} M_3 g_x \\ + \{ (a_2 + a_3) \sin q_2 + d_3 \cos q_2 \} (M_4 + M_5 + M_6 + M_{payload}) g_x ] + T_4$$

$$T_{1x} = -[(a_1 + rx_1) \sin q_1 M_1 g_x \\ + \{ a_1 + (a_2 + rx_2) \cos q_2 - rz_2 \sin q_2 \} \sin q_1 M_2 g_x \\ + \{ a_1 + (a_2 + a_3 + rx_3) \cos q_2 - (d_3 + ry_3) \sin q_2 \} \sin q_1 M_3 g_x \\ + \{ a_1 + (a_2 + a_3) \cos q_2 + (a_4 + rx_4) \cos(q_2 + q_4) - d_3 \sin q_2 - rz_4 \sin(q_2 + q_4) \} \sin q_1 M_4 g_x \\ + \{ a_1 + (a_2 + a_3) \cos q_2 + a_4 \cos(q_2 + q_4) - d_3 \sin q_2 - (d_5 + ry_5) \sin(q_2 + q_4) \} \sin q_1 M_5 g_x \\ + [\cos q_1 \sin q_5 \{ (a_6 + rx_6) \cos q_6 - ry_6 \sin q_6 \} \\ + \sin q_1 \{ a_1 + (a_2 + a_3) \cos q_2 - d_3 \sin q_2 \\ - \{ d_5 + ry_6 \cos q_6 + (a_6 + rx_6) \sin q_6 \} \sin(q_2 + q_4) \} \\ + \{ a_4 + \cos q_5 \{ (a_6 + rx_6) \cos q_6 - ry_6 \sin q_6 \} \cos(q_2 + q_4) \} ] M_6 g_x \\ + [\cos q_1 \sin q_5 (a_6 \cos q_6 - h \sin q_6) \\ + \sin q_1 \{ a_1 + (a_2 + a_3) \cos q_2 - d_3 \sin q_2 \\ - (d_5 + h \cos q_6 + a_6 \sin q_6) \sin(q_2 + q_4) \\ + \{ a_4 + \cos q_5 (a_6 \cos q_6 - h \sin q_6) \} \cos(q_2 + q_4) \} ] M_{payload} g_x]$$

### Gravity and ship motion compensation torque in the manipulator Y direction:

$$T_{6y} = -[[ry_6[\sin q_1 \{\cos(q_2 + q_4) \cos q_5 \cos q_6 - \sin(q_2 + q_4) \sin q_6\} + \cos q_1 \sin q_5 \cos q_6] \\ + (a_6 + rx_6)[\sin q_1 \{\cos(q_2 + q_4) \cos q_5 \sin q_6 + \sin(q_2 + q_4) \cos q_6\} + \cos q_1 \sin q_5 \sin q_6]]M_6g_y \\ + [h[\sin q_1 \{\cos(q_2 + q_4) \cos q_5 \cos q_6 - \sin(q_2 + q_4) \sin q_6\} + \cos q_1 \sin q_5 \cos q_6] \\ + a_6[\sin q_1 \{\cos(q_2 + q_4) \cos q_5 \sin q_6 + \sin(q_2 + q_4) \cos q_6\} + \cos q_1 \sin q_5 \sin q_6]]M_{payload}g_y]$$

$$T_{5y} = \{(a_6 + rx_6) \cos q_6 - ry_6 \sin q_6\} \{\cos q_1 \cos q_5 - \cos(q_2 + q_4) \sin q_1 \sin q_5\} M_6g_y \\ + (a_6 \cos q_6 - h \sin q_6) \{\cos q_1 \cos q_5 - \cos(q_2 + q_4) \sin q_1 \sin q_5\} M_{payload}g_y$$

$$T_{4y} = -[[ (a_4 + rx_4) \sin(q_2 + q_4) + rz_4 \cos(q_2 + q_4) ] \sin q_1 M_4g_y \\ + [a_4 \sin(q_2 + q_4) + (d_5 + ry_5) \cos(q_2 + q_4) ] \sin q_1 M_5g_y \\ + [a_4 \sin(q_2 + q_4) + d_5 \cos(q_2 + q_4) ] \sin q_1 (M_6 + M_{payload})g_y \\ + [(a_6 + rx_6) \{\cos(q_2 + q_4) \sin q_6 + \sin(q_2 + q_4) \cos q_5 \cos q_6\} \\ + ry_6 \{\cos(q_2 + q_4) \cos q_6 - \sin(q_2 + q_4) \cos q_5 \sin q_6\} ] \sin q_1 M_6g_y \\ + [a_6 \{\cos(q_2 + q_4) \sin q_6 + \sin(q_2 + q_4) \cos q_5 \cos q_6\} \\ + h \{\cos(q_2 + q_4) \cos q_6 - \sin(q_2 + q_4) \cos q_5 \sin q_6\} ] \sin q_1 M_{payload}g_y]$$

$$F_{3y} = -\sin q_1 \sin q_2 * (M_3 + M_4 + M_5 + M_6 + M_{payload})g_y$$

$$T_{2y} = -\sin q_1 [ \{(a_2 + rx_2) \sin q_2 + rz_2 \cos q_2\} M_2g_y \\ + \{(a_2 + a_3 + rx_3) \sin q_2 + (d_3 + ry_3) \cos q_2\} M_3g_y \\ + \{(a_2 + a_3) \sin q_2 + d_3 \cos q_2\} (M_4 + M_5 + M_6 + M_{payload})g_y ] + T_4$$

$$T_{1y} = (a_1 + rx_1) \cos q_1 M_1g_y \\ + \{a_1 + (a_2 + rx_2) \cos q_2 - rz_2 \sin q_2\} \cos q_1 M_2g_y \\ + \{a_1 + (a_2 + a_3 + rx_3) \cos q_2 - (d_3 + ry_3) \sin q_2\} \cos q_1 M_3g_y \\ + \{a_1 + (a_2 + a_3) \cos q_2 + (a_4 + rx_4) \cos(q_2 + q_4) - d_3 \sin q_2 - rz_4 \sin(q_2 + q_4)\} \cos q_1 M_4g_y \\ + \{a_1 + (a_2 + a_3) \cos q_2 + a_4 \cos(q_2 + q_4) - d_3 \sin q_2 - (d_5 + ry_5) \sin(q_2 + q_4)\} \cos q_1 M_5g_y \\ + [-\sin q_1 \sin q_5 ((a_6 + rx_6) \cos q_6 - ry_6 \sin q_6) \\ + \cos q_1 \{a_1 + (a_2 + a_3) \cos q_2 - d_3 \sin q_2 \\ - (d_5 + ry_6 \cos q_6 + (a_6 + rx_6) \sin q_6) \sin(q_2 + q_4) \\ + \{a_4 + \cos q_5 ((a_6 + rx_6) \cos q_6 - ry_6 \sin q_6)\} \cos(q_2 + q_4)\} ] M_6g_y \\ + [-\sin q_1 \sin q_5 (a_6 \cos q_6 - h \sin q_6) \\ + \cos q_1 \{a_1 + (a_2 + a_3) \cos q_2 - d_3 \sin q_2 \\ - (d_5 + h \cos q_6 + a_6 \sin q_6) \sin(q_2 + q_4) \\ + (a_4 + \cos q_5 (a_6 \cos q_6 - h \sin q_6)) \cos(q_2 + q_4)\} ] M_{payload}g_y]$$

**Gravity and ship motion compensation torque in the manipulator Z direction:**

$$T_{6z} = -[(a_6 + rx_6)\{\sin(q_2 + q_4)\cos q_5 \sin q_6 - \cos(q_2 + q_4)\cos q_6\} \\ + ry_6\{\sin(q_2 + q_4)\cos q_5 \cos q_6 + \cos(q_2 + q_4)\sin q_6\}]M_6g_z \\ - [a_6\{\sin(q_2 + q_4)\cos q_5 \sin q_6 - \cos(q_2 + q_4)\cos q_6\} \\ + h\{\sin(q_2 + q_4)\cos q_5 \cos q_6 + \cos(q_2 + q_4)\sin q_6\}]M_{payload}g_z$$

$$T_{5z} = -[\{(a_6 + rx_6)\cos q_6 - ry_6 \sin q_6\} \sin(q_2 + q_4) \sin q_5 M_6 g_z \\ + (a_6 \cos q_6 - h \sin q_6) \sin(q_2 + q_4) \sin q_5 M_{payload} g_z]$$

$$T_{4z} = [(a_4 + rx_4)\cos(q_2 + q_4) - rz_4 \sin(q_2 + q_4)]M_4g_z \\ + [a_4 \cos(q_2 + q_4) - (d_5 + ry_5) \sin(q_2 + q_4)]M_5g_z \\ + [a_4 \cos(q_2 + q_4) - d_5 \sin(q_2 + q_4)](M_6 + M_{payload})g_z \\ + [(a_6 + rx_6)\{\cos(q_2 + q_4)\cos q_5 \cos q_6 - \sin(q_2 + q_4)\sin q_6\} \\ - ry_6\{\cos(q_2 + q_4)\cos q_5 \sin q_6 + \sin(q_2 + q_4)\cos q_6\}]M_6g_z \\ + [a_6\{\cos(q_2 + q_4)\cos q_5 \cos q_6 - \sin(q_2 + q_4)\sin q_6\} \\ - h\{\cos(q_2 + q_4)\cos q_5 \sin q_6 + \sin(q_2 + q_4)\cos q_6\}]M_{payload}g_z$$

$$F_{3z} = \cos q_2 * (M_3 + M_4 + M_5 + M_6 + M_{payload})g_z$$

$$T_{2z} = [(a_2 + rx_2)\cos q_2 - rz_2 \sin q_2]M_2g_z \\ + [(a_2 + a_3 + rx_3)\cos q_2 - (d_3 + ry_3) \sin q_2]M_3g_z \\ + [(a_2 + a_3)\cos q_2 - d_3 \sin q_2](M_4 + M_5 + M_6 + M_{payload})g_z + T_4$$

$$T_{1z} = 0$$

## APPENDIX E: MANIPULATOR PARAMETERS

### Kinematic Parameters

The kinematics of the manipulator are defined in Table 20 using the standard Denavit-Hartenberg convention [47]. Figure 90 shows the link coordinate systems of the manipulator when all joint angles are zero.

**Table 20: Denavit-Hartenberg parameters of the heavy-lift manipulator**  
(from [17], courtesy Foster-Miller, Inc.)

Link	Axis Name	$\alpha_i$	$a_i$ (m)	$\theta_i$	$d_i$ (m)	type	Range
1	Base yaw	$\pi/2$	0.1651	0	0	0	variable
2	Base pitch	$-\pi/2$	0.2951	0	0	0	$-95^\circ$ to $-25^\circ$
3	Arm extension	$\pi/2$	0.0444	0	0	1	0.921 to 1.327 m
4	End pitch	$-\pi/2$	0.3239	0	0	0	$10^\circ$ to $105^\circ$
5	End Yaw	$\pi/2$	0	0	0.3810	0	$-120^\circ$ to $120^\circ$
6	Roll (up to 1500 lb payload)	0	0.5080	0	0	0	$-45^\circ$ to $225^\circ$
6	Roll (1500 to 3000 lb load)	0	0.3810	0	0	0	$-45^\circ$ to $225^\circ$

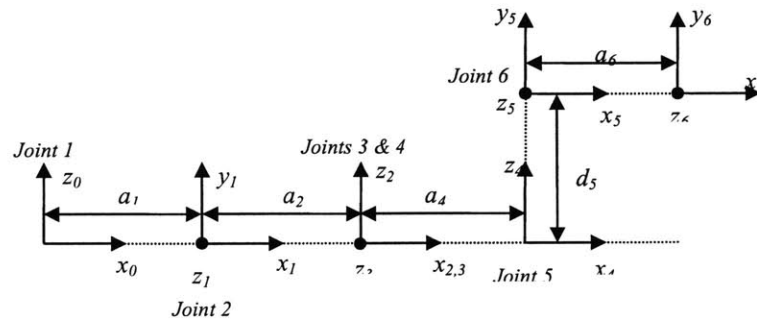


**Figure 90: Link coordinate systems when joint angles are set to zero (from [17], courtesy Foster-Miller, Inc. )**

## Inertial Parameters

Table 21 defines the mass, center-of-mass position, and inertia tensor for each link in the coordinate system of that link.

**Table 21: Inertial parameters of the heavy-lift manipulator (from [17], courtesy of Foster-Miller, Inc.)**

Link	mass (kg)	$r_x$ (m.)	$r_y$ (m.)	$r_z$ (m.)	$I_{xx}$ (kg m <sup>2</sup> )	$I_{yy}$ (kg m <sup>2</sup> )	$I_{zz}$ (kg m <sup>2</sup> )	$I_{xy}$ (kg m <sup>2</sup> )	$I_{yz}$ (kg m <sup>2</sup> )	$I_{xz}$ (kg m <sup>2</sup> )
1	42.034	-.092	-.104	0	0.907	0.329	0.995	-0.236	0	0
2	180.184	-.010	0	0.262	17.456	16.76	8.12	-.054	-.033	-.771
3	193.711	-0.023	-0.292	0	21.307	4.814	20.464	-1.036	-.012	-.001
4	137.217	-.198	0	0.011	2.018	4.551	4.595	0	0	-.262
5	140.268	0	-.143	0	5.016	1.73	5.072	0	0	0
6	191.266	-.427	-.018	0	16.2	21.245	6.302	0.883	0	0

Table 22 defines the mass, center of mass position, and inertia tensor for the representative heavy and light payloads in the coordinate system of link 6.

**Table 22: Inertial parameters of the heavy and light payloads (from [17], courtesy Foster-Miller, Inc.)**

Payload	mass (kg)	$r_x$ (m.)	$r_y$ (m.)	$r_z$ (m.)	$I_{xx}$ (kg m <sup>2</sup> )	$I_{yy}$ (kg m <sup>2</sup> )	$I_{zz}$ (kg m <sup>2</sup> )	$I_{xy}$ (kg m <sup>2</sup> )	$I_{yz}$ (kg m <sup>2</sup> )	$I_{xz}$ (kg m <sup>2</sup> )
Heavy	1360.78	-0.127	0.2286	0	927	927	42	0	0	0
Light	156.0	0	0.2667	0	130	130	0.7	0	0	0

## Friction Parameters

The following friction models and parameters are used in Chapter 3 to simulate joint friction in the manipulator. The models and parameters are extracted from experimental data. Units are in kilograms, meters, seconds, and radians.

### Static-load-dependent Friction Model (joints 1-3)

$$\tau_{friction} = -[(\alpha_2 + \alpha_1 F_{load})(\beta_1 + \beta_1(1 - e^{-\beta_1|\dot{q}|}) + \alpha_3|\dot{q}|)]\text{sgn}(\dot{q}) \quad (\text{E.1})$$

**Table 23: Simulated friction parameters in the linear actuators for joints 1-3**

	$\alpha_1$	$\alpha_2$	$\alpha_3$	$\beta_1$	$\beta_2$	$\beta_3$
Right Base:	$37.4 \times 10^{-6}$	0.04	$1 \times 10^{-4}$	0.6	0.4	0.1
Left Base:	$37.4 \times 10^{-6}$	0.04	$1 \times 10^{-4}$	0.6	0.4	0.1
Joint 3:	$90.0 \times 10^{-6}$	0.04	$1 \times 10^{-4}$	0.6	0.4	0.05

### Torque-dependent Friction Model (joints 4-6)

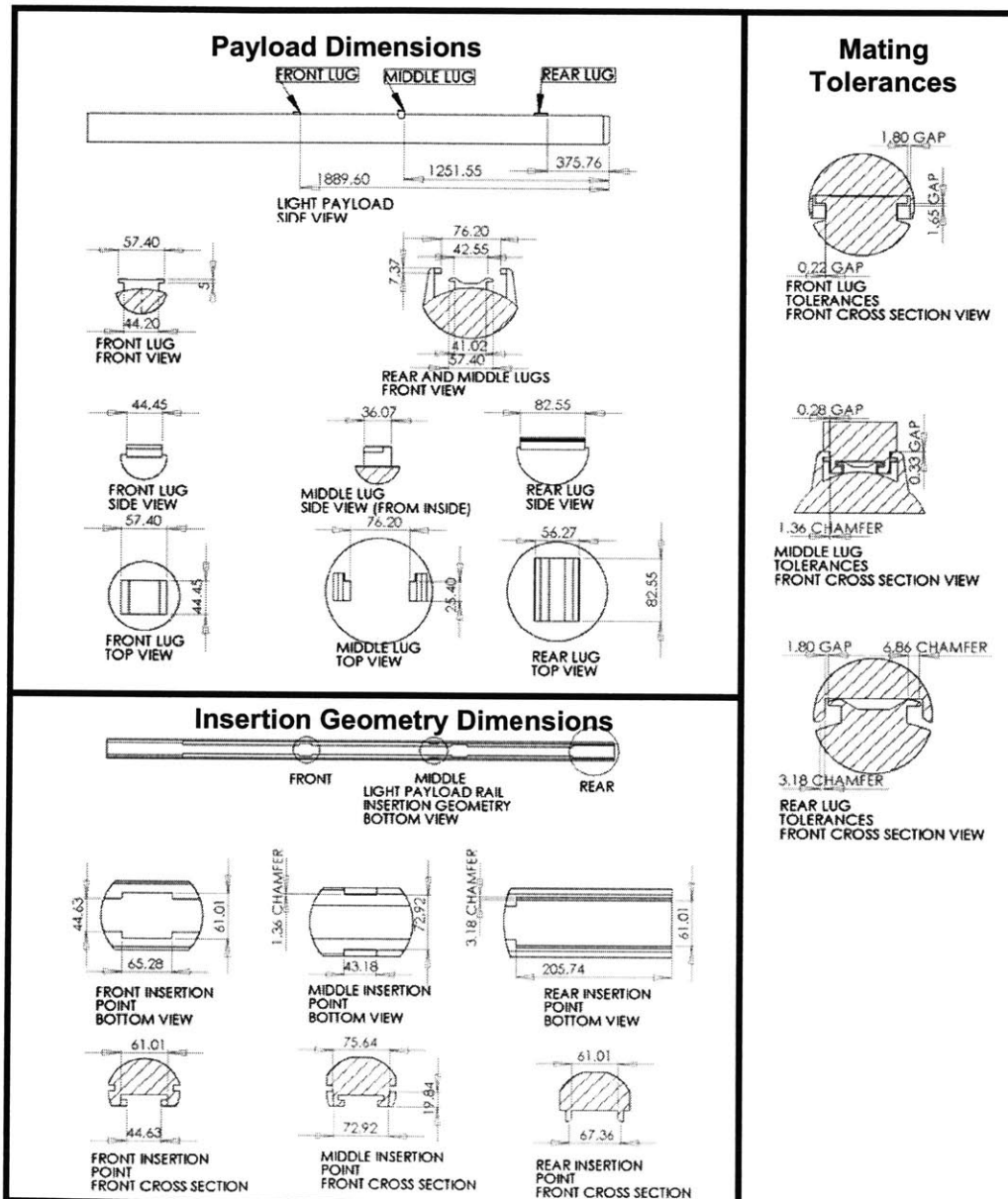
$$\tau_{friction} = -\frac{(1 + \alpha_1|\dot{q}|)(\alpha_2 + \alpha_3|C\tau_{motor}| + \alpha_4(C\tau_{motor})^2)}{C}\text{sgn}(\dot{q}) \quad (2.19)$$

**Table 24: Simulated friction parameters in the direct drive motors for joints 4-6**

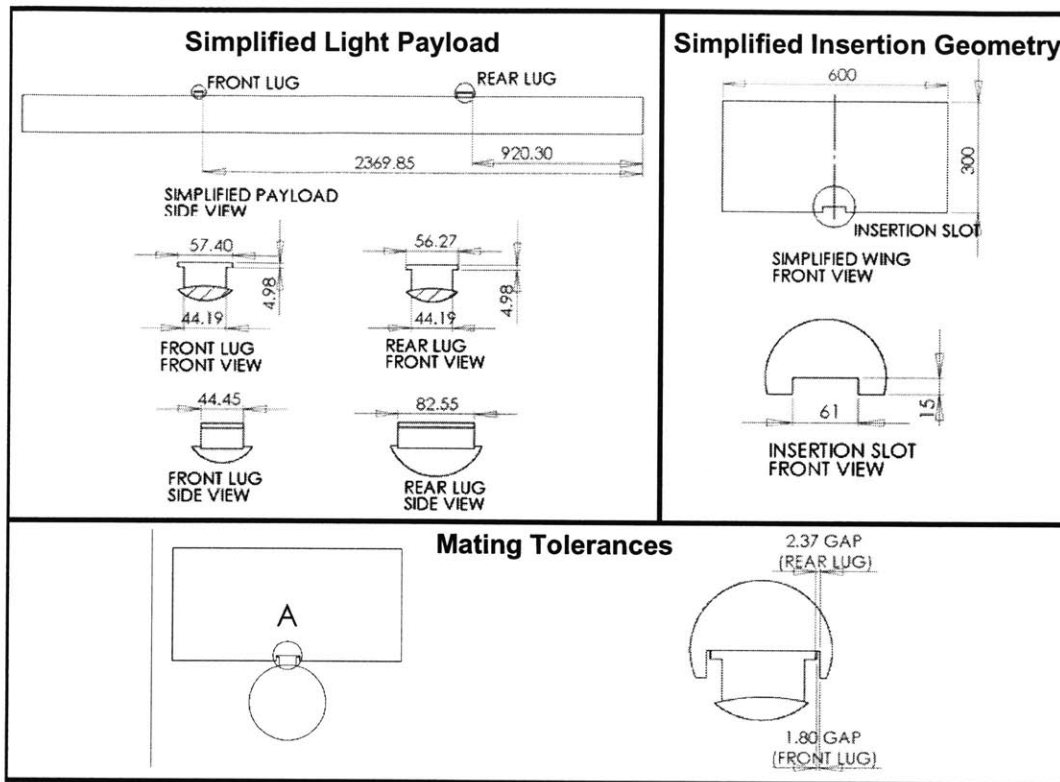
	$\alpha_1$	$\alpha_2$	$\alpha_3$	$\alpha_4$	C
Joint 4:	10	500	0.187	$-1 \times 10^{-6}$	8.8504
Joint 5:	10	150	0.187	$-1 \times 10^{-6}$	8.8504
Joint 6:	10	350	0.187	$-1 \times 10^{-6}$	8.8504

## APPENDIX F: PAYLOAD DIMENSIONS AND TOLERANCES

### Light Payload:

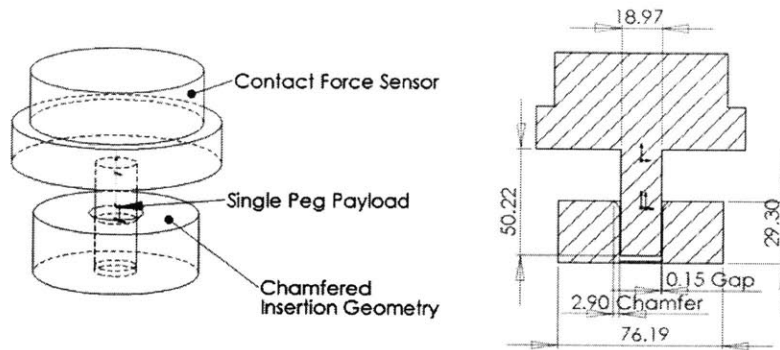


## Simplified Two Lug Payload for Simulations

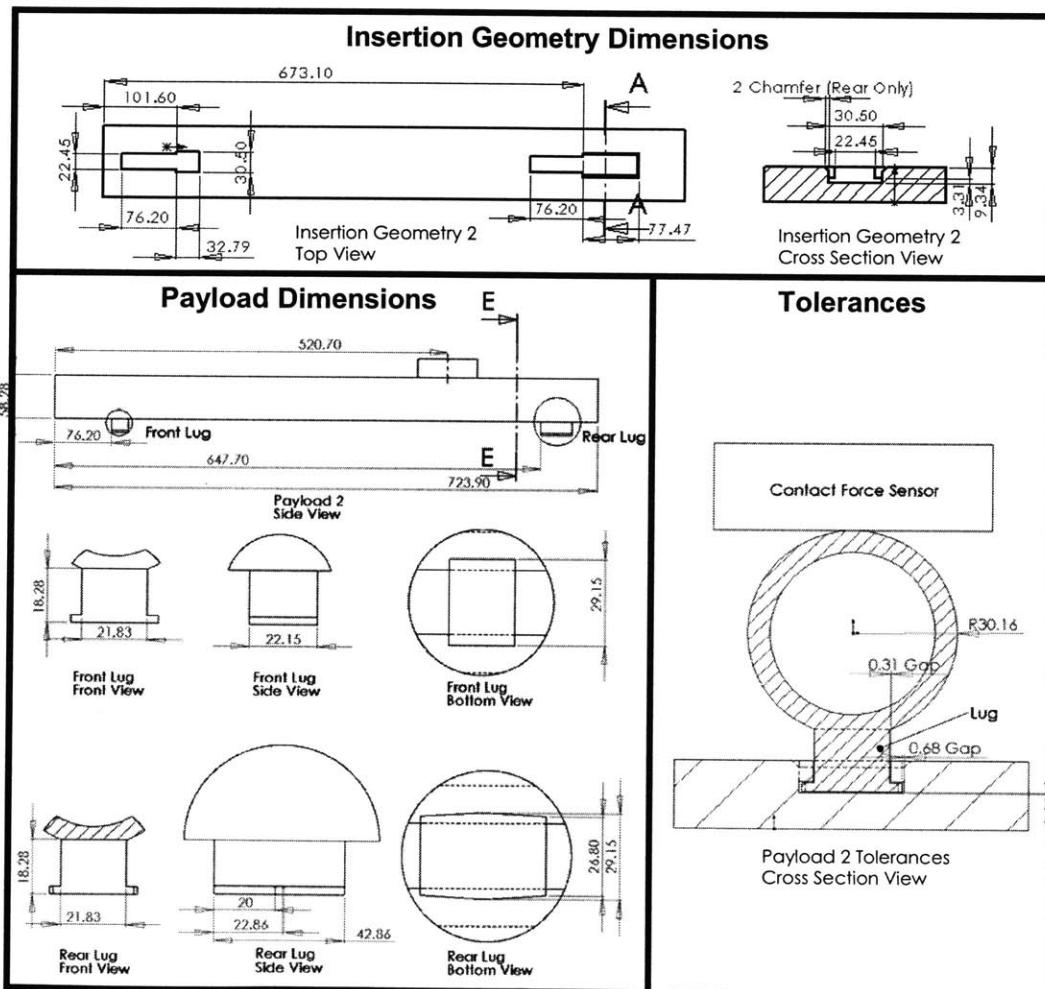




## Single Peg Experimental Payload



## Two Lug Experimental Payload





## **APPENDIX G: INSERTION CONTROL USER SURVEY**

User:

User Amplification:                    1            2            5            10

Friction Compensation: on    off

How would you rate this controller overall (1 = unusable, 2 = barely usable, 5 = great)?

1            2            3            4            5

How would you rate your ability to insert the payload with visual feedback?

1            2            3            4            5

with partial visual feedback?

1            2            3            4            5

with no visual feedback?

1            2            3            4            5

Do you have a good feel of the environment with this controller?

1            2            3            4            5

Do you feel that you are in control of the manipulator?

1            2            3            4            5

Any additional comments?